UNIVERSITY COLLEGE LONDON

Department of Chemistry

Title:

Study of redox activity at modified liquid/liquid interfaces using electrochemical and physicochemical methods

by:

Dimitra Georganopoulou

A thesis presented to the University of London, in partial fulfilment of the requirements for the degree of Doctor in Philosophy

London, November 2001

Abstract:

The aim of this work was to establish an experimental basis for exploration of the reactivity of cell membrane-bound redox enzymes, by using electrochemistry at an aqueous/organic interface. The study presented in this thesis consisted of two parts. The first concerned the effect of surfactant adsorption on interfacial electron transfer. The second involved the measurement of activity of an enzyme within a surfactant-modified interface, catalysing the interfacial electron transfer.

Surfactant adsorption at the interface inhibited electron transfer across an aqueous/organic interface, between ferro/ferricyanide and dimethyl (DiMFc) or decamethyl (DcMFc) ferrocene, directly in proportion to the fraction of the surface covered. Interfacial capacitance and interfacial tension measurements gave the surface coverage of the non-ionic surfactant, sorbitan monostearate, and SECM approach curves gave the overall reaction rate constant. Four-electrode voltammetry revealed an asymmetry of the interface geometry due to surfactant adsorption. Oxidation of the neutral ferrocene was inhibited, but the reduction of ferricenium was not. From the limiting current values for DiMFc oxidation, a model of uncovered micro-holes was proposed and their diameter within the surfactant layer at nominal full coverage was calculated to be ca. 200 nm.

The adsorption of glucose oxidase (GOx) at the H_2O/dichloroethane interface was also investigated, using capacitance and surface tension techniques. Both methods indicated that the adsorption process was time and concentration dependent. The adsorption isotherm obtained from the double layer capacitance suggested that there are two different adsorption states and that the interface saturated at a bulk GOx concentration of 500 nM. This behaviour was further investigated with specular neutron reflection at the water/air interface, assuming that the behaviour of the enzyme adsorption at the two interfaces is similar. This assumption was strengthened by surface tension results at the water/air interface that indicated similar behaviour to that at the water/oil interface. For low concentrations the neutron data were fitted for a uniform layer of small thickness and large area/molecule (molecules flattened after adsorption). For higher enzyme concentrations and high ionic strength the area/molecule became comparable with that expected from the dimensions of the enzyme (molecules retained rigidity). For the even higher concentration range (>400 nM) the fit needed to include a second layer of flattened molecules, adsorbing underneath the first layer.

The reactivity of glucose oxidase adsorbed at the dichloroethane-water interface was studied using scanning electrochemical microscopy, with dimethylferricenium as the mediator, electrogenerated in the organic phase. The feedback current caused by recycling of the mediator as the generator electrode approached close to the interface from the organic side was interpreted in terms of an enzyme-catalysed oxidation of the aqueous substrate, glucose, within an interfacial protein-surfactant film.

Preface:

The present thesis describes the research carried out mainly at University College London during the years 1999-2001.

First and foremost I would like to greatly acknowledge my supervisor Professor David E. Williams for his continuous encouragement and enthusiasm in this work. I am also greatly indebted to Dr. Jörg Strutwolf for his support and for providing the theoretical simulations to the SECM measurements. I am very grateful to all my "friends and colleagues" in G16, Dr. Daren Caruana, Camilla Forssten, Hanna Rajantie and Ali Morshed for an enjoyable environment including great discussions, as well as "impression-day Fridays". I am also very thankful to all the members of technical support at UCL, especially to Jim Stevenson, Dick Waymark, Joe Nolan and John Hughes.

I would also like to express my gratitude to Professor Pat Unwin for his guidance, as he and Jie Zhang helped me, while at Warwick, to understand better the SECM and MEMED experiments, as well as to upgrade my SECM set-up back at UCL. Professor Kyösti and Dr. Annu Kontturi, are gratefully acknowledged for their invitation in the Helsinki University of Technology. Together with the rest of the group in Finland, especially Drs. Bernie Quinn, Riikka Lahtinen, Christoffer Johans and Peter Liljeroth, provided a very enjoyable environment and helped me grasp the concept of interfacial electron transfer. Dr Pereira and Prof. Fernando Silva are also deeply acknowledged for their invitation to Porto University and their input and support with the capacitance measurements. Dr. T.J. SU and Prof. J Lu are acknowledged for their help with the Neutron experiments.

Many thanks are also due to the European network (ODRRELLI), of which UCL was a partner in this project, for supplying the financial support as well as the opportunity to meet, discuss and collaborate with many senior and young researchers in the same field.

Finally and most importantly, I would like to thank all my friends and family and dedicate this thesis to my parents, for all the love, patience and "quantum" support they showed over the years. **Dimitra Georganopoulou**

List of contents

List of cells:

Capacitance:

Cell 1a	*Ag/AgCl*	**(wro)** 0.01 M LiCl 0.001 M $BTPPA^+Cl^-$	**(o)** *Pt* 0.001 M BTPPATPB	**(w)** *Pt* 0.1 M KH_2PO_4 0.1 M K_2HPO_4	*Ag/AgCl*
Cell 1b	*Ag/AgCl*	**(wro)** 0.01 M LiCl 0.001 M $BTPPA^+Cl$	**(o)** *Pt* 0.001 M BTPPATPB	**(w)** *Pt* 0.01 M LiCl	*Ag/AgCl*
Cell 1c	*Ag/AgCl*	**(wro)** 0.01 M TBuACl	**(o)** *Pt* 0.01 TBuATPB	**(w)** *Pt* 0.1 M KH_2PO_4 0.1 M K_2HPO_4	*Ag/AgCl*

Aqueous redox species:

Cell 2a:	*Pt*	(w) Redox species Aqueous Electrolyte	***Ref***
Cell 2b:	*Ag/AgCl*	**(w)** 0.001M $Na_4Fe\ (CN)_6$ 0.01 M NaCl x mM Surfactant	*Pt(25μm)*

Organic redox species:

Cell 3a:	*Ag/AgCl*	**(wro)** 0.01 M LiCl 0.001 M BTPPACl	**(o)** x M x-Fc 0.001 M BTPPATPB	***Pt*** ***(25μm)***
Cell 3b:	*Ag/AgCl*	**(wro)** 0.01 M LiCl 0.001MB Cl	**(o)** 0.01 M DiMFc 0.001 M BTPPA TPB x mM Triton x-100	***Pt*** ***(50 μm)***
Cell 3c:	*Ag/AgCl*	**(wro)** 0.1 M $NaClO_4$	**(o)** 0.01 M DcMFc 0.01 M $ThexAClO_4$ x mM SM	Pt ***(25 μm)***

Four-electrode ET:

Cell 4a:	*Ag/AgCl*	**(wro)** 0.01 M LiCl 0.001 BTPPACl	**(o)** *Pt* 0.0001 M x-Fc 0.001 BTPPA TPB	**(w)** *Pt* Aq. Redox couple Aq. Electrolyte	***Ref***
Cell 4b:	*Ag/AgCl*	**(wro)** 0.01 M LiCl 0.001M BTPPACl	**(o)** *Pt* 0.001 M DiMFc 0.001 BTPPA TPB	*Pt* **(w)** 0.1 M $Fe(CN)_6^{3-}$ 0.01 M $Fe(CN)_6^{4+}$ x M Triton X-100	*Pt*
Cell 4c:	*Ag/AgCl*	**(wro)** 0.01 M LiCl 0.001 M BTPPACl	**(o)** *Pt* 0.001 M DiMFc 0.001 BTPPA TPB x M SM	*Pt* **(w)** 0.1M $K_3Fe(CN)_6$ 0.01M $K_4Fe(CN)_6$ 1.5 M $LiSO_4$	*Pt*

SECM-MEMED:

Cell 5a	(o) *Pt* *Ag* 0.001 M DiMFc 0.1 M TPrATPB	(w) x M $Na_4[Fe(CN)_6]$ 0.01 M TPrACl
Cell 5b:	(o) 0.01 M DcMFc 0.1 M $THexACLO_4$	(w) *Pt* *Ag/AgCl* 0.001M $a_4[Fe(CN)_6].10H_2O$ 0.25 M $NaCLO_4$ 0.002M $NaHCO_3$ 0.1 M NaCl x M Triton X-100
Cell 5c:	(o) 0.01 M DcMFc 0.1 M $ThexAClO_4$ **x M SM**	(w) *Pt* ***Ag(QRE)*** 0.001 M $Na_4[Fe(CN)_6]$ 1 M $NaClO_4$

Enzyme system:

Cell 6a:	*Ag/AgCl*	(wro) 10 mM LiCl 10 mM T(Alk)ACl	(o) *Pt* *Pt* 1 mM DiMFc 10 mM $T(Alk)AClO_4$	(w) 0.05 M Glucose,0.2 M K_2HPO_4 10 mM $T(Alk)Cl\ O_4$ 0.25 mM Triton X-100 560 nM *GOX,*
Cell 6b:	(o) *Ag(QRE)* Pt 1 mM DiMFc 30 mM TPrATPB	(w) 550 nM *GOX,* 0.05 M Glucose 0.2 M K_2HPO_4 10 mM TPrACl		

List of abbreviations and symbols:

Solvents-Surfactant:

1,2-Dichloroethane	DCE
Millipore Q-plus water	H_2O
Sorbitan monostearate	SM
Aqueous phase	(w)
Organic phase	(o)
Aqueous reference junction for the organic phase	(wro)

Redox Couples:

Ferrocene	Fc
Dimethylferrocene	DiMFc
Decamethylferrocene	DcMFc
Tetracyanoquinodimethane	TCNQ

Organic electrolytes-Potential determining ions:

Tetraalkylammonium cation	$T(Alk)A^+$
Perchlorate anion	ClO_4^-
Bis-triphenyl phosphoranylidene cation	$BTPPA^+$
Tetraphenylborate anion	TPB^-

Techniques:

Scanning Electrochemical microscopy	SECM
Microelectrochemical measurements at an expanding droplet	MEMED
Mass spectrometry	MS
Electron ionisation	EI
Fast atom bombardment	FAB
Electrospray	ES

Miscalleneous:

Interface between two immiscible electrolyte solutions	ITIES
Electron transfer	ET
Ion transfer	IT
Potential determining ion	PDI
Critical micelle concentration	CMC
Direct current	dc-
Alternating current	ac-

A	surface area, m^2	T	temperature, K
b_i	scattering length, fm	u	normalised concentration
c^0	bulk concentration of species	z_i	charge of species
C_D	double layer capacitance, F cm^{-2}		
c_i	concentration of species		
d	distance, m	α_i	activity of species, M
D	diffusion coefficient, $cm^2\ s^{-1}$	γ	surface tension, mN m^{-2}
e	electron charge, C	γ_i	activity coefficient
E	potential, V	Γ	surface excess, mol m^{-2}
E^0	standard redox potential, V	$\Delta\phi$	Galvani potential difference, V
F	Faraday constant, C mol^{-1}	ΔG^0	standard free energy, J
f	frequency, Hz	ε	relative permittivity
I	ionic activity	θ	surface coverage
i (I)	current, A	λ	wavelength, nm
j	complex number, □-1	μ	chemical potential, V
$\boldsymbol{k}$	Boltzman constant, J K^{-1}	$\bar{\mu}$	electrochemical potential
K	equilibrium constant, (M^{-1})	μ^0	standard chemical potential, V
k	rate constant, cm $s^{-1}M^{-1}$	$\rho(z)$	scattering length density, fm
n	number of transferred electrons	σ_W	Warbourg coefficient, $\Omega\ s^{-1/2}$
N_A	Avogadro number, mol^{-1}	τ	layer thickness, A
n_i	number density	Z	impedance, Ω
Q	momentum transfer, A^{-1}	Z'	real impedance, Ω
R	gas constant, 8.314 J $mol^{-1}K^{-1}$	Z''	imaginary impedance, Ω
r	radius, m	Z_W	Warburg impedance, Ω
R	resistance, Ω	v	scan rate, mV s^{-1}
R x 10^{-3}	Reflectivity	ϕ	Galvani potential, V
R_a	microhole radius, m	χ	outer potential, V
R_0	radial distance between microholes, m	ψ	surface potential, V
S	total surface area, m^2	ω	angular frequency, Hz

List of tables:

List of figures:

Chapter 1: Introduction to liquid/liquid interfaces

Over the past two decades, the interest in the electrochemistry of the interface between two immiscible electrolyte solutions (ITIES) has increased, due to the challenges and numerous applications it presents. The main reason for this interest is that the water/oil interface can be considered as a simple model for half a biological cell membrane. In this respect, the liquid/immiscible liquid interface represents the separation of the aqueous cytosol, i.e. the internal or external cell medium from the apolar central region of a bilayer membrane[1]. Several aspects of this interface have been investigated, such as the structure, the thermodynamics, as well as the different interfacial charge transfer processes. Based on the need to understand drug delivery and bio-electrolyte equilibrium, studies focused initially on the ion transfer (IT) processes occurring at ITIES. These studies were pursued as the outer membranes of mitochondria for example, were found to be permeable to several ions and polar molecules.

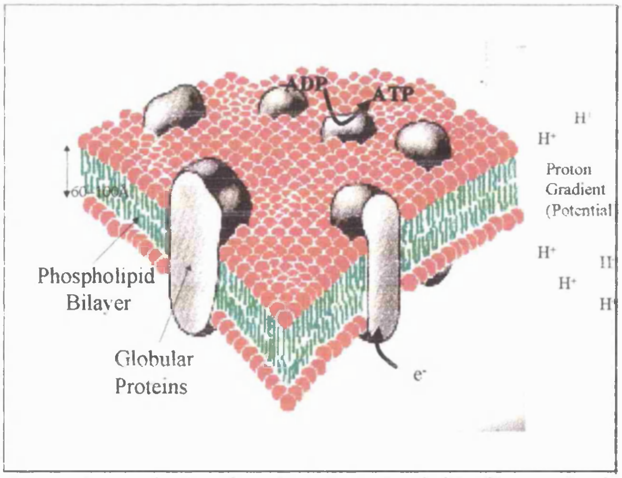

Figure 1. 1 Biological membrane indicating the phospholipid bilayer, the integral and peripheral globular proteins, as well as basic steps of the process of oxidative phosphorylation (from ref. 1)

Inner membranes, on the other hand, were found to be impermeable to almost all ions[2]. These membranes, however, support two major energy conversion processes such as the oxidative phosphorylation in mitochondria and photosynthesis at chloroplasts. Mitchell suggested in 1961[3] that the process of oxidative phosphorylation is induced by a transmembrane electron transfer, followed by a proton gradient establishment. The potential established and the different pH of the two faces of the membrane result in the phosphorylation of

ADP to ATP that is the major reaction of producing energy in the organisms. This aspect of the inner membranes as well as the electrochemical issues that it raises, led to the idea of modelling and studying the transmembrane electron transfer at the liquid/liquid interface. Such a study of the ITIES is a very intriguing one, posing not only pure scientific challenges, but also providing a helpful insight to significant biological processes, with possible general applications.

1.1 Aims and structure of project

Guided by the possibility of modelling aspects of bioelectrochemistry, the aims of the present project were the following:

- Study of adsorption and formation of layers of species such as surfactants and enzymes, with electrochemical and non-electrochemical methods.
- Thorough study and understanding of the process of electron transfer (ET) across an unmodified (clean) interface that is polarised or not, followed by the study of the effect of adsorbed surfactants
- Adsorption of enzymes at a surfactant modified interface in order to study interfacial electron transfer via an enzymatic catalytic process, similar to the one observed in biological membranes.

Several techniques were employed during this work. The individual adsorption of the surfactants and enzymes at the interface was studied initially with capacitance as well as surface tension. The interfacial adsorption behaviour of the enzyme was further clarified using the neutron reflection technique. Since, the main process studied is ET, most of the techniques used in this study were electrochemical. cyclic voltammetry and chronoamperometry, using macro- and micro-electrodes were two dynamic electrochemical techniques used in order to study the interface under consideration. An adaptation of a three-electrode set-up to a four-electrode set-up, with a counter and a reference electrode in either phase, was mainly employed for the study of an ideally polarisable interface between the two phases, with no common ions present. The scanning electrochemical microscopy (SECM) technique was used in order to study non-polarisable interfaces that have a common ion in both phases, measuring the feedback current as the micro-electrode approaches the interface due to interfacial processes. With this technique also, the effect of surfactants and enzymes on interfacial ET was studied. Spectroscopic techniques were used to identify reactants synthesised (Mass Spectroscopy), and the result of possible spontaneous reactions or interfacial transfers between the two phases (UV-Visible). Finally with the aid of microscopy the status of the microelectrodes used was controlled.

1.2 History of electrochemistry at liquid/liquid interfaces

The birth of this specific aspect of electrochemistry dates back almost over a century ago, with the derivation of the Nernst equation in 1888. The ubiquitous equation applies not only to the metal/solution interface but also to the liquid/liquid interface, as was proved by the first electrochemical study of the interface by Nernst and Reisenfield[4]. They investigated the effect of electric current flow across the water/oil interface on the concentration of potassium iodide present in both phases. A few years later, in 1906, Cremer[5] pointed out that the liquid/liquid interface is analogous to the semi-membranes studied by Ostwald[6]. This seemed to be an interesting discovery that could enable the modelling and study of biological membranes electrochemically. In the fifties an accurate thermodynamic description of the chemical and electrochemical equilibrium properties of the interface was obtained. A synopsis of the achievements up to the late sixties in the study of ITIES is given by Davies and Rideal[7]. However, this area remained less developed than other areas of electrochemistry and it was only half a century after its birth that the real breakthrough came with Gavach and Guastalla[8] in 1968. They showed that when the two phases in contact have a common organic ion, the interface is not polarisable, but when the electrolyte in the organic phase is hydrophobic and the one in the aqueous phase is hydrophilic, and the interface can be externally polarised. The Galvani potential difference established at the interface could be used as the driving force for charge transfer reactions. They were also the ones that introduced the new investigation method for studying the interface using a four-electrode potentiostat with two reference and two counter electrodes[9].

The next step was the development of a four-electrode potentiostat, which compensated a large portion of the applied potential lost in solution resistance, from Samec and Marecek in the seventies[10,11]. This instrument allowed the kinetic study of ITIES and its development was closely followed by the ion transfer experiments by Koryta in 1978[12]. These allowed the development of his theory, which based the polarisability of ITIES on the standard free energy of ion transfer. This led electrochemists all over the world to study thoroughly the ITIES and its physicochemical and electrochemical properties. The field of ion transfer has since been widely studied, with several areas being covered such as facilitated ion transfer, ion transfer across lipid membranes and bilayers, and phase transfer catalysis.

Over the last two decades, the area of electron transfer has been the subject of increasing interest. For example Marcus has adjusted his electron transfer theory to apply to liquid/liquid interfaces[13-16]. Novel areas are currently being explored, including metal nanoparticle deposition, photoiduced ET, ET kinetics with SECM technique, electron transfer across lipid membranes, as well as more complicated aspects of electron and ion transfer coupling. The current state-of-the-art is summarised in a special issue of the Journal of Electroanalytical Chemistry[17]. Apart from the numerous papers published on each aspect, several reviews and a number of books have been published that have recounted the course of ITIES through time.[18-19,2021,22] A brief overview is given over the next few sections of this Chapter.

1.3 General characteristics of the liquid/liquid interface.

As already mentioned, there are two different types of interface between the two immiscible liquids studied so far[22]:

- The *ideally polarisable* interface between two immiscible solutions, with a hydrophobic electrolyte in the organic phase and the hydrophilic electrolyte in the aqueous phase. It can be electrochemically polarised in a wide potential range from an external voltage or current source, and is usually studied with a four-electrode potentiostat.
- The *non-polarisable interface* exists between two phases with a common ion (partitioning ion). Since there are few reference electrodes that can be used directly in the organic phase to provide a specific potential difference, it is customary to use a non-polarisable interface to create a reference junction for the organic phase. Alternatively, non-polarisable interfaces can be studied using spectroscopic techniques, or scanning electrochemical microscopy. The potential difference across the interface is determined by the ionic species distributed in both phases.

Immiscibility of the two solvents is the most important factor in ITIES. The limiting factors determining the choice of organic solvent for ITIES are: very low solubility in water, low vapour pressure, sufficient polarity and a density appreciably different from that of H_2O to allow the formation of a stable interface. Moreover, a minimum dielectric constant of 10 is required in order to provide dissociation of many salts within a wide range of concentrations and to permit sufficient conductivity. The solvents, which meet these criteria and have been widely studied in the ITIES are nitrobenzene and 1,2-dichloroethane (DCE). Although DCE has a considerably lower dielectric constant than nitrobenzene, it exhibits a somewhat wider, more useful polarisation window. It has a relative permittivity of ε=10.38 and is an aprotic, inert solvent of type 8 (Bronsted's classification), immiscible to H_2O. Apart from these solvents, in the study of liquid-liquid interfaces a variety of other solvents have been less extensively studied, with an overview presented in the following table:

Table 1.1 Common solvents for liquid/liquid experiments

Solvents	Refs	Solvents	Refs
4-Isopropyl-1-methyl-2-nitrobenzene	23	Benzonitrile	24
Adiponitrile	23	2-fluoro-2'nitrodiphenyl ether	25
Dibutyl carbonate	23	o-Nitro-phenyl-octyl-ether	25
Dioctylcarbonate	23	o-Nitro-phenyl-phenwayl-ether	25
Nitrobenzene mixtyres	26	o-Nitrotoluene	27
Dichloromethane	28	Nitroethane	29
Acetophenone	30	o-Dichlorobenzene	31
Isobutyl-methyl-ketone	32	Propiophenone	33
Chloroform	24	Acetonitrile / Chloroform	34

Extensive information regarding the solvents presented above and their characteristics can be found in "The chemistry of non-aqueous solvents", however the main problem with using these solvents, is that the majority of them are toxic[35].

By varying the aqueous electrolyte or its concentration, it is possible to widen the available potential window. Different aqueous electrolyte cations have different transfer potentials from one phase to the other, thus the positive limit of the potential window can be extended, i.e. K^+ will transfer before Li^+. It was demonstrated by Kontturi[36,37] that by increasing the degree of hydration of the aqueous anion, in the order of $Cl^-<F^-<SO_4^{2-}$, the salting out of the organic electrolyte cation TBA^+ increases and the negative limit of the potential window also increases. The same effect of widening the window is observed by increasing the concentration of the aqueous electrolyte.

When a potential difference is applied, ions distribute near the interface so that an excess of charge is present at each side of the interface. An electrical double layer (EDL) at the ITIES is formed by the distribution of ionic and dipolar constituents in the interfacial region. Under certain circumstances and accepting some assumptions, this kind of phenomenon can be seen as similar to that observed at a metallic electrode/electrolyte solution interface[38]. In this case, the existing theories and techniques used to study the latter case can be transposed to the study of the liquid/liquid interface.

Nevertheless, it should be clarified that the electrical double layer formed at the ITIES is characterised by some specific properties that differ from those of the metal-electrolyte interface[39]. First of all, the boundary between the two immiscible liquids is less well defined than for the metal/electrolyte interface, because the cohesive energy of a metal is much greater than that of a liquid. In a metal/liquid interface the well-defined boundary between the two phases has an electric charge distributed across the metal surface and the ion free layer (inner layer) formed next to the electrode surface. Up to recently, the molecular structure of the liquid/liquid interface remained unresolved with many models proposed, including that of a "mixed layer". Therefore, if the interface consisted of an extended mixed solvent layer, many physical quantities (e.g. permittivity), would have continuous values across the interface. Alternatively, a diffuse double layer could be present, on both sides of the interface, with the charge distribution in both phases preserving their diffuse property.

In the following sections of this Chapter a brief description of some of the main aspects of the ITIES will be described along with some of the literature of experimental findings and/or theoretical treatments supporting them, including:

- the structure of the interface
- ion pairing at the ITIES
- thermodynamics of ITIES
- non polarisable ITIES (partitioning ion)
- ion transfer (IT) of charged species from one phase to the other: thermodynamics/ kinetics / facilitated IT
- electron transfer (ET) between redox species in respective phases: thermodynamics/ kinetics / various aspects of ET
- coupling of ion transfer and electron transfer

1.4 Structure of liquid/liquid interface.

There is still not a complete understanding of the interfacial structure between two immiscible solutions, and the microscopic structure of the double layer remains a controversial topic. This issue has given rise to difficulties in the quantitative description of the kinetics of charge processes at the ITIES. This resulted in terms such as "apparent", "corrected" and "true" rate constant, since the structure of the interface determines the distribution of the electrical potential in the interfacial region[40]. The main problem has been the experimental difficulties related to the detailed study of the interfacial liquid/liquid interface.

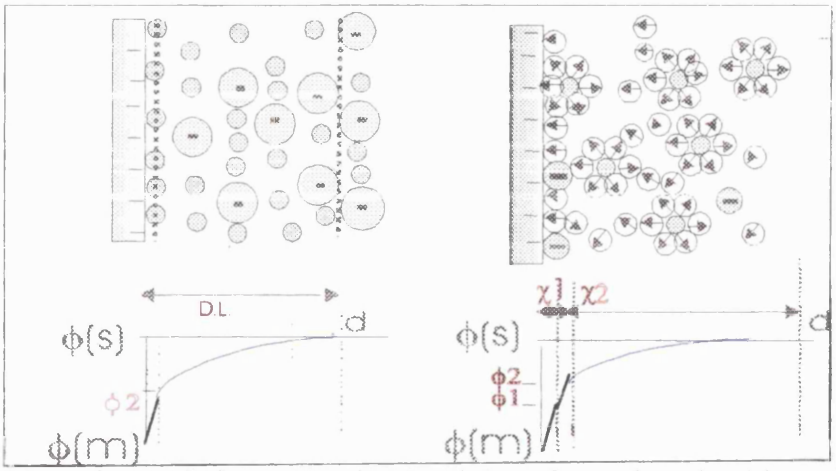

Figure 1. 2 Schematic models for the electrical double layer for an electrolyte/electrode solutions, a. Gouy-Chapman-Stern model combining the Hemholtz and Gouy-Chapman models and b. Grahame's model with the inner Hemholtz plane χ_1 and the outer Hemholtz plane χ_2 that form the Hemholtz layer *a*, shown here for weak specific adsorption.

The analysis of experimental double layer data is still largely based on the classical Gouy-Chapman (GC) theory, proposed for metal/liquid interfaces from the original Hemholtz model (Figure 1.2) by Stern. In this model, applicable only to dilute solutions, ions are considered as point charges and the solvent is simply a dielectric continuum. Grahame later introduced an inner layer modification, which consisted of oriented solvent dipoles or specifically adsorbed ions. This meant that ions could only approach the metal surface to within their solvated radius without being specifically adsorbed or partially desolvated[41,42]. In contrast to the rather orderly development of the theory of the EDL at the metal/liquid interface, development of theory for the liquid/liquid interface involved the proposal of a number of conceptually different models[43], briefly reviewed:

a) Verwey and Niessen[44] gave the first quantitative treatment of the double layer at the ITIES. They represented the liquid/liquid interface as two back to back diffuse double layers, i.e. one phase containing an excess of the positive space charge and the other phase an equal excess of the negative space charge.

b) Boguslavsky *et al.*[45] neglected the diffuse double layer and assumed an ionic bilayer at the ITIES formed by the specifically adsorbed ions on one side of the interface and by ions of the opposite charge on the other.

c) The model of two back to back non interacting diffuse double layers was modified by Gavach,[46] in order to include an ion free inner layer of oriented solvent molecules (compact inner layer) sandwiched between them. This modified Verwey-Niessen model (MVN), was supported by Kakiuchi's electrocapillary experiments[47].

d) Girault and Schiffrin[48] presented an alternative model which replaced the inner layer by a "mixed solvent layer" where there was supposed to be a gradual change in the solvent properties. They also promoted the use of the term of "specific adsorption" to describe the interfacial association between ions in the two respective phases. This idea found support in capacitance results [49] that could not be explained by the GC theory.

e) Samec[50] suggested a further modification of the MVN, taking into account ion penetration into the inner region and then later introducing the use of image forces to correct the GC model in the low permittivity organic phase.

f) The MVN model was further modified and tested at ITIES by Torie and Valleau[51] using the Monte Carlo method to solve a modified Poisson-Boltzmann model (MPB). This model describes the potential distribution in the diffuse layers, taking into account ionic volume, ionic atmosphere and image forces. This was pursued in order to give a better correlation between theoretical predictions and double layer capacitance data, especially at high ionic strength or applied potential, resulting in a thinner diffuse layer of higher capacitance.

g) Cui *et al.*[52] later suggested that the MPB theory correlated better theoretical expectations and experimental data for the interfacial capacitance. It was suggested again (as in the MVN theory) that the two phases were separated by an inner layer, into which the ions could not penetrate and whose dielectric constant was different from those in both phases.

h) Schmickler *et al.*[53] presented a different approach altogether, proposing a lattice gas model in order to describe the interfacial region, where an extended mixed layer exists with a considerable intermiscibility of the two phases in the vicinity of the interface.

i) Recently Benjamin[54] presented molecular dynamic calculations that suggested that the water/dichloroethane interface is very sharply defined but very rough on the molecular scale, manifested by capillaries or fingers of one liquid protruding into the other. These results closely resemble the capillary wave model. These fingers were found to extend up to 8Å within a few picoseconds, with their length dynamically changing with time. The average over time results in a relatively smooth density profile of an interface thickness of 8 Å.

j) Various experimental surface sensitive techniques are currently being employed in order to resolve interfacial structure, such as surface sensitive spectroscopic techniques (second harmonic generation and sum frequency generation)[55]. Strutwolf *et al.* recently presented neutron reflection and scanning electrochemical microscopy experiments[56], showing that any interfacial zone was less than 10 Å thick. This result correlates well with the molecular dynamics simulations and the capillary wave theory.

1.5 Thermodynamics of ITIES

The state of ions in the two different solvents is characterised by the Gibbs energy of solvation G_s with solvent molecules orientating around the ionic species. The Gibbs energy of ion transfer between the two solvents is the difference in the Gibbs energy of solvation in the two solvents. When two immiscible liquids come into contact, there is always a potential difference established across the interface. The electrical (inner) potential ϕ, established in each phase can be attributed to:

a) The orientation of the solvent dipoles in the vicinity of the interface, called the surface potential χ and

b) The presence of free ionic charges separated by the interface, which is called the outer potential ψ.

$$\phi=\chi+\psi \tag{1.1}$$

The magnitude of ϕ is determined by the conditions of the equilibrium established between the two phases. The potential difference established when two immiscible liquids are brought in contact is given by the separation:

$$\Delta\phi=\Delta\chi+\Delta\psi \tag{1.2}$$

with $\Delta\psi$ as the outer/Volta potential difference $\Delta\chi$ the surface potential difference (concentration dependent) and $\Delta\phi$ the Galvani potential difference. At an ideally polarisable liquid/liquid system there are no common ionic species between the two phases. However in a real system all ions have certain solubility in both aqueous and organic systems. Therefore a more practical definition of the polarisability in this case is based on the degree of external control over the interfacial potential difference $\Delta_{(o)}^{(w)}\varphi=\varphi_{(w)}-\varphi_{(o)}$, which is the practical polarisability of the system, with $\varphi_{(w)}$ and $\varphi_{(o)}$ the inner potential of the aqueous and organic phase respectively. The use of appropriate supporting electrolytes in both phases establishes a potential window where various electrochemical processes can be studied, free from the interference from base electrolyte ionic current. On the other hand, for the non-polarisable ITIES, both phases have a common partitioning ion, which is the one that establishes the interfacial potential difference $\Delta_{(o)}^{(w)}\varphi_{\mathrm{Eq}}$. Slight changes of $\Delta_{(o)}^{(w)}\varphi$ from $\Delta_{(o)}^{(w)}\varphi_{\mathrm{Eq}}$ induce large currents passing through the interface.

1.6 Ion pairing at ITIES

Another diversion from ideal situations appears in the case of ion pairing across the interface. According to the theory developed by Bjerrum, all oppositely charged ions within a certain distance of each other are associated in ion pairs. Accordingly, an interfacial ion pair can be formed between two oppositely charged ions depending on their distance of closest approach. The critical distance d^* needed to enable ion pairing is defined as the point where the electrostatic attraction between the two oppositely charged ions overcomes the thermal energies of the ions:

$$d^* = \frac{z_1 z_2 e^2}{2\varepsilon kT} \qquad \textbf{(1.3)}$$

where z_i are the charges of the ions, e the electron charge, k the Boltzman constant, ε the solvent relative permittivity, T is the temperature given in Kelvins. Equation 1.3 implies that ion pairing is more likely to happen, the smaller the relative permittivity of the solvent is. The critical distance for each solvent is d^*_{water} =3.57 Å and d^*DCE=27.39 Å. As an approximation, all oppositely charged ions within these distances become "undissociated" ion pairs. For greater or equal distances between the ions in each solvent than the critical distances mentioned, there will be no ion pairing. In a similar way, it is possible to observe ion pairing between oppositely charged ions across the interface. Ion pairing occurring between small ions in the aqueous phase (e.g. alkali metal cations,) and the organic electrolyte ion (e.g. tetraphenylborate, TPB^-) has indeed been reported by Cheng *et al.*[49]. They observed that bigger alkali cations were more prone to form ion pairs with TPB^- ($Cs^+ > Rb^+ > K^+ > Na^+ > Li^+$). They suggested that this was due to the fact that smaller aqueous ions have larger hydration shell that can not penetrate the interfacial region to the same extent as bigger aqueous ions. Conversely, small organic cations were found to be more likely to form ion pairs. Perreira *et al.*[53] argued that this was due to the fact that although small organic ions have smaller radius they can penetrate the interfacial region more easily, as, unlike aqueous ions, they don't form stable solvation shells.

1.7 Partitioning ion at non-polarisable interfaces

A non polarisable interface is the interface between two phases, in the presence of a common partitioning ion *i*[57,58]. The equilibrium condition at constant temperature and pressure, between these two phases (a) and (b) in contact can be expressed as the equality of electrochemical potential of common components *i*: $\bar{\mu}_{i(w)} = \bar{\mu}_{i(o)}$. The definition of the electrochemical potential $\bar{\mu}_i$ for a charged common species, is a combination of contributions from the chemical energy and from the electrostatic energy of the species, given by the following expressions:

$$\tilde{\mu}_i = \mu_i + z_i F\phi \qquad = \mu_i^0 + RT \ln \alpha_i + z_i F\phi \tag{1.4}$$

where ϕ is the electrical potential,

z_i is the charge of the particle *i*,

μ_i is the chemical potential of component *i*,

μ_i^0 is the standard chemical potential of component *i*,

α_i is the activity of the component *i*.

F is the Faraday constant 96485 A s mol^{-1}

R is the molar gas constant 8.314 J mol^{-1} K^{-1},

T is the absolute temperature in Kelvin.

It is not possible to separate the two terms and split the electrochemical potential into a chemical and an electrical term. Based on the condition of equilibrium given above, the potential difference between the phases, for example the aqueous (w) and the organic (o) can be expressed with:

$$\Delta_{(o)}^{(w)}\varphi_i = \frac{1}{zF}(\mu_{i(o)} - \mu_{i(w)}) \tag{1.5}$$

where $\Delta_{(o)}^{(w)}\varphi_i = \varphi_{i(w)} - \varphi_{i(o)}$ is the Galvani potential difference, i.e. the difference in the inner potential between the aqueous and the organic phase. The definition of the chemical potential is substituted in equation (1.5), with the activity α_i replaced by the concentration c_i and the ionic activity coefficient γ_i $(\alpha_i = \gamma_i c_i)$:

$$\Delta_{(o)}^{(w)}\varphi = \frac{1}{zF}(\mu_{i(o)}^{0} - \mu_{i(w)}^{0}) + \frac{RT}{zF}\ln\frac{\gamma_{i,(o)}c_{i,(o)}}{\gamma_{i,(w)}c_{i,(w)}} \quad \textbf{(1.6)}$$

where the constants and variables have the same meaning as mentioned above. However the standard Gibbs energy of transfer for an ion *i* from the organic phase (o) to the aqueous phase (w) is:

$$\Delta G_i^{0(o\rightarrow w)} = -zF\Delta_{(o)}^{(w)}\varphi^0 = (\mu_{i(w)}^{0} - \mu_{i(o)}^{0}) \quad \textbf{(1.7)}$$

and therefore by combining the two previous equations, a Nernst type equation is given for the Galvani potential difference $\Delta_{(o)}^{(w)}\varphi$:

$$\Delta_{(o)}^{(w)}\varphi = \Delta_{(o)}^{(w)}\varphi_i^0 + \frac{RT}{zF}\ln\frac{\gamma_{i,(o)}c_{i,(o)}}{\gamma_{i,(w)}c_{i,(w)}} \quad \textbf{(1.8)}$$

which can be rewritten as:

$$\Delta\phi = \Delta\phi^0 + \frac{RT}{zF}\ln\frac{a_i^{(o)}}{a_i^{(w)}} \quad \text{or} \quad \Delta\phi = \Delta\phi^\theta + \frac{RT}{zF}\ln\frac{c_i^{(o)}}{c_i^{(w)}} \quad \textbf{(1.9)}$$

with $\Delta\phi^0$ is the standard Galvani potential difference of a common ion and $\Delta\phi^\theta$ the formal potential that takes into account the activity coefficient:

$$\Delta\phi^\theta = \Delta\phi^0 + \frac{RT}{zF}\ln\frac{\gamma_i^{(o)}}{\gamma_i^{(w)}} \quad \textbf{(1.10)}$$

that varies from medium to medium, as the activity coefficients vary. Standard electrode potentials, E^0, are referenced against the hydrogen electrode assuming that the energy of reaction $H^+ + e^- \leftrightarrow \frac{1}{2} H_2$ is zero. The standard Galvani potential difference, $\Delta\phi^0$, is related to the Gibbs energy of transfer and differs from the standard electrode potential in that the former refers to extra thermodynamic assumptions presented here. The most fundamental assumption, is the one proposed by Parker[59], which states that for an organic electrolyte constituted by two sufficiently large hydrophobic ions, e.g. the tetraphenylarsonium$^+$ and the tetraphenylborate$^-$, the two ions have equal standard Gibbs energies of transfer between any pair of solvents. This is based on the fact that both these ions are symmetrical and large with almost the same size and shape, having the charge on the central atom buried under the phenyl groups. Therefore their solvation energy is the same, i.e. their chemical potential is the same.

1.8 Ion transfer (IT)

Ion transfer is one of the two faradaic processes that have been extensively studied at ITIES. It has applications in analytical chemistry with particular fields of interest drug delivery[60] and biosensors[61]. It is a fast process (typically $>10^{-2}$ cm s^{-1}) and diffusionally controlled so that it is reversible. In the previous section the potential is defined by a partitioning ion, common in both phases that is not part of the system under study. Conversely, ion transfer is usually studied with a polarisable interface established between two phases, where only one of them consists of the charged species *i*. The established interfacial potential from the hydrophobic and hydrophilic electrolyte is such that it prevents the partitioning of species. In this case, the potential is externally applied to polarise the interface driving the ion to be transferred reversibly from one phase to the other.

1.8.i Thermodynamics of simple ion transfer

The Galvani potential difference for ion transfer is also given by equation (1.8), associated with a single ionic component in one phase, but is not a directly accessible quantity. Values for $\Delta_{(o)}^{(w)}\varphi_i^0$ and $\Delta_{(o)}^{(w)}G_{tr}^0$ defined in section 1.7 have been published for several ions based on the extra thermodynamic assumptions, using the Gibbs energy of partition for components when the two solvents are at thermodynamic equilibrium[43]. The Gibbs energy of transfer $\Delta G_{tr}^{(w\rightarrow o)}$ refers to the transfer of an ion *i* from a pure solvent (a) to pure solvent (b) (see Appendix I). The standard potential difference $\Delta_{(o)}^{(w)}\varphi_i^0$ for a transferring ion quantifies the relative affinity of an ion for both phases when both solvents are in mutual solvation. It can be estimated from the reversible half wave potential of the four-electrode cyclic voltammetry experiments. Many charged species have been studied in this way, and apart from the thermodynamic data, values for diffusion coefficients as well as kinetic parameters have been published in different solvent systems[62].

1.8.ii Kinetics of simple ion transfer

The following simple schematic shows a simple ion transfer process, when the aqueous phase is for example positively charged with respect of the organic. This can be achieved if the necessary energy is externally provided to charge the double layer, when finally a potential is reached that corresponds to the Gibbs free energy of transfer across the interface:

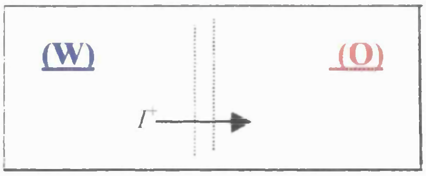

There have been extensive studies on the kinetics of IT which are listed in a comprehensive review by Samec[43]. Kinetic data can be extracted and trusted once the ohmic drop can be reliably compensated for. This can be achieved with the use of improved instrumentation, or the development of micro-interfaces. The IT process is assumed to follow the first order rate law.

The IT kinetics studied with cyclic voltammetry can be described by a Butler-Volmer (B-V) equation[63] although Kakiuchi[64] has also formulated a Nernst-Planck equation (activationless process) that better describes the *i-E* relationship for IT Most models for IT kinetics assume an activated step, ignoring the interfacial structure. In this case Frumkin type corrections are applied to the "apparent" kinetic parameters, with the potential drop across the diffuse double layer taken into account.

1.8.iii Facilitated ion transfer

The standard transfer potential is related to the Gibbs energy of solvation G_s in both phases and can significantly shift in value when specific ionic complexes occur. In the case of facilitated (mediated or assisted) ion transfer, a strongly hydrophobic complexing ligand L, is present in the organic phase, and can selectively combine with a specific ion in the aqueous phase, thus facilitating its transfer across the interface[65]. The transfer of some very hydrophilic ions occurs at highly positive potentials that lie outside the observable potential window (established by the electrolytes in each phase). In this case, an ionophore can be used to shift the transfer in a negative direction so that it can be observed, within the potential window. It is widely used for two-phase solvent extraction of metal ions.

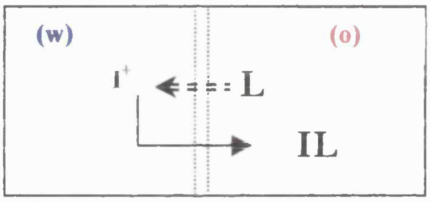

The potential for the IT is shifted according to the following equation:

$$\Delta\varphi = \Delta\varphi_{I^+} - \Delta\varphi_L = (\frac{RT}{zF})\ln[K^0_{I^+L}C^0_L] \qquad \textbf{(1.14)}$$

where z_{I^+} is the charge of the ion

$K^0_{I^+L}$ is the formation constant of the complex

C^0_L is the concentration of the ligand in the organic phase.

Assuming that the diffusion coefficient of the ligand is the same as that of the complex, the association constant *K* can be calculated from the transfer experiments. Some kinetics results imply that IT in this case takes place interfacially in a single step and is called the E-type mechanism. The process is diffusionally controlled and the concentration of the transferred ion is much greater than that of the complexing agent, with the stoichiometry of the reaction being of great importance. The effect of hydrogen bonding and protonation on facilitated IT has also been thoroughly studied[43].

1.9 Electron transfer (ET)

Two immiscible solutions containing a redox couple but no partitioning species are brought into contact. In this case, a redox reaction does not necessarily take place spontaneously, but an interfacial Galvani potential difference is established. The equilibrium of the system that drives the interfacial reaction is described by a Nernst-type equation that depends on the following terms:

- The difference in the standard potential of the redox couples ΔE^0
- The interfacial Galvani potential difference established between two phases $\Delta\phi$

It is possible to have IT and ET at the same time, therefore when they are studied separately, it has to be established that they occur at well-separated potentials.

1.9.i Characteristics of electron transfer

The interfacial electron transfer process from the organic to the aqueous phase is shown in the simple schematic below. If the ET between the two redox species is unfavourable, the necessary potential difference, required to drive the reaction in the desired direction, can be provided either by the presence of partitioning common ion (reverse uphill ET), or with an externally applied potential difference (e.g. four-electrode voltammetry).

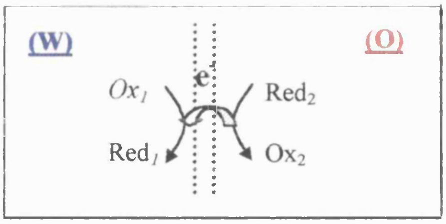

When a partitioning ion is present, ET happens as soon as the two phases come into contact, and the partitioning ion maintains electroneutrality in both phases. The ET process can then be indirectly studied by the depletion or production of electroactive species involved in the ET reaction. In the case of the externally applied potential difference, the standard potentials firstly need to be closely matched. In this case, the necessary potential difference needed for interfacial ET can be observed within the potential window. Electroneutrality in each phase is maintained by the reactions at the counter electrodes, which supply the current through the cell. One concept behind the study of ET at ITIES is that the reaction of the redox species at a metal electrode in the organic system can equally well be monitored with a four-electrode system. This is established by replacing the metal electrode with a concentrated aqueous phase where high concentrations of both the reduced and oxidised components exist. The idea is that the Fermi level of the aqueous phase will remain effectively constant during the ET process and the solution will therefore behave as an extension of a metal electrode.

Electron transfer at ITIES has much slower rate constants than ion transfer, or indeed than ET at electrolyte-solid electrode systems. This observation has been attributed to the following factors[66]:

- Larger distances between the redox centres, present in the corresponding phase
- Higher reorganisation energies for the precursor complexes formed suggested to participate in the ET at ITIES.

1.9.ii Thermodynamics of electron transfer

The system of a homogeneous ET is presented first, in order to transpose it next to the heterogeneous system. In an one-phase system, where only the $Ox^{(1)}$ and $Red^{(2)}$ components are present initially, the redox reaction that takes place is:

$$Ox^{(1)}+Red^{(2)} \leftrightarrow Red^{(1)} + Ox^{(2)}$$

For this system there are four adjustable physical parameters (the concentration of the four components) that are related by three conditions, namely the two mass balance equations, and the redox equilibrium, given by the standard Gibbs energy:

$$\Delta G^0 = -RT\ln\frac{a_{ox^{(2)}}a_{\mathrm{Re}\,d^{(1)}}}{a_{Ox^{(1)}}a_{\mathrm{Re}\,d^{(2)}}} \qquad (1.15)$$

Where ΔG^0 is the standard Gibbs energy of the homogeneous redox reaction and a_{Redox} the activities of the different redox species in the same medium. Therefore, the degree of freedom of the former system is one, (univarient system), and the concentrations of the redox couples can't be varied independently

On the other hand, for a heterogeneous ET, there are five adjustable physical parameters, including the Galvani potential difference, therefore the variance of the system is two (bivariant system). This means that the concentrations of the redox components can be varied independently, thus changing the Galvani potential difference. Therefore it is possible as the two phases come into contact, each containing the redox species (w):$\mathrm{Ox}^{(1)}/\mathrm{Red}^{(1)}$ and (o):$\mathrm{Ox}^{(2)}/\mathrm{Red}^{(2)}$, to establish an interfacial potential difference $\Delta\phi$, where no ET takes place as shown in equation[67]:

$$\Delta G^{0}{}_{E.T.} = -RT\ln\frac{a_{ox^{(o)}}a_{\mathrm{Re}d^{(w)}}}{a_{Ox^{(w)}}a_{\mathrm{Re}d^{(o)}}} - zF\Delta^{(w)}_{(o)}\varphi \tag{1.16}$$

Where $\Delta G^0{}_{(E.T)}$. is the standard Gibbs energy of the heterogeneous ET

$\alpha_{Redox^{(s)}}$ is the corresponding activities of the different redox species

$\Delta\phi_{(o)}{}^{(w)} = \phi(\mathrm{w}) - \phi(\mathrm{o})$ is the Galvani interfacial potential difference.

z is the number of electrons participating in ET,

ET across the interface, $\mathrm{Ox}^{(w)}+\mathrm{Red}^{(o)} \leftrightarrow \mathrm{Ox}^{(o)}+\mathrm{Red}^{(w)}$ will occur once the necessary interfacial potential difference $\Delta^{(w)}_{(o)}\varphi^{0}$, is provided. Replacing the standard Gibbs energy of the ET by its definition:

$$\Delta G^{0}{}_{E.T.} = -zF\Delta^{(w)}_{(o)}\varphi^{0} \tag{1.17}$$

it can be concluded that the interfacial Galvani potential difference , due only to the presence of the redox species in either phase is given by the following Nernst type equation (swapping the activities):

$$\Delta^{(w)}_{(o)}\varphi = \Delta^{(w)}_{(o)}\varphi^{0} + \frac{RT}{zF}\ln\frac{a_{ox^{(w)}}a_{\mathrm{Re}d^{(o)}}}{a_{Ox^{(o)}}a_{\mathrm{Re}d^{(w)}}} \tag{1.18}$$

The Gibbs energy of ET between the two redox couples is also given by equation (1.19), when the standard Galvani potential difference for ET is related to the electrochemical potentials of the components present:

$$\Delta^{(w)}_{(o)}\varphi^{0}_{ET} = [(\mu^{0}_{Ox_{(o)}} + \mu^{0}_{\mathrm{Re}d_{(w)}}) - (\mu^{0}_{Ox_{(w)}} + \mu^{0}_{\mathrm{Re}d_{(o)}})] \tag{1.19}$$

Replacing the standard Galvani potential difference $\Delta_{(o)}^{(w)}\varphi^0$ from equation (1.19) into (1.18) and after substituting $E^0_{Ox/\mathrm{Re}\,d_{(o)}} = \mu^0_{Ox_{(o)}} - \mu^0_{\mathrm{Re}\,dx_{(o)}}$:

$$\Delta_{(o)}^{(w)}\varphi = E^0_{Ox/\mathrm{Re}\,d_{(o)}} - E^0_{Ox/\mathrm{Re}\,d_{(w)}} + \frac{RT}{n_1 n_2 F}\ln\frac{a_{ox^{(w)}}a_{\mathrm{Re}\,d^{(o)}}}{a_{Ox^{(o)}}a_{\mathrm{Re}\,d^{(w)}}} \qquad \textbf{(1.20)}$$

where $E^0_{Ox/\,Red}$ is the standard electrode potential for each redox species in their respective phase, corrected to the Galvani scale with respect to one phase (by convention potentials are usually expressed vs. SHE in the aqueous phase),

n_1 and n_2 are the number of electrons exchanged from the aqueous and organic phase respectively, with $z=n_1n_2$ the stoichiometric coefficient. Therefore from equation (1.20), although the interfacial difference is $\Delta_{(o)}^{(w)}\varphi = \varphi_{(w)} - \varphi_{(o)}$ the standard Galvani potential difference for ET becomes when the activity ratio is 1:

$$\Delta_{(o)}^{(w)}\varphi^0_{ET} = E^0_{Ox/\mathrm{Re}\,d_{(o)}} - E^0_{Ox/\mathrm{Re}\,d_{(w)}} \qquad \textbf{(1.21)}$$

1.9.iii Potential control for electron transfer

- Based on equation (1.20), the system's position of equilibrium can be set by an externally imposed Galvani potential difference using 4 electrodes. The potential difference established across the two reference electrodes is denoted as the cell potential difference E_{Cell}[11]:

$$E_{Cell} = E^{(w)}_{\mathrm{Re}\,f} + \Delta_{(o)}^{(w)}\phi - E^{(o)}_{\mathrm{Re}\,f} \qquad \textbf{(1.22)}$$

In the case that the organic reference electrode is established with a Nernst-Donnan equilibrium between the organic phase (o) and an aqueous reference junction (wro) with a common ion *i*, as in section 1.7, equation (1.22) becomes:

$$E_{Cell} = E^{(w)}_{\mathrm{Re}\,f} + \Delta_{(o)}^{(w)}\phi - \Delta_{(o)}^{(w)}\phi_i - E^{(wro)}_{\mathrm{Re}\,f} \qquad \textbf{(1.23)}$$

where $\Delta_{(o)}^{(w)}\phi_i$ is due to the partitioning ion in wro/o,

$\Delta_{(o)}^{(w)}\phi$ is given in equation (1.18),

and E_{Ref} are the potential of the reference electrodes.

In this case the standard Galvani potential difference, $\Delta_{(o)}^{(w)}\phi^0$, is chosen to be close to 0, based on the standard potentials of the redox species used (cf. equation (1.21)). This limitation exists as the external potential difference applied can only be of the order of mV in order to drive the activity ratio in a favourable direction, as the process must be observed within the limited potential window established. This is therefore the rationale of closely matching the redox potentials of the two species.

- Alternatively the presence of a partitioning ion in both phases, with concentration significantly higher than that of the redox couples, fixes the interfacial potential difference to a specific value. In this case the degree of freedom is again reduced to one as another restrictive condition is included. The partition equilibrium as seen in equation (1.8) is:

$$\Delta_{(o)}^{(w)}\varphi_i = \Delta_{(o)}^{(w)}\varphi_i^0 + \frac{RT}{zF}\ln\frac{a_{i^{(o)}}}{a_{i^{(w)}}} \qquad \mathbf{(1.24)}$$

This is also established when one of the constituents of the cell system partitions, such as for example a base electrolyte ion. The partitioning ion fixes the Galvani potential difference but is not part of the redox system. In this case the equation for the equilibrium across the interface is given by the combined equation[68]:

$$\ln\frac{a_{ox^{(w)}}a_{\mathrm{Red}^{(o)}}}{a_{Ox^{(o)}}a_{\mathrm{Red}^{(w)}}} = \frac{zF}{RT}(E^0_{Ox/\mathrm{Red}_{(w)}} - E^0_{Ox/\mathrm{Red}_{(o)}} + \Delta_{(o)}^{(w)}\varphi_i^0) + \frac{n_1 n_2}{z_i}\ln\frac{a_{i^{(o)}}}{a_{i^{(w)}}} \qquad \mathbf{(1.25)}$$

From this equation the established Galvani potential difference established by the partitioning ion, based on its standard transfer potential and its activities in the system, can be chosen to be such that would match the standard potentials of the two redox species. Numerous papers in the literature have studied the effect of a partitioning ion on ET at ITIES. In this case, ET occurs as soon as the two phases come into contact, allowing therefore only an indirect measure of the ET, spectroscopically, or with SECM

1.9.iv Kinetics of electron transfer

The kinetics of the ET process across the interface of two immiscible electrolyte solutions has been the subject of extensive studies. The process is a bimolecular reaction and the rate of reaction is given by[69]:

$$J = \overrightarrow{k}\, c^{Ox1}_{s,(w)} c^{\mathrm{Re}d2}_{s,(o)} - \overleftarrow{k}\, c^{\mathrm{Re}d1}_{s,(w)} c^{Ox2}_{s,(o)} \qquad \textbf{(1.26)}$$

where *J* represents the interfacial ion flux $J = {}^{I}\!/_{zAF}$, with A the interfacial area

$c^{Ox,\mathrm{Re}d}_{s}$ (mol cm^{-2}) are the surface concentrations of species in either solvent

$\overrightarrow{k}$ and $\overleftarrow{k}$ are the forward and reverse heterogeneous rate constants

Following the Butler Volmer formalism the rate constants are functions of $\Delta^{(w)}_{(o)}\varphi$ and may be expressed in the absence of a double layer effect:

$$\overrightarrow{k} = k^{\theta}_{app} \exp(-\alpha nF \frac{(\Delta^{(w)}_{(o)}\varphi - \Delta^{(w)}_{(o)}\varphi^{\theta})}{RT}) \qquad \textbf{(1.27)}$$

for the forward rate constant and the corresponding for the reverse one:

$$\overleftarrow{k} = k^{\theta}_{app} \exp((1-a)nF \frac{(\Delta^{(w)}_{(o)}\varphi - \Delta^{(w)}_{(o)}\varphi^{\theta})}{RT}) \qquad \textbf{(1.28)}$$

where $\Delta^{(w)}_{(o)}\varphi^{\theta}_{i}$ is the formal Galvani potential difference for ET

k^{θ}_{app} is the apparent rate constant (when $\Delta^{(w)}_{(o)}\varphi_{i} = \Delta^{(w)}_{(o)}\varphi^{\theta}_{i}$)

α is the apparent charge transfer coefficient given by $a = \frac{RT}{z_i F}(\frac{\partial \ln \overrightarrow{k}}{\partial \Delta^{(w)}_{(o)}\varphi})$

The analysis presented above was based on a model by Gavach *et al.* [70], where a compact layer of oriented molecules for both solvents exists at the plane of contact of the immiscible solutions, which separate the diffuse double layers and establish two planes of closest approach.

1.9.v Summary of some experimental investigations on ET

Several redox species for both phases have been used in the study of heterogeneous ET, based usually on ferrocene derivatives in the organic phase. The first experimental paper was presented by Samec in 1977[11], using four-electrode cyclic voltammetry to study ET between ferrocene in the organic phase and hexacyanoferrate in the aqueous phase. During the intervening years many different aspects of ET have been since explored experimentally:

a) Investigations of interfacial ET across a polarisable interface It is evident from the literature that certain different redox species and combinations can be employed in the case, with iron or cerium complexes as the most commonly used aqueous redox species. Table 1.2 indicates the range and interest of selected studies on ET over the last decade:

Table 1.2 Selection of experimental studies on heterogeneous ET with four-electrode technique

Main Author	Year	Organic *Redox*	Interest	Ref
Hanzlik	1987	Ferrocene (Fc)	IT/ET coupling	71
Geblewicz	1988	$Lu(PC)_2$	True ET	72
Kihara	1989	TCNQ, TTF	Thermodynamic analysis	73
Chen	1991	Ferrocene (Fc)	Rate of transfer	74
Cheng	1991	$Fe[TPP\text{-}(py)_2]$ $Ru[TPP\text{-}(py)_2]$	Change of $E^0_{(o)}$	75
Cunnane	1995	Dimethyl Fc DecaMethyl Fc	IT/ET coupling Complications	76
L'Her	1996	$Lu(PC)_2$	Diffusion kinetics	77
Suzuki	1997	TCl-BQ, diBr-BQ, MB^+	Polarography with ascorbic acid	78
Ohde	1998	Quinone derivatives	NADH reaction	79
Ohde	2000	TCNQ	O_2 reaction	80

b) Deposition of metal particles. The first experimental proof of metal deposition at a polarised aqueous/organic interface was by Guanazzi *et al.* in 1975 [81]. They showed that driving a current across an interface between an aqueous solution of $CuSO_4$ and a solution of tetrabutylammonium hexacarbonyl-vanadate in nitrobenzene resulted in the deposition of a copper layer at the interface between the two solutions. Cheng *et al.* [82] deposited gold particles at the interface by the electrochemical reduction of tetraoctylammonium tetrachloroaurate in DCE by aqueous $K_4Fe(CN)_6$. The process was studied with cyclic voltammetry as well as in-situ spectrophotometry and SEM. Evans and Cunnane studied the formation of conducting polymers at the liquid/liquid interface[83]. Lahtinen *et al.*[84] showed recently that electrochemically generated Pd nanoparticles at the liquid/liquid interface could be used as reductive photocatalysts by mediating heterogeneous ET. Johans *et al.* then provided a model and a rate law for the diffusion-controlled electrodeposition of metallic particles at the interface[85].

c) ET across a non polarisable interface induced by a partitioning ion

Scanning Electrochemical Microscopy (SECM) is a surface probe technique using moving ultramicroelectrodes tips at surfaces[86], that has been further developed to study the kinetics of charge transfer processes across the liquid/liquid interface [87]. Wei *et al.* [88] first used SECM to study the characteristics and kinetics of ET between ferrocene and $Na_3Fe(CN)_6$, obtaining the potential dependence of the ET rate constant by changing the concentrations of potential determining ion. Tsionsky *et al.*[89], studied heterogeneous ET between zinc 5,10,15,20-tetraphenyl-21H,23H-porphyrine (ZnPor) and $Ru^{III}(CN)_6^{3-}$. They concluded that conventional ET theories are applicable to the liquid/liquid interface, and calculated α for this reaction to be close to 0.5. A lot of work has been focused on the study of ET with SECM but will be reviewed further in Chapter 5.

Anson and Shi [90] developed a method for forming stable adherent thin layers of organic solvents between the surface of a graphite electrode and the aqueous electrolyte, with a partitioning ion that distributes itself between the two phases. They studied in this way the ET between the reductant organic species ferrocene, decamethylferrocene and the oxidants cobalt and zinc tetraphenylporphyrins by aqueous $Fe(CN)_6^{3-}$ and $Fe(CN)_6^{4-}$, $Ru(CN)_6^{4-}$ and $Mo(CN)_6^{4-}$. The observed rate constants differed from the findings of the SECM measurements[91,92] and this was attributed by the authors to ion coupling interfering with ET. A quantitative model was then developed by Barker *et al.*[93] for measuring the rate constants of electron transfer (ET) in similar systems showing that approximate treatment of the method is rarely applicable for typical experimental parameters reported in the work by Shi and Anson. This technique was also used by Shafer *et al.*[94] where various aqueous and organic redox species as well as different driving forces from partitioning single electrolytes were studied.

d) ET across adsorbed layers. Cheng and Schiffrin[95] showed that the ET reaction between the organic species Ru(TPP)(py)$_2$ and Lu(PC)$_2$ with aqueous $Fe^{II/III}(CN)_6$ is blocked by the adsorption of phospholipid layers at ITIES. They suggested that this was due to large distances between redox centres, and showed that when TCNQ was incorporated into the lipid layer it could act as a mediator for the reaction involving Ru(TPP)(py)$_2$. Tsionsky *et al.* [96] also investigated the effect of phospholipid adsorption on heterogeneous ET between zinc 5,10,15,20-tetraphenyl-21H,23H-porphyrine (ZnPor) in benzene and aqueous redox species, using SECM techniques. They found that phospholipid adsorption decreases the rate of interfacial ET, and that for a complete monolayer of phospholipid the heterogeneous rate constant was dependent on the number of methylene groups in the phospholipid chain. Delville *et al.* [97] also used SECM to study the effect of phospholipids containing conjugated chains on the rate of heterogeneous ET. They showed that in this case ET rates increase by at least a factor of 2 compared to films with only saturated hydrocarbon chains.

Amemiya *et al.*[98] recently presented a review of the SECM technique as well as a study of the charge transfer across a bilayer lipid membrane. They present results on the rate constant of ET that follow Marcus theory, including the inverted region. Lately, the effect of adsorbed non-ionic surfactants on ET was studied by Zhang *et al.*, using the SECM technique[99] to study the effect of Triton X-100 on the oxidation of DcMFc by aqueous $Ru(CN)_6^{3-}$and the MEMED technique[100] to study the effect of the same surfactant on the reduction of $TCNQ^-$ by $Fe(CN)_6^{3-}$. The diminution in ET rate with increasing surfactant concentration was consistent with Langmuirian adsorption of surfactant at the liquid/liquid interface, with the redox reaction occurring only at the portion of the interface free from surfactant.

e) ***In-situ*** **spectroscopic studies and photoinduced electron transfer.** Ding *et al.*[101] were the first to study spectroscopically heterogeneous ET between the organic species 7,7,8,8,-tetracyanoquinodimethane (TCNQ) and $K_4Fe(CN)_6$. This was carried out using *in-situ* UV-Vis spectroscopy keeping in mind that TCNQ has an absorption maximum at 390 nm and $TCNQ^{\cdot -}$ has a number of absorption bands in the 600-900 nm region. Plotting the absorption response versus the applied potential resulted in the shape of an ET voltammogram, denoting a method called voltabsortometry. They also studied the photon induced ET reaction of aqueous $Ru(bpy)_3^{2+}$ with TCNQ, demonstrating that the aqueous species transferred into the organic phase and reacted there homogeneously. They used the techniques of differential cyclic voltfluorometry and time-resolved total internal reflectance luminescence, to distinguish between species transferring at the same potential if one of them luminesces. Using the same technique they also studied [102] the photoinduced ET between the aqueous chromophore europium (Eu^{III}) and anthracene, which was found to take place heterogeneously. Lahtinen *et al.*[103] also presented an artificial photosynthesis system, where benzoquinone was photoreduced by water soluble porphyrins.

Heterogeneous ET for the reduction of TCNQ and the oxidation of 1-1' dimethylferrocene (DiMFc) by the aqueous $Fe^{II/III}(CN)_6$ couple was confirmed by Dryfe *et al.* [104], using *in-situ* UV-Visible spectrometry in total reflection mode. They showed a good correlation between optical and electrochemical responses, and a potential dependence of the rate constant. They also studied [105] the ET reaction of radical ions $TTF^{\cdot +}$ and $TCNQ^{\cdot -}$ with aqueous $Fe^{II/III}(CN)_6$, using for the first time a specially developed cell for *in-situ* EPR to monitor paramagnetic species at ITIES. They measured the change in signal intensity with respect to the potential difference at ITIES and then further modelled heterogeneous ET to biologically important quinones.

Kott *et al.*[106] studied photoinduced ET using the surface sensitive technique of optical second harmonic generation to monitor the change in the optical non-linearity at the interface, which resulted from ET. Fermin *et al.*[107], used the same technique to study the photoinduced ET between the water-soluble zinc terakis(carboxyphenyl)porphyrin and the organic redox species of ferrocene and diferrocenylethane. They developed a quantitative analysis of the photoinduced ET kinetics at the ITIES from the potential dependence of the photocurrent at various light intensities and aqueous porphyrine concentrations.

1.10 Coupling of ET and IT

In the study of charge transfers at liquid/liquid interfaces, electron transfer and ion transfer across the interface are frequently coupled, as can be seen from the following simple schematic. In this case the potential drop across the interface may be a mixed potential to which both ET and IT contribute. Whether IT or ET is the main reaction occurring depends on the relative concentrations of the partitioning constituent and the redox couples [43].

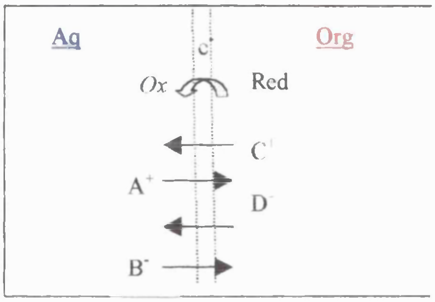

Kihara *et al.*[108,109] studied specific experimental systems to obtain spontaneous coupling of IT and ET, where the driving force is the electroneutrality of the system. The coupling of the two processes has also been studied by Kakiuchi [110,111], who developed a method for calculating the equilibrium inner potential difference between the two phases as well as the equilibrium concentrations of all the system components. The method takes into account initial concentrations for the ionic components A^+B^- and C^+D^- as well as the standard electrode potentials and standard IT potentials. Kakiuchi proposed that the aqueous/organic volume ratio itself appears to have a dramatic effect on the equilibrium. Generally, it was concluded that the partition of even small amounts of ions could significantly alter the initial conditions presumed for heterogeneous ET.

The system is defined by the following restrictive conditions:

a) Electroneutrality of both phases

$$\sum_i z_i c_i^s = 0 \qquad \textbf{(1.29)}$$

b) The mass balance equation for all the redox species,

$$V_{(w)}^0 c_{\mathrm{Re}d(w)}^0 + V_{(w)}^0 c_{Ox(w)}^0 + V_{(w)} c_{\mathrm{Re}d(w)} + V_{(w)} c_{\mathrm{Re}d(w)} = V_{(w)}({*c_{Ox(w)}} + {*c_{\mathrm{Re}d(w)}}) \qquad \textbf{(1.30)}$$

$$V_{(o)}^0 c_{\mathrm{Re}d(o)}^0 + V_{(o)}^0 c_{Ox(o)}^0 + V_{(o)} c_{\mathrm{Re}d(o)} + V_{(o)} c_{\mathrm{Re}d(o)} = V_{(o)}({*c_{Ox(o)}} + {*c_{\mathrm{Re}d(o)}}) \qquad \textbf{(1.31)}$$

where V$_{(s)}$ represents the volume of the solvent (s) and

* represents the initial concentrations.

c) The mass balance for all the other partitioning ionic components *i*:

$$V_{(o)} c_{i(o)} + V_{(w)} c_{i(w)} = V_{(o)} * c_{i(o)} + V_{(w)} * c_{i(w)} \qquad \textbf{(1.32)}$$

d) The distribution equilibrium of each component between the two phases given by the Nernst-Donnan equation:

$$\frac{c_{i,(o)}}{c_{i,(w)}} = \exp[\frac{z_i F}{RT}(\Delta_{(o)}^{(w)}\varphi_{Eq} - \Delta_{(o)}^{(w)}\varphi_i^0)] \qquad \textbf{(1.33)}$$

where $\Delta_{(o)}^{(w)}\varphi_i^0$ is the standard transfer potential for each ionic component

e) The redox potential difference is given by:

$$\Delta_{(o)}^{(w)}\varphi = E_{Ox/\mathrm{Re}d_{(o)}}^{\prime 0} - E_{Ox/\mathrm{Re}d_{(w)}}^{\prime 0} + \frac{RT}{n_1 n_2 F}\ln\frac{a_{ox^{(w)}} a_{\mathrm{Re}d^{(o)}}}{a_{Ox^{(o)}} a_{\mathrm{Re}d^{(w)}}} \qquad \textbf{(1.34)}$$

This set of equations can be solved for two cases:

- The partition of counterions of the redox species. This means that if there is a net flow of counterions between the two phases, it is counterbalanced by ET across the interface. The equilibrium inner potential difference was found to become more positive, the bigger the lipophilicity of the counteranion in the aqueous phase is. This means that the ET is driven by IT from the aqueous to the organic phase. Figure 1.3 shows the effect of the volume ratio $r=V^o/V^w$ on the equilibrium potential. When log*r* is small, $\Delta_{(o)}^{(w)}\varphi_{Eq}$ approaches the limiting value for the example used[110,111], whereas when V^w is small and log*r* is large there is a significant deviation (0.2 V).

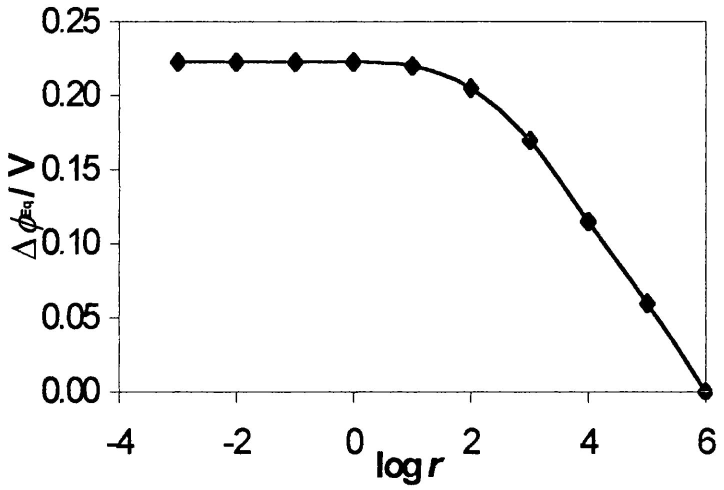

Figure 1. 3 Effect of the volume ratio *r*=V°/V^w on $\Delta_{(o)}^{(w)}\varphi_{Eq}$ for partition of counterions of redox species. (From reference 111)

- The partition of the indifferent ionic constituents (e.g. electrolyte ions). The ratio of the concentration of the indifferent ion to the concentration of the redox species, determined in this case whether the established equilibrium inner potential is determined only by the IT reaction, only by the ET reaction, or if it is an intermediate value determined by both reactions (mixed potential).

Kakiuchi argues that for experimental data during measurements that are made immediately after the contact of the phases (e.g. dropping electrolyte), the effects of ET/IT coupling are minimal, whereas when there is prolonged contact before measurement, then the ET/IT coupling, must be taken into account.

2.3 Scanning Electrochemical Microscopy (SECM)

Interfacial ET is studied indirectly in one phase by the depletion or production of the redox species involved. SECM is one of the scanning probe microscopies, used to monitor faradaic current at a "rastering" microelectrode, resulting from electrolysis of solution species at transport-controlled conditions. As the electrode tip is scanned near the interface a three-dimensional image of a surface is obtained where current variations are related to changes in topography or conductivity. Alternatively the technique can be used in a coupled mode, where the probe microelectrode/tip induces and monitors the interfacial processes of a target interface/substrate. In some cases instead of scanning the electrode in three-dimension, only the z-direction is used. When a microelectrode tip polarised at an appropriate potential, approaches an interface where no interfacial reaction occurs, the steady state tip current decreases due to a blocking effect of the "insulating" surface. In this case, as the tip approaches the interface, the tip current approaches to zero due to hindered diffusion of mediator species, as seen in Figure 2.1:

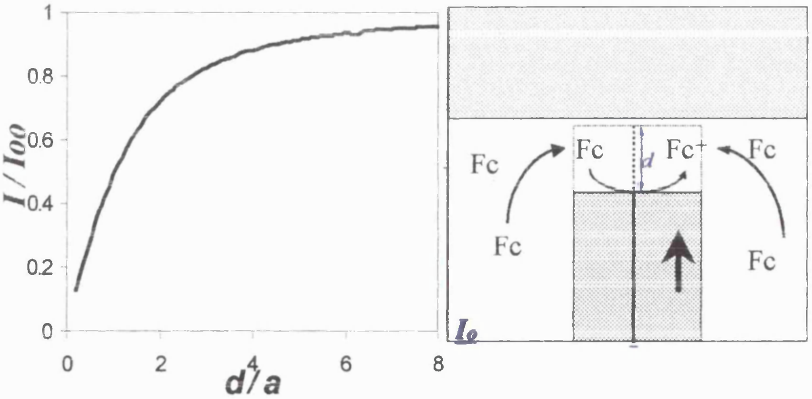

Figure 2. 1 Theoretical approach curve and a schematic for approach to an unreactive surface

Conversely, if the interface/substrate behaves as a conductor, i.e. there is a regeneration of the replenished species within the gap by an interfacial process, the tip current is enhanced. The magnitude of the current depends on the tip-substrate distance, the nature of the substrate, as well as the kinetics of the interfacial process. This is the reason why there are various "positive feedback" approach curves for different rate constants (Figure 2.2).

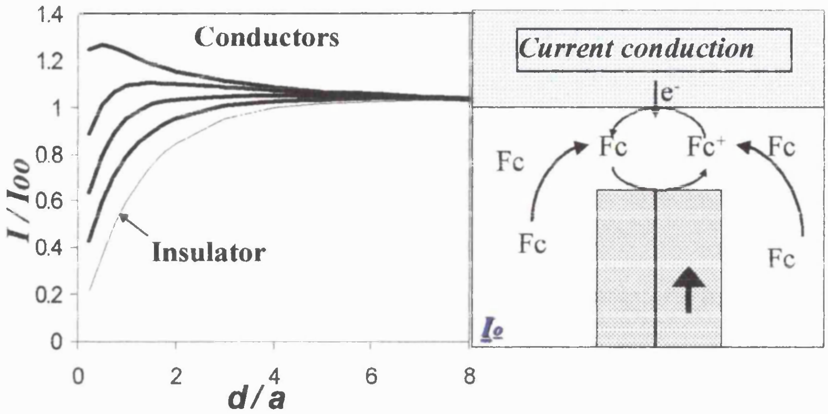

Figure 2. 2 Theoretical approach curves for various interfacial normalised rate constants (From botton to top K= 1, 10, 25,50, 75, 100) and a schematic representing feedback

The main advantage of using SECM as a probing technique is that it features the characteristics of dynamic electrochemistry where the current response is governed by the flux of reactants in the absence of problems such as ohmic drop, charging currents etc, observed in the four electrode experiments. This allows well-defined quantitative theory to be used for determination of various kinetics of interfacial or solution processes that take place. For some more information about the various principles and applications of SECM a variety of reviews and publications is available[112].

The diffusion equation and boundary conditions for the simulation of the SECM measurements are given in the work of Bard *et al.*[113]. The boundary conditions at $z=d$ (i.e. at the substrate), depends on the nature of the interface. For the enzyme system presented in Chapter 8, typical boundary conditions are[114]:

$$z = d\,,\ r \geq 0 \text{ then } \quad u_R = 1 \qquad \text{and} \qquad z = d\,,\ r \geq 0 \text{ then } \frac{\partial u_R}{\partial z} = 0 \qquad \textbf{(2.5)}$$

for a conductor and insulator respectively whereas for a first order irreversible reaction:

$$z = d\,,\ r \geq 0 \text{ then } \frac{\partial u_R}{\partial z} = -K(1 - u_R) \qquad \textbf{(2.6)}$$

with r and z denoting spatial co-ordinates in dimensionless form

(scaled to the electrode tip radius a)

and $u_R(r,z) = c_R(r,z)/c_R^*$ is the normalised concentration, with

c_R^* the bulk concentration of the reduced

Equation (2.6) presents the recycling from the oxidised form (o) of the mediator to the reduced form (R) by a first order irreversible heterogeneous reaction at the interface with a rate constant *K*. The relations $u_O = 1 - u_R$ and $\partial u_R / \partial z = -\partial u_O / \partial z$ are applied. The dimensionless rate constant *K* is connected to the rate constant in physical dimensions *k* by $K = ka/D$ where the assumption $D=D_R=D_O$ is used. For numerical solution, the condition: $0 \le z \le d$, $r \rightarrow x$ then $u_R = 1$ is used, where x denotes the radius of the electrode sheath. Experimental curves follow SECM theory up to a certain distance from the interface, depending on the experimental set-up (usually > 5μm). After this point deviations are always observed possibly due to capillary waves and electrostatic forces distorting the interface just before the probe electrode touches the interface. The theoretical simulations used in this project were carried out by Dr. Jörg Strutwolf.

2.4 Microelectrochemical measurements at an expanding droplet (MEMED)

MEMED is a technique recently developed by Unwin and Slevin[115] at Warwick University. It constitutes a special branch of SECM, where an expanding drop of one phase approaches a stationary microelectrode tip positioned in the other phase. Current is continuously measured as the interface of the drop approaches the microelectrode. The measured current-time approach curve *I-t* is translated to a concentration-distance, *c-d*, profile. The drop time is changed to distance:

$$t = \frac{DropVolume}{FlowRate} = \frac{(4/3)\pi r_D^{\,3}}{F.R.} \qquad \textbf{(2.7)}$$

where r_D is the expanding drop radius at time t and $d=2c-2r_D$ is the distance between the tip and the drop, and $2r_{Do}$ the final diameter of the drop at contact point, typically 1mm. The current is converted to concentration based on the equation for microelectrodes:

$$C = \frac{I}{4naFD} \qquad \textbf{(2.8)}$$

where D is the diffusion coefficient of the aqueous redox species,

a is the electrode radius and the rest of the variables are as already defined.

2.5 Impedance technique

The impedance technique that provides the double layer capacitance C_D is an established method for characterisation of the liquid/liquid interfaces. Each component of the electrochemical cell is translated to an equivalent electronic component of a circuit. The structure of the interface can be approached with this technique. Several topics like ionic adsorption through ion pair formation[116-118], IT kinetics[119] and ET kinetics[120,121], have been thus investigated. There have been reports that a simple electrical equivalent circuit is an oversimplification of the liquid/liquid interface[122] since it does not account for the experimental artefacts or the role of capillary waves at the interface. For the purposes of this work, these effects are considered negligible.

Impedance spectroscopy has its origin in early works of Debye[123]. At a polarised liquid/liquid interface the dc-potential that controls the cell is perturbed by an alternating potential:

$$E = E_0 + \Delta E \sin(\omega t) \qquad (2.9)$$

with ω the angular frequency, and ΔE a small amplitude

The resulting alternating current, which typically has some phase shift ϕ with respect to the perturbation is measured (Figure 2.3)

$$I = I_0 + \Delta I \sin(\omega t + \varphi) \qquad (2.10)$$

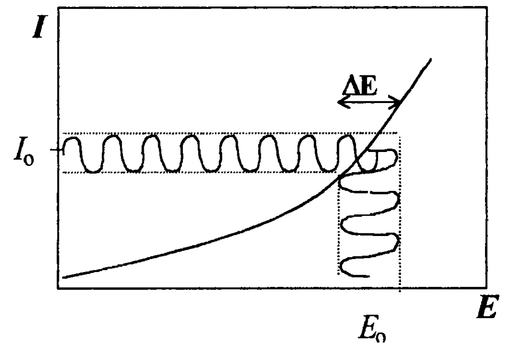

Figure 2. 3 Potential perturbation resulting in an alternating sinusoidal current

If the amplitude of the perturbation is small enough, the response is linear and a simple electrical equivalent circuit using linear components can be defined. As Ohm's law describes the relation between dc- potential and dc- current ($E=IR$), for the alternating components, the relation is $E_{AC}=I_{AC}Z$, with Z the electrochemical impedance provided by the cell. The impedance Z is therefore the proportionality constant (transfer function) between the *ac* current and *ac* potential, i.e. the opposition that the cell offers to the flow of *ac* current at a particular frequency. Z can be represented as a complex quantity:

$Z=|Z|\,e^{j\phi}$ or in Cartesian co-ordinates $Z = Z'-jZ''$, with $j=\sqrt{-1}$

with Z' being the real part, which is the *resistance* component R (in phase)

and Z'' the imaginary part, the *reactance* component $X_c=Z''$(out of phase)

The electrical response of a material that is neither purely resistive nor purely reactive, can be represented (at any specific frequency) as a combination of series and parallel combinations of a resistance (R) and a capacitance (C). Such a representation is called an equivalent circuit.

If the system under study could be represented only by a resistance, for example the ohmic resistance of the electrolyte solution, then it would provide an impedance that would change only the magnitude of the signal. In contrast, if the system is represented by a capacitance, then there is a phase shift of the signal, shown in Figure 2.4:

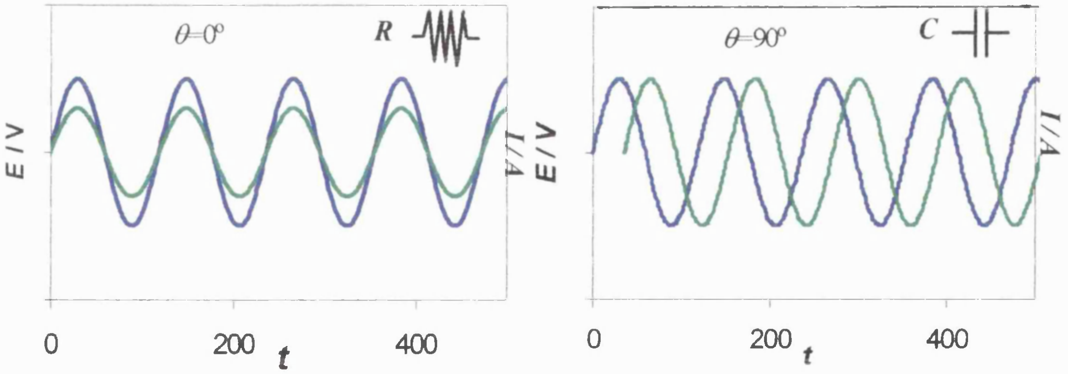

Figure 2. 4 Effect of different cell components on the resulting alternating current (blue line) following an alternating potential perturbation (green line)

Capacitance C, is related to *reactance* X_C:

$$Z'' = X_C = \frac{1}{\omega C} = \frac{1}{2\pi f C} \qquad \textbf{(2.11)}$$

where f is the frequency of the applied disturbance.

Conductance, is the reciprocal of resistance ($G=1/R$) and *susceptance* the reciprocal of reactance ($B_c=1/X_c$). In some cases due to non-ideal situation, resulting from roughness, or heterogeneity of the cell, instead of a simple capacitance the reactance takes the form of a constant phase element (CPE): $Z''_{CPE} = -j/(\omega Q)^n$. For ideal situations as assumed in this work $Q=C_D$ and n=1.

Admittance Y^* is the reciprocal of impedance Z and is given by:

$$Y^* = Y' + jY'', \qquad \textbf{(2.12)}$$

where Y' the real part and Y'' the imaginary part

When there are charge transfer reactions involved in an electrochemical cell, such as the liquid/liquid interface, the diffusing species that take part in the processes offer an extra impedance term called concentration impedance. This circuit element is called the Warburg impedance:

$$Z_W = \frac{\sigma_W(1-j)}{\sqrt{\omega}} = \frac{\sigma(1-j)}{\sqrt{2\pi f}} \qquad \textbf{(2.13)}$$

where σ_W is the Warbourg coefficient, dependent on the square root of diffusion coefficient $\sqrt{D}$ of the species, involved in the charge transfer process.

Finally inductance L, is the circuit element of a device that resists the change in the current going through it, with similar attributes as the capacitance but with opposite result, introducing a delay to the signal, which therefore has a phase lag.

Table 2.1 summarises the characteristics of some of the standard electrical circuits used for the description of electrochemical systems, together with the complex plane plots (-*Z*"-*Z*') and the Bode plots (log-log) typical of the equivalent circuits.

Table 2.1 Standard electrochemical circuits and their characteristics

Circuit	Cell equivalence	Impedance	Complex Plot	Bode Plot
Capacitance 	EDL Capacity C_D	$Z'' = -\frac{j}{\omega C} = -\frac{j}{2\pi f C}$	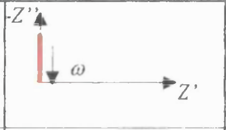	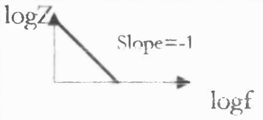
Series 	EDL Capacity(C_D) and Electrolyte Resistance (R_E)	$Z'' = R_E - \frac{j}{\omega C}$	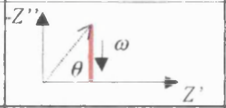	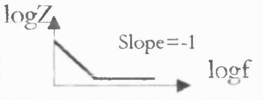
Parallel 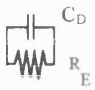	EDL Capacity(C_D) & CT reaction with Polarisation Resistance (R_P)	$Z'' = (\frac{1}{R_P} - j\omega C_D)^{-1}$	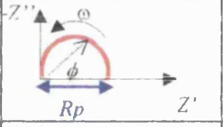	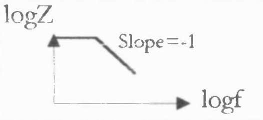
Combination 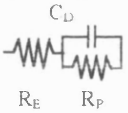	EDL Capacity(C_D), CT Resistance(R_P) and Electrolyte Resistance (R_E)	$Z'' = R_E + (\frac{R_P}{1+\omega^2 C_D^2 R_P^2} - \frac{\omega C_D R_P^2}{1+\omega^2 C_D^2 R_P^2})$	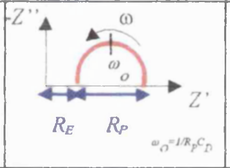	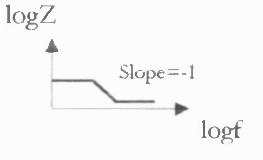
Randles 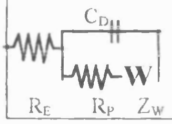	EDL Capacity(C_D), CT Resistance(R_P), Electrolyte (R_E) and Warburg (Z_W)	$Z' = R_E + \frac{1}{j\omega C_D + \frac{1}{R_P + Z_W}}$	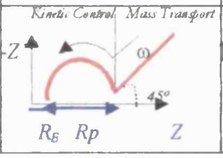	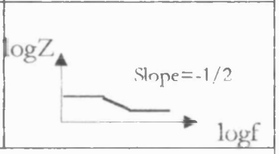

A resistance would appear as a single point on the x-axis of the complex plane, with *Z*=*Z*'=R. Generally, the analysis of the impedance measurements is not very straightforward, mainly because most of the systems examined do not exhibit an ideal behaviour.

2.6 Surface tension

The method used for the determination of the surface tension of various systems during this work was the ring method, an easy and widely used technique. It simply involves the determination of the force to detach a ring of wire, platinum in this case, from the surface of a liquid. It is attributed generally to De Noüy [124] and belongs to a family of detachment techniques, of which the drop weight and the Willhelmy plate are also examples. As with all the detachment methods, it is assumed that a first approximation to the detachment force is given by the surface tension multiplied by the periphery of the surface detached. Therefore for a ring[129]:

$$W_{tot} = W_{ring} + 4\pi R\gamma \qquad \textbf{(2.14)}$$

where *W* is the weight, *R* the ring's diameter and γ the surface tension

For equation (2.14) tables of empirical correction factors are used, which depend on two dimensionless ratios related to the resulting meniscus volume and the radius of the ring itself[129]. A zero or near zero contact angle is necessary, to prevent underestimation of γ. This was found to be the case with surfactant solutions where adsorption on the ring changed its wetting characteristics, and where liquid/liquid interfacial tensions were measured. The analysis of the results is based on the variation of γ with ln(*c*). Values of surface tension for concentrations less than the critical micelle concentration (CMC) can be well described with a quadratic equation, $\gamma = \gamma_0 + a\ln(c_b) + b(\ln(c_b))^2$. Therefore at each concentration, tangents to this functions can be used to obtain the surface excess Γi using the Gibbs equation:

$$\Gamma = -\frac{1}{RT}\frac{d\gamma}{d\ln(c)} = -\frac{1}{RT}(a + 2b\ln(c_b)) \qquad \textbf{(2.15)}$$

2.7 Specular neutron reflection technique

The neutron reflection technique is a very sensitive and accurate technique that has been used for the study of proteins at the water/air interface[130-132]. The high resolution of neutron reflectivity allows a reliable determination of protein layer density distribution perpendicular to the surface. Therefore measurements of the area/molecule, as well as its layer thickness determined with a few Angstrom resolution can be obtained. These structural parameters in conjunction with the known dimensions of the globular structure of the enzyme, can provide an insight about the physical state, the conformation, the extent of immersion in water and reorientation of the protein within the adsorbed layer.

The neutron reflection method is based on the variation in specular reflection *R*, as a function of the momentum transfer *Q*[133], defined as

$$Q = \frac{4\pi}{\lambda}\sin\theta_0 \qquad \textbf{(2.16)}$$

with θ_0 the glancing angle of incidence and λ the wavelength of neutrons, typically in the range of 3-6 Å. The specular reflectivity R(*Q*) is determined by the variation in scattering length density ρ(z) along the surface normal direction. For an interface between two bulk media, *R*(*Q*) can be described by Fresnel's law:

$$R(Q) = \left|\frac{(n_0 \sin\theta_0 - n_1 \sin\theta_1)}{(n_0 \sin\theta_0 + n_1 \sin\theta_1)}\right| \quad \text{and by}$$

$$= \frac{16\pi^2}{Q^2}\left|\hat{\rho}(Q)\right|^2 \qquad \textbf{(2.17)}$$

where n_0 and n_1 are the refractive indices if the two phases, θ_1 the angle of the transmitted wave, with $\hat{\rho}(Q)$ the one dimensional Fourier transform of ρ(z):

$$\hat{\rho}(Q) = \int_{-\infty}^{\infty} \exp(-QZ)\rho(z)dz \qquad \textbf{(2.18)}$$

The scattering length density ρ(z) is related to chemical composition through: $\rho(z) = \sum n_i b_i$, where n_i is the number density of element *i* and b_i the scattering length. Since different isotopes (e.g. H, D) have different b_i values, the use of isotopic substitution may result in a variety of neutron reflection profiles for a given layer. Values for scattering lengths, b_i, of the most common atoms used are given in Table 2.2. The most useful combination is often achieved by exchanging deuterium for hydrogen. The contribution to the reflection from bulk solvent can be removed by using null reflecting water (NRW) which contains 8.1% (v/v) D_2O with a resulting zero scattering length density.

Table 2.2 Coherent scattering lengths of atoms, 1 fm=10^{-15}m

Nucleus	AW	*b*(fm)
H	1.008	-3.739
D	2.016	6.671
C	12.011	6.6446
N	14.007	9.36
O	15.999	5.803
P	30.974	5.13
S	32.065	2.847

The profiles obtained are usually analysed by means of optical matrix formalism based on the following procedure[134]. An assumption for a structural mode is made for the adsorbed layer, followed by calculation of the reflectivity, based on the optical matrix formula. The calculated reflectivity is then compared with the measured data and the structural parameters (number of layers, thickness τ and density ρ of each layer) are varied in a least-squares iteration until a best fit is found. From the estimated structural parameters above, the volume fraction of the adsorbed species can be estimated from:

$$\rho = \rho_P\phi_P + \rho_W\phi_W \quad = \rho_P\phi_P + (1-\rho_P)\phi_W \qquad \textbf{(2.19)}$$

with ρ_W (=0 for NRW) and ρ_P the scattering length density of water and protein respectively, whereas ϕ_W and ϕ_P their respective volume fractions.

The area per molecule (A) of the adsorbed protein can be calculated:

$$A = \frac{\sum m_i b_i}{\rho \tau} \qquad \textbf{(2.20)}$$

with m_i the number of the ith atom and $\sum m_i b_i$ the total scattering length of the protein. Alternatively the surface area can be estimated by $A=(V_P+nV_W)/\tau$, with n the hydration number and V the water's or protein's (excluding water molecules) volume. In this case the volume fraction for the protein is $\phi_P=V_P/A$, and the surface excess, Γ, can be estimated:

$$\Gamma \quad = \frac{1}{N_A A} \ (\Gamma \text{ in mol m}^{-2}) = \frac{10^{20}}{N_A A} \ (\Gamma \text{ in mg m}^{-2}) = \frac{MW}{6.02A} \qquad \textbf{(2.21)}$$

where MW is the protein's molecular weight.

The equations presented here apply under the condition of a uniform layer distribution, yet they are directly applicable to each of the sublayers that may be present in the model. The total adsorbed amount is obtained by summing over the sublayers used in the fitting procedure. Meanwhile, at the water/air interface, there is always a contribution to the measured thickness of the layer from the thermal motion of the surface (capillary waves)[135]. The relationship between the total measured thickness τ and the capillary roughness w (Å) is given approximately by:

$$\tau^2 = \sigma^2 + w^2 \qquad \textbf{(2.22)}$$

where σ (Å) is the intrinsic thickness of the layer.

The amplitude of the thermal motion in a pure liquid is inversely proportional to the surface tension of the liquid. For pure water, the root mean square amplitude of thermal motion at 298K is estimated to be 2.8 Å and in terms of Gaussian distribution, usually employed, this is equivalent to a value of w=7 Å. The thermal roughness is thus estimated, and usually found to have negligible effect, within experimental error, on the total measured layer thickness without affecting the estimated protein's width either. The fitting to theory for the neutron experimental data was carried out by Dr. T.J. Su and Prof J.R. Lu.

Chapter 3: Experimental set-up

3.1 Introduction

This chapter gives the detailed methodology used for the work presented in this thesis. It is organised as follows:

- Synthesis - characterisation of organic electrolytes with Mass Spectroscopy-MS
- List of individual components and establishment of potentials.
- Preparation of reference electrodes and fabrication of working microelectrodes and their characterisation with Scanning Electron Microscopy (SEM), microscope imaging for electrode checking and video imaging for positioning.
- Ultraviolet-Visible (UV-Vis) spectroscopy to clarify possible side-reactions and the spectroscopy of the enzyme and mediators used.
- Impedance spectroscopy to determine the electrical double layer capacitance of the interface, in the absence and presence of surfactants and enzyme.
- Surface tension measurement for the determination of the surface excess in the presence of surfactant or enzyme layer.
- Specular neutron reflection for accurate determination of protein layer density distribution along the surface normal direction of water/air interface, as well as the determination of mono- or multi-layer thickness and the extent of mixing.
- Cyclic voltammetry with microelectrodes to determine the redox potentials of the redox species (aqueous and organic) studied in their respective phase and the effect of surfactants on these separate processes.
- Four electrode voltammetry to study heterogeneous ET across an ideally polarisable interface, between the two phases separately studied above, and the effect of surfactants on it.
- Scanning Electrochemical Microscopy (SECM) and its variation Microelectrochemical measurements at an Expanding Drop (MEMED), for the study of ET in the absence and presence of adsorbed surfactants and enzymes

3.2 Chemicals

3.2.i Solvents

Water used for the aqueous phase as well as for washing of glassware, was filtered using an ion exchange resin, then distilled, followed by treatment with a Millipore Q-Plus water purification system to remove both ionic and organic impurities. The non-aqueous solvent used in all ITIES experiments during this work was 1,2-dichloroethane (DCE) (99.5%, Fluka, Analar grade), which was used as received.

When indicated, the aqueous or organic solutions prepared were degassed with Ar and/or filtered prior to use and were further used at ambient temperature. All chemicals were weighed in their respective flasks made up with the required solvent. The solvents used for the preparation of the organic electrolytes were absolute ethanol (BDH, Analar) and acetone (BDH, Analar).

3.2.ii Supporting Electrolytes

Several aqueous supporting electrolytes were used for different systems and will be indicated separately for each cell: lithium sulphate (Li_2SO_4, BDH, Analar), lithium chloride (LiCl, Aldrich 99%), tris sodium citrate (Na_3Cit, BDH, Analar), dipotassium hydrogen phosphate (K_2HPO_4) and potassium dihydrogen phosphate trihydrate (KH_2PO_4-$3H_2O$) (Fluka Reagent grade).

Most of the organic supporting electrolytes C^+A^- used had to be synthesised, by mixing equimolar amounts of C^+Cl^- and Na^+A^- , (both Analar grade, purchased from Aldrich) in a 1:2 mixture of ethanol/water mixture, followed by washing thoroughly with H_2O and recrystallising twice from acetone. Therefore, a series of organic electrolytes were prepared in this way (Table 3.1) oven dried and kept dry in a dessicator, together with the commercially available ones.

Table 3.1 Organic electrolytes used and their origin

Organic electrolyte	**Preparation with acronyms**
Tetraethylammonium tetraphenylborate	TEA - TPB from TEACl + Na TPB
Tetrapropylammonium tetraphenylborate	TPrA- TPB from TBACl + Na TPB
Tetrabutyllammonium tetraphenylborate	TBuA- TPB from TBuACl + Na TPB
Tetrahexylammonium tetraphenylborate	THexA-TPB from TBACl + Na TPB
Tetraphenylarsonium tetraphenylborate	TPAs- TPB from TPAsCl + Na TPB
Bis(triphenyl)phosphoranylidine tetraphenylborate	BTPPA-TPB from BTPPACl + NaTPB,
Tetraheptylammonium tetraphenylborate	THepA-TPB (Fluka, Chemica)
Tetramethylammonium perchlorate	TMA- ClO_4 (Fluka, Chemica)
Tetraethylammonium perchlorate	TEA- ClO_4 (Fluka, Chemica)
Tetrapropylammonium perchlorate	TPrA- ClO_4 (Fluka, Chemica)
Tetrahexylammonium perchlorate	THexA- ClO_4 (Fluka, Chemica)

The structure of the organic ions used during this study is shown in scheme 3.1:

Scheme 3.1 Chemical structure of the organic electrolyte ions

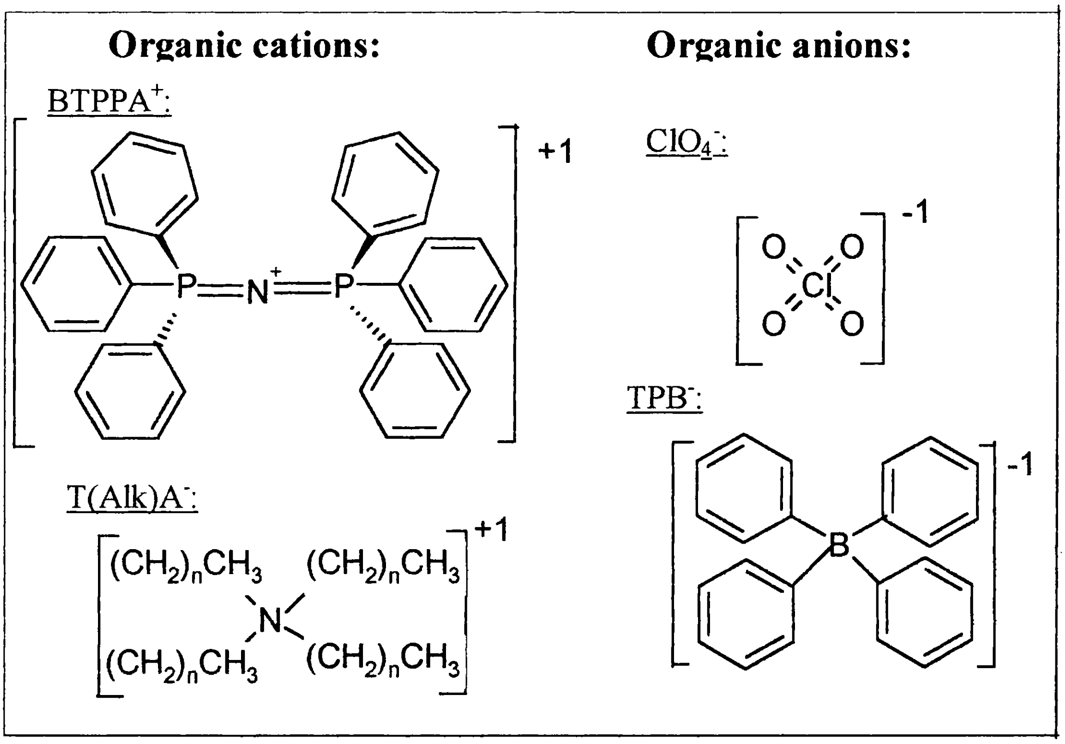

Some of the organic electrolytes and their purity, was further characterised using mass spectrometry (Electron Ionisation, EI, Fast Atom Bombardment, FAB, and Negative Electrospray, ES).

For the main organic electrolytes that were synthesised as described above the MS spectra, shown in the Appendix II resulted in the following data:

$\underline{BTPPA^+}$ m/z (FAB$^+$): 538 (M$^+$, 100% cation), 460 (M-C_6H_6, 5%), 384 (M-2(C_6H_6), 7 %), 183 (M- 4(C_6H_6)NP, 9%)
$\underline{TPrA^+\ TPB^-}$ m/z (EI$^+$): 186 (100% $\underline{TPrA^+}$), 164 (84%), 114 (100%, -Ph), 78 (54%Ph), 51(10%) 41(25%) ,30 (22%)
$\underline{TPB^-}$ m/z (ES$^-$) 319 (M$^-$, 100% anion)
The above results indicate that there are limited impurities in the electrolytes synthesised and starting materials were absent.

3.2.iii Potential Determining Ions and Single Electrolytes

Some of the organic electrolytes mentioned above were also used for SECM experiments, as potential determining ions (PDI) in order to establish a potential difference across the interface. The potential is established either by a common cation C^+, when the organic electrolyte C^+A^- is in the organic phase and C^+Cl^- is in the aqueous phase or by a common anion A^-, with C^+A^- is in the organic phase and Na^+A^- in the aqueous phase. Changing the ratio of the common ion concentrations in either phase can alter the potential established, as was described in Chapter 1. A selection of the possible potential values established by the various PDI, most of which were explored in different ratios during the present study are given in Table 3.2.

When an electrolyte itself is soluble in both phases, such as the perchlorates, (TEA-ClO_4, TPrA- ClO_4, THexA-ClO_4) the term "single electrolyte" (SE) is used. In this case both ions act as potential determining ions and the established potentials for various SE are also given in the Table 3.2, where $\Delta\phi_{SE}=0.5(\Delta\phi_i+\Delta\phi_j)$.

Table 3.2 Potential determining ions and electrolytes with established potentials

PDI	$\Delta\phi^0_i$/ mV	PDI	$\Delta\phi^0_i$/ mV	SE	$\Delta\phi^0_i$/ mV
TPB	364	TFB$^+$	-185	TMAClO$_4$	3
Cs$^+$	360	TBuA$^+$	-225	TEAClO$_4$	-67
TMA$^+$	182	TpeA$^+$	-360	TEATFB	-71
TEA$^+$	44	TPAsA$^+$	-410	TPrAClO$_4$	-130
TPrA$^+$	-91	BTPPA$^+$	-420	TBuATFB	-200
ClO$_4^-$	-178	THexA$^+$	-494	TBuAClO$_4$	-210

The ions and salts of Table 3.2 are given with the acronyms established in Table 3.1. The values given are taken either from literature[136], or were calculated from the Gibbs energy of transfer, based on the tetraphenylarsonium-tetraphenylborate assumption. Based on the values for the standard Galvani potential difference, $\Delta\phi^0_i$, the value of the interfacial potential difference established can be estimated using the appropriate ratios in respective phases. In the present study, most of the activity coefficients, unless otherwise stated, were assumed to be 1(see Appendix 1). The different ratio chosen for the ions in their respective phases may result in a considerable potential change, notably 18 mV (2:1), 30 mV (3:1), 60 mV (10:1), 118 mV (100:1) etc.

An appropriate PDI or SE for the purposes of this project should ensure an equilibrium potential that is higher than the transfer potential of the ions involved in the organic phase, i.e. $\Delta\phi > \Delta\phi^{org}_{IT}$, and lower than the transfer potentials of the ions in the aqueous phase $\Delta\phi < \Delta\phi^{aq}_{IT}$. $\Delta\phi$ is the potential difference established for the aqueous phase with respect to the organic phase. Furthermore it must ensure that it maintains or enhances the driving force of interfacial ET, ie. $\Delta E = E_{acceptor} - E_{Donor} > 0$. Extra care must be paid to distinguish which species is oxidised interfacially to determine favourability. In the case that the organic species is oxidised, with an electron donated to the aqueous phase, favourability is maintained when $\Delta E + \Delta\phi > 0$, and therefore $E^o_{aq} + \Delta\phi > E^o_{org}$, or vice versa.

3.2.iv Redox couples

The hydrophobic organic reductant species chosen for this study were various ferrocene derivatives: ferrocene (Fc, Aldrich, Reagent Grade), 1,1'-dimethylferrocene (DiMFc, Strem chemicals) and decamethylferrocene (DeMFc, Strem chemicals).

Various aqueous redox couples were explored in different ratios: hexacyanoferrate $Na_3[Fe^{III}(CN)_6]/Na_4[Fe^{II}(CN)_6]$ (Analar BDH) and $K_3[Fe^{III}(CN)_6]/K_4[Fe^{II}(CN)_6]$ (Sigma, ACS Reagent), iron-citrate $Fe_2/_3SO_4$-Na_3Cit (Analar BDH), hexacyanoruthenate $K_3[Ru^{III}(CN)_6]/K_4[Ru^{II}(CN)_6]$ (Aldrich), and hexaamineruthenium $Ru^{III}(NH_3)_6Cl$ /$Ru^{II}(NH_3)_6Cl_2$ (Aldrich), all used as received. The comparative scale given in Table 3.3 for the standard redox potentials, E^0, of various aqueous and organic redox couples was used in order to design most of the experiments presented in the next chapters.

Table 3.3 Redox potentials of aqueous* and organic** species

Organic red/ox species	$E^o_{(o)}$ /V vs SHE	$E^o_{(w)}$ /V vs SHE	Aqueous red/ox species
ZnPOr	0.800	0.870	$Ru(CN)_6^{3-}/Ru(CN)_6^{4-}$
Ferrocene (Fc)	0.615	0.650	FcCOONa
		0.490	$Fe(CN)_6^{3-}/Fe(CN)_6^{4-}$
Dimethylferrocene (DiMFc)	0.485		
Tetracyanoquinodimethane (TCNQ)	0.220	0.090	$Fe(Cit)_3^{3+}/Fe(Cit)_3^{2+}$
		0.065	$Ru(NH_3)^{3+}/Ru(NH_3)^{2+}$
		0.030	Methylene Blue
Decamethylferrocene (DecaMFc)	0.055	0.010	$NAD/NADH_2$
		-0.136	$FAD/FADH_2$
Ubiquinone (UQ)	-0.243	-0.220	Anthraquinone/Hydroquinone

*Literature values from *Handbook of Chemistry*, CRC Press, 57th edition

**Formal potentials based on experimental measurements against Fc^+/Fc couple[137]

The values of the aqueous standard potentials in Table 3.3, are for pH=7, and T=25 °C, and have a very strong ionic strength and pH dependence, i.e. for the ferro/ferricyanide couple a value of 0.460 mV is given for alkaline pH and 0.690 mV for acidic pH. For the purposes of the four-electrode studies the aqueous redox couple is present in high concentrations and various ratios that establish the equilibration potential E_{eq}. This equilibrium potential E_{eq}, will remain almost constant during ET, thus allowing the aqueous phase to act in the same way as a metal electrode, and donate/accept electrons from the organic phase. For this reason a Pt pseudo-reference electrode is used in the aqueous phase. The potential difference established between a Pt wire electrode and a reference SCE can indicate the rest potential, E_{Rest} established by different concentration ratios of the aqueous species. This can be then corrected to the standard hydrogen scale, to give the equilibrium potential, E_{Eq} presented in Table 3.4:

Table 3.4 Measured equilibrium potentials for various ratios in 1.5 M $LiSO_4$

$C_{Fe^{(III)}(CN)_6}/M$	$C_{Fe^{(II)}(CN)_6}/M$	Ratio	E_{Rest} /V (Pt vs.SCE)	E_{Eq} /V (Pt vs. SHE)
0.1	0.001	100/1	0.369	0.611
0.1	0.01	10/1	0.302	0.545
0.1	0.02	5/1	0.295	0.537
0.1	0.025	4/1	0.289	0.531
0.1	0.05	2/1	0.272	0.514
0.1	0.1	1/1	0.246	0.488
0.05	0.1	1/ 2	0.236	0.478
0.025	0.1	1/ 4	0.221	0.463
0.02	0.1	1/ 5	0.214	0.456
0.01	0.1	1/ 10	0.198	0.440
0.001	0.1	1/ 100	0.136	0.380

As expected the Nernst equation describes the relationship between the established equilibrium potential and the logarithm of the concentration ratio, as shown in Figure 3.1. The reproducibility of the measurements allowed a ±10mV error. The solutions need to be freshly made.

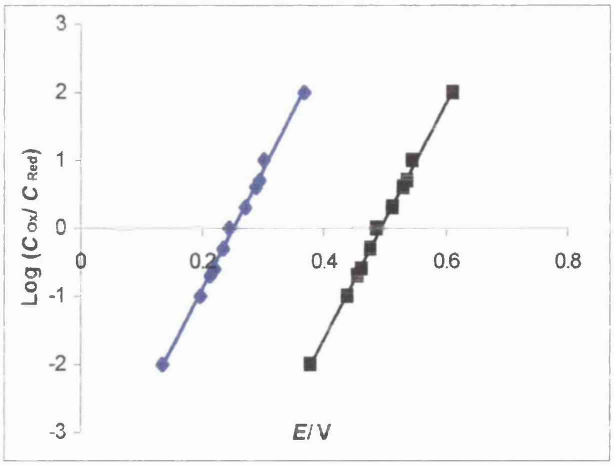

Figure 3. 1 Nernst equation for the ferrocyanide redox couple for potentials vs SCE (diamonds) and SHE (squares) with their standard potential $E° = 0.48V$ for alkaline pH.

3.2.v Surfactants

Five different surfactants were tried, the non-ionic surfactants, shown in Scheme 3.2, Triton X100 (Aldrich), and Sorbitan monostearate (SM, Aldrich), the cationic cetyl trimethyl ammonium bromide (CTAB, Aldrich) and cetyl trimethyl ammonium p-toluenesulfonate (CTA-pTS, Aldrich) and the anionic sodium dodecylsulphate (SDS, Aldrich). Adding the CTAB to the aqueous phase led to emulsification, which consequently excluded the study of this ionic surfactant on the electron transfer reaction. This is probably due to the salting out of one of the ions used in the solution. A dense stock solution of surfactants was prepared and consecutive additions were injected with an automatic pipette to the system under study. The critical micelle concentration (CMC) of Triton X-100 is found in the literature to be $3\text{x}10^{-4}$ M, whereas for CTAB it is $9.2\text{x}10^{-4}$M. The addition of the surfactant in the total volume is not taken into account, as it gives an error of only 1~2 %. On the other hand very low surfactant concentrations are not ideal, as there is a possible adsorption of the surfactant on the vessel walls. Ideally a certain time should be allowed for maximum adsorption of the surfactant at the interface. As can be seen in Scheme 3.2 the long alkyl chains are the hydrophobic part of the surfactants that remains in the organic phase, while the polar hydrophilic heads protrude in the aqueous phase. Triton X-100 was water-soluble whereas SM was soluble only in the organic phase. When the surfactant were not studied in their respective phases, sonication of the solutions was followed by filtration.

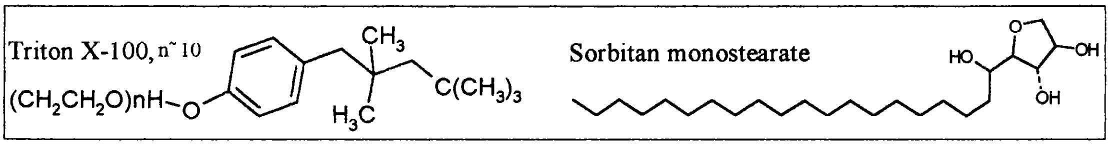

Scheme 3.2 Chemical structure of the non-ionic surfactants, used in the present study

3.2.vi Enzyme

The enzyme used for all experiments was glucose oxidase, GOx, (ex Aspergillus Niger) purchased from Bioenzyme UK and Fluka and stored at –20 °C. GOx was chosen as it is very stable and specific to its substrate, glucose (Aldrich, Analar Grade). Solutions were prepared in phosphate buffer, which was adjusted to pH=7, using appropriate phosphate concentrations, (K_2HPO_4 -$KH_2PO_4.3H_2O$).

3.3 Experimental Set-up

The pH was measured using a standard pH-meter. All electrochemical measurements were carried out in Faraday cages, constructed in-house, in order to eliminate electronic noise and vibrations. The cages were grounded by earthing through the electrical supply. The sign convention used throughout this work is that the potentials reported are those of the aqueous phase with respect to the organic phase. Therefore a positive current corresponds to the transfer of positive charge from the aqueous to the organic phase.

3.3.i Preparation of electrodes

The Ag/AgCl reference electrodes were electrochemically prepared by driving a current density of 1mA per cm^2 through a silver wire immersed in a continuously stirred 0.1 M HCl solution. The technique of chronocoulometry was used in a two electrode configuration, with the clean Ag wire acting as a working electrode and a clean Pt wire as the counter + reference electrode. The two electrodes have to be parallel in solution and the time taken to coat the necessary area of the wire is estimated by the charge flow required to dissolve 20 % of the silver wire, e.g. for 4 cm of immersed Ag wire (d= 0.125mm) 0.15 mA of current is passed for 150 min. Once the coating was even, the magnitude and stability of the electrode potential was checked in 0.1 KCl vs SCE. The electrodes were then washed thoroughly and stored in a low concentration chloride solution. The Ag/AgCl electrodes were also used in the reference junction of the organic phase, see Figure 3.1.a.

The saturated calomel reference electrodes were also fabricated, (Figure 3.2) with the procedure carried out in a fume-cupboard, taking extra care while handling mercury. Drops of Hg were added in a glass sample tube, with 2 ml of KCl and two spatula-full of Hg_2Cl_2 and were mixed into an even viscous paste with a wooden spatula. Two purpose made glass compartments were prepared, compartment A with a holed screw cap at top and a frit on the bottom, and compartment B with an open top and a 1 cm Pt wire collapsed at the bottom to provide a connection. Hg was added to compartment B in order to cover the Pt wire, followed by the paste and glass wool, taking extra care to exclude any air bubbles. Compartment B was filled to the top with saturated KCl, and so was compartment A, where some KCl crystals were also added. B was carefully tipped over and inserted in compartment A, with the Pt connection sticking out and the screw cap keeping it in place. The electrode was thoroughly washed with H_2O and kept in a saturated KCl solution, to prevent Cl^- from leaking out.

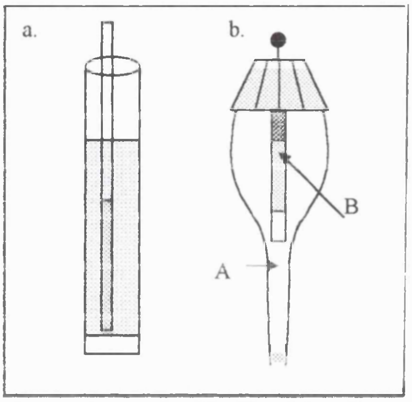

Figure 3. 2 Reference electrodes, a. Ag/AgCl with reference junction and b. SCE

The normal and "hook" Pt microelectrodes were fabricated by collapsing capillary glass on Pt wire. The glass melting point tubes were firstly soaked in acetone and thoroughly dried. "Normal" Pt microelectrodes were prepared with radius r=12.5 and 50 μm Pt, while the "hook" ones used for the SECM experiments were Pt and 10% Ir, of radius r=12.5 μm, 90%. In both cases, a piece of Pt wire (2cm) was cut and half inserted in the glass tube. The hook electrodes were sealed with the aid of a Bunsen burner. Using rubber tubing connected to the open end, the sealed end of the glass tube was rotated over a Bunsen burner. A suction collapsed about 1 cm of the glass around the Pt in the tube still leaving some uncovered wire for connection. The glass tube was inserted again in the oxidising flame of the Bunsen burner and was bent into shape with the aid of tweezers. For the normal electrodes, a capillary was pulled by a pipette puller, and sealed at the end using again a Bunsen burner. The sealed capillary with the inserted Pt wire was then placed within a heatable coil, and connected to an oil vacuum for 20-30 min. The coil was then heated slowly to high temperature and while rotating the capillary, the glass collapsed around the Pt wire.

A small piece of indium wire (1 cm) was inserted in both types of electrode, and a long chromium wire (10 cm) was added on top. The glass tube was inserted for the last time in the flame and the In wire melted to create a connection between Pt and Cr wires. The top of the glass tube was then sealed off with epoxy. The collapsed end was ground flat with sandpaper (P405), and/or a rotating diamond disk mounted on the platter of a computer disc drive. The microelectrodes were then polished consecutively with three grades of alumina 1.0 μm, 0.3 μm and 0.05 μm (Buehler, UK) on a microcloth (Buehler, UK). The last two grades were always used as well prior to every measurement. The microelectrodes were washed thoroughly with H_2O and acetone and kept in H_2O. Electrodes were always checked under the microscope prior to use in electrochemical measurements to determine RG, which is the ratio of the radius of surrounding glass sheath to electrode radius (Figure 3.3):

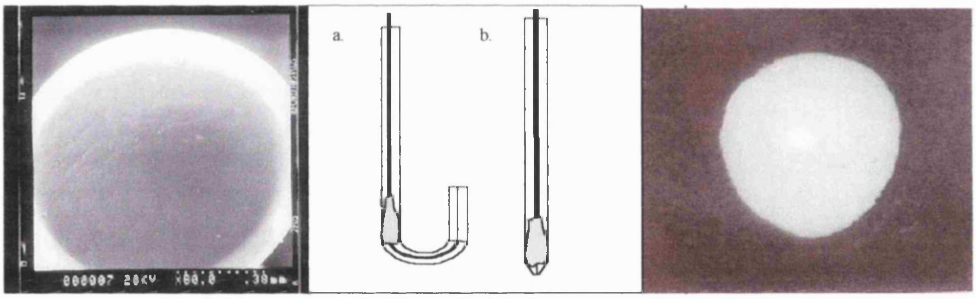

Figure 3. 3 a. Pt "hook" microelectrode (r=25μm) with RG=40, established by SEM picture (left)b. Straight Pt microelectrode (r=25μm) with RG=10, with microscope image photo (right)

A reference scale is given for testing electrodes, keeping in mind that the different pH, temperature, electrolyte type and concentrations could alter the indicative values given in the schematic:

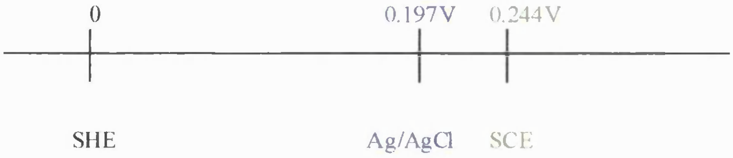

The value obtained for $E_{Ag/AgCl}$ above is for sat. KCl and varies for difference Cl- concentrations in different solution. In most cases Ag/AgCl was measured against SCE in each solution.

3.3.ii UV-Vis cell and instrumentation

The phases (5 ml of each) were mixed and left to settle in glass sample tubes (20 cm^3 with an interfacial surface of approximately 4.5 ml· Each phase was extracted and transferred to a quartz cuvette (l=1.00 cm) that was previously cleaned thoroughly with the respective solvent and sample. The spectrum was scanned over the UV-vis range (900-100 nm) with appropriate reference solution. The instrument was a Shimadzu 2401 PC recording spectrophotometer interfaced with a PC, controlled with the Shimadzu Hyper UV 1.50 software. The wavelength scan rate was 400 nm min^{-1}.

3.3.iii Surface tension cell and instrumentation

The surface tension measurements for surfactant adsorption were carried out with the ring method, using a Dynamic Surface Tensiometer (NIMA Technology, Coventry, England – Type DST 9005 SN 009), which was computer controlled. A beaker of volume 50 ml was used as a cell, into which equal volumes (10ml) of the two phases were carefully transferred. The liquid/liquid interface was left to equilibrate for at least 30 min prior to the measurement covered with Parafilm. The organic phase consisted of the organic electrolyte 0.001 M BTPPATPB and various concentrations of the surfactant sorbitan monostearate SM. The aqueous phase was phosphate buffer, adjusted to pH=7 (0.001 M KH_2PO_4, 0.001 M K_2HPO_4 or LiCl). The two phases therefore did not have a common ion that would establish an interfacial potential difference. The surface of the aqueous phase was sucked away with a water pump to prevent the contamination of the ring while immersing from the top.

The Pt (d= 500 μm) ring used, which was 20.5 mm in diameter, was flamed before use in an oxidative flame and rinsed with H_2O in order to remove any possible contaminants such as grease. It was kept horizontal with less than 1° deviation. The liquid density was assumed to be 1 and the initial surface tension guess of 7.28 mN/m. The immersion speed was 10 mm/min. The ring was immersed ~8 mm, in the organic phase and withdrawn to 6 mm. The immersion depth and the resultant force was controlled by the software which performed a programmed immersion, once the distance from the interface was established.

The surface tension measurements for GOx adsorption at the water/air and water/oil interfaces were carried out using a Kruss K10 digital tensiometer. The ring was cleaned following a similar procedure as described previously. All experiments were thermostated at 25-27°C, using a water bath (HAAKE Fissons, K20). Samples were prepared and left covered with Parafilm over various periods of time periods for adsorption to reach equilibrium

3.3.iv Neutron reflection cells and instrumentation

Neutron reflection measurements were performed on the white beam reflectometer SURF at the Rutherford Appleton Laboratory, ISIS, Didcot, UK, using neutron wavelengths from 0.5 to 6.5 Å. Neutrons in this case are produced by the spallation process. Initially a H^- ion source produces a beam that is accelerated to ground and then is injected into a linear accelerator, that results in a 70 MeV and 200μs long, 22 mA H^- pulse. The proton beam is further accelerated in the synchotron, where upon entry the H^- beam is stripped of its electrons by a 0.3 μm thick alumina foil. The resulting protons make around 10000 revolutions in the synchotron, resulting in a 800 MeV and 100 ns long pulse. The beam is then captured by the RF harmonic system and is transported to the neutron target. This process is repeated 50 times a second, and results in highly energetic protons that bombard a heavy metal target, in this case tantalum, thus triggering an intranuclear cascade, with nuclei reaching a highly excited state.

These nuclei then release this energy by evaporating nucleons-mainly neutrons, that generally have very high energies and are slowed by an array of small hydrogenous moderators around the target, where the moderator temperature determines the spectral distribution. This results in an extremely intense neutron pulse, which is delivered with only modest heat production in the neutron target.

Several instruments utilise this beam in various ways, i.e. diffraction, reflection or excitation. A liquid hydrogen moderator (20 K) is used to provide the beam to the SURF instrument, which was used in the present study. In this instrument the glancing–angle incident beam is used to probe details of the structure perpendicular to the studied surface, via the interference pattern of the resulting scattered beam.

The aqueous buffer solutions with the various enzyme concentrations were poured into Teflon troughs to give a positive meniscus in order to prevent obstruction of the incoming and reflected beam by the teflon, following a procedure described in detail elsewhere[130]. The troughs were mounted on an anti-vibration Table with 5 trough slots, which allowed the continuous monitoring of the reflectivity of the sample until a steady value was obtained. The alignment of each trough was established by adjusting each time the appropriate heights using a laser beam that shared the beam path as the neutron beam. The collimated neutron beam was reflected at the water/air interface at three different glancing angles, 1.5°, 0.8 °, 0.5 ° and the three reflectivity curves were subsequently merged manually to produce a *Q* range necessary to determine the layer thickness, with appropriate scaling factors. The beam intensity was calibrated with respect to clean D_2O. A flat background was determined by extrapolation to high values of momentum transfer *Q*. All the experiments were carried out at 25 °C.

3.3.v Microelectrode cell and instrumentation

The custom-made cell employed for the study of the organic redox species using microelectrode is shown in Figure 3.4, operated in a two-electrode configuration. The volume of the organic phase (o) was 2 ml and of the aqueous reference (wro) phase 1 ml. A Pt microelectrode (r=25 μm), was used as the working electrode and a Ag/AgCl stick as a reference+counter electrode, both fabricated as described in previous sections. The cell is used to study the oxidation of the various ferrocene derivatives x-Fc, with x= - , DiM- , DecaM- .

The organic electrolyte was $BTPPA^+TPB^-$ (0.001 M) and the aqueous electrolyte was $BTPPA^+Cl$ that establishes a potential difference of aqueous with respect to the organic phase of $\Delta\phi_i$=405 mV.

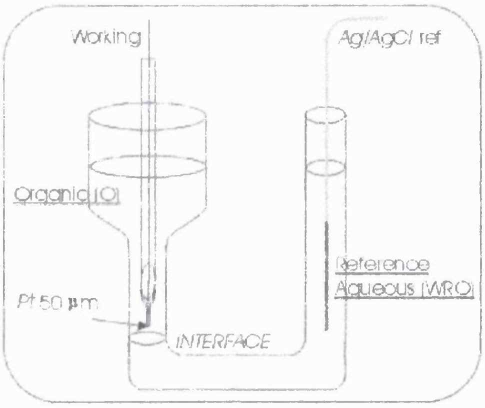

Figure 3. 4 Electrochemical cell for microelectrode measurements with organic redox species

A computer controlled potentiostat (µ-Autolab II, EcoChemie) was used for the microelectrode measurements.

3.3.vi Aqueous cell and instrumentation

The cell employed for the electrochemical study of the aqueous redox species: $Na_4[Fe^{II}(CN)_6]$, the $K_4[Ru^{II}(CN)_6]$ and $Ru^{II}(NH_3)_6Cl_3$ was supplied by BAS. For microelectrode measurements, cyclic or linear voltammetry with a two electrode configuration was used with a Pt microelectrode (r=12.5 and 25 µm) as the working electrode. The half wave potential of the aqueous redox species was measured and the standard potential was estimated. The instrument used was the µ-Autolab in a two-electrode configuration (connecting W+S and C+R leads). A Pt wire was also used vs. a reference electrode, such as SCE, connected to a voltmeter that measured the rest potential E_{Rest} of the aqueous redox species. This was then corrected vs. SHE in order to estimate the equilibrium potential E_{Eq} of the specific ratio used shown in Table 3.4.

3.3.viii Four electrode cells and instrumentation

For the impedance measurements a specific type of four-electrode cell, (Figure 3.5) which provided a planar interface of 28 mm^2 was used. It was custom made in Porto University[138], designed to ensure interface stability throughout the experiment (>4 hours). After filling the cell carefully and establishing the interface, the cell was equilibrated for 30-60 min. All experiments were carried out at room temperature (23±2°C). The reference electrodes were Ag/AgCl sticks electrochemically prepared and used with an aqueous/organic reference junction both connected with capillaries to the interface, while the counter electrodes were platinum mesh. Potential control was maintained with a Solartron-1278 potentiostat and the impedance measurements were monitored using a Solartron-1250 frequency response analyser, both controlled via a GPIB interface with a home-made software (C.M. Pereira). An equivalent circuit was obtained using the "Equivcrt" software (B. Boukamp). Similar impedance experiments were also carried out using the Autolab potentiostat, controlled by the Frequency Response Analyser (FRA) software.

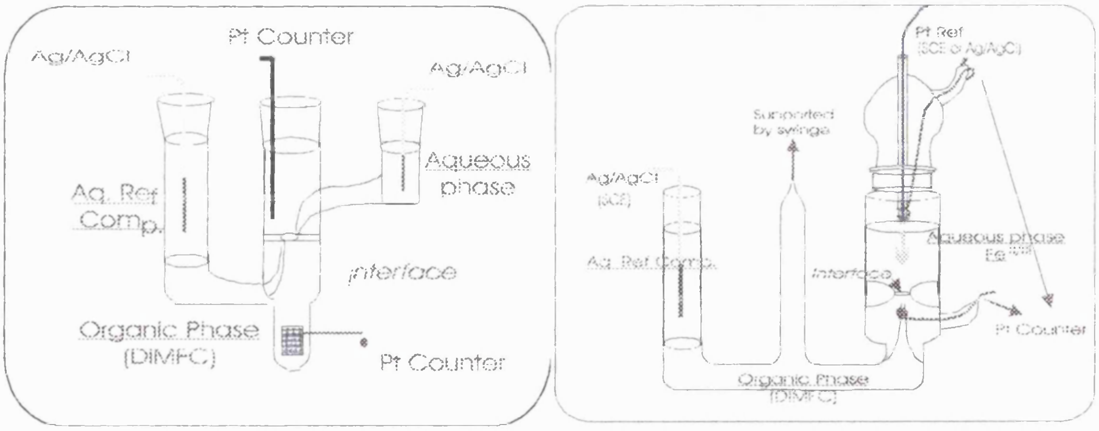

Figure 3. 5 Four electrode cells a. Porto Univeristy Design b. HUT design

Prior to all impedance measurements cyclic voltammograms were obtained, and the following procedure was followed in order to control any possible changes of the electrochemical characteristics of the liquid/liquid interface. The ac-impedance measurements started at a dc-potential in the middle of the window, which was varied then in steps of 50 mV towards the positive and then negative direction.

The chosen range of frequencies was between 10 and 0.1 Hz. with amplitude for the ac-perturbation of 10 mV. Higher frequencies were avoided in order to eliminate high frequency artefacts that would complicate the analysis [139].

Both the two cells depicted in Figure 3.5 were used for the four electrode cyclic voltammetry measurements. Figure 3.5b depicts the cell that was custom made at Helsinki University of Technology[140]. This cell consisted of three different compartments, the aqueous (w), the organic (o), both with capacity of 2 cm^{-3}, and the aqueous reference junction (wro). The polarisable interface between the two phases had an area of 27 mm^3, and was maintained flat by adjusting the syringe, which was also used for filling the cell with the organic phase.

Four-electrode measurements were carried out with a computer controlled potentiostat (Autolab PGStat 100) that implemented positive feedback ohmic compensation: Figure 3.6. The *i*R compensation was adjusted to the maximum achievable before the electronic system oscillated. The potential difference was supplied from the two Pt counter electrodes (in Figure 3.6: CE and WE), situated very close to the interface, which were also used to measure current. The potential difference was measured from the two reference electrodes (in Figure 3.6: RE and S), chosen from the following: Ag/AgCl, SCE or Pt.

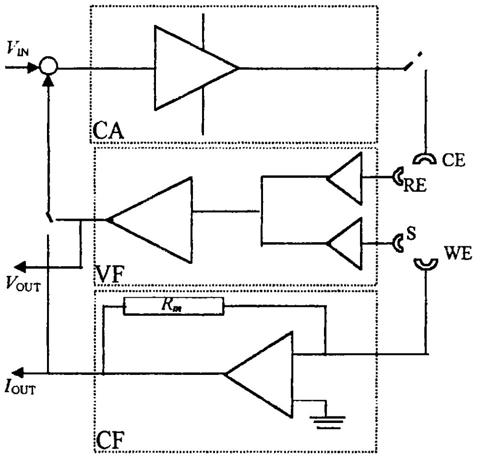

Figure 3.6 Simple schematic of the four-electrode circuit diagram (see text) VF: voltage follower, CF: current follower, CA: current amplifier, R_M: measuring resistance

3.3.viii MEMED cell and instrumentation

The idea of the 'MEMED' experiment, illustrated in Figure 3.7 is that the aqueous/organic interface is moved towards a probe electrode, by extruding a drop of one phase into the other (Figure 3.7). In the present work the organic phase was extruded into the aqueous phase. The Pt ultramicroelectrode (radius=1μm)[141] sealed in glass was operated in a 2-electrode configuration against Ag/AgCl. The ratio of the microelectrode to the insulator radius was RG≈10. A borosilicate glass capillary tip, with an internal diameter of *d*=100um, was immersed and positioned on top of the microelectrode. The probe was positioned with the aid of x-y-z stages. The organic phase was pumped through the capillary tip to produce an expanding drop of a diameter=1mm at contact point. The flow of the organic phase was controlled with a microsyringe infusion pump (CP Instruments), fitted with a 500ul syringe (Hamilton). The drop approached and eventually touched the microelectrode, detached from the tip and was renewed. The flow rates used were 200, 300, 400 μl/h. Video microscopy was used to monitor the set-up of the electrodes and the growth of drops during experiments.

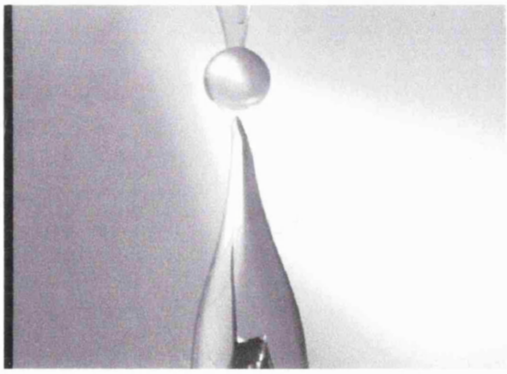

Figure 3. 7 Part of the electrochemical cell used in the MEMED experiments with an expanding drop of the organic phase approaching an ultramicroelectrode immersed in the aqueous phase,

Both phases had a partitioning ion (perchlorate) that established the Galvani potential difference. ET occurred as the two phases came in contact. The depletion or formation of one of the species of either of the aqueous redox species was monitored at the microelectrode. The potential of the microelectrode was kept at a value to ensure diffusion-limited oxidation or reduction of the aqueous species.

3.3.ix SECM cell and instrumentation

For the SECM technique various cells and configurations were tried. The cell used for the enzyme system was an optical cubic cell (10ml), with a three-electrode configuration. The working electrode was a hook microelectrode (Pt, *d*=25μm, RG≈40) that could be immersed into the organic phase and approach the aqueous/organic interface from below. When operating in three electrode mode the counter electrode was a platinum electrode (*d*=50μm). The reference tube was inserted in the cell, where only the organic phase is present along with the two Pt electrodes. The aqueous phase was added on top of the organic where it was degassed for at least 30 min with Ar. The aqueous reference phase was added in the reference tube and a Ag/AgCl stick placed into the tube as a reference electrode. The cell stood on a micropositioner stand that allowed adjustment of the position of the interface with respect to the microelectrode.

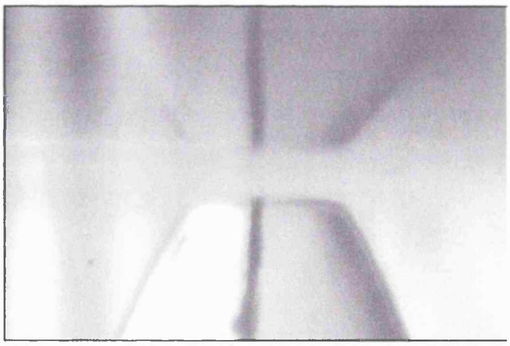

Figure 3. 8 Part of the electrochemical cell used in the SECM experiments with a ultramicroelectrode positioned near the interface, with it's reflection on the other phase.

The interface was ensured to be flat, the hook microelectrode brought near the interface (*d*<250μm, see figure 3.8), and then the electrode was stepped continuously at rates between 1 μm s^{-1} and 4.6 μm s^{-1}, until it touched the interface. The "hook" electrode was controlled by a step driver that could move it with a maximum speed of 4.6 μm/sec, 1μm/step. The position of the microelectrode with respect to the interface was controlled with video microscopy (Figure 3.8).

When a single electrolyte was used, the two phases were pre-equilibrated and left to settle for at least 30 min prior to the final set-up, in order for the single electrolyte to partition and establish the Galvani potential difference needed. Cyclic voltammetry in the organic phase was used every time prior to SECM, in order to check that the set-up was working correctly. For SECM, transient chronoamperometry was used at a diffusion controlled potential. Current was monitored against time, until the electrode touched the interface. This transient was then transformed to a normalised current-distance approach curve. The potential control was established by the μ-Autolab potentiostat.

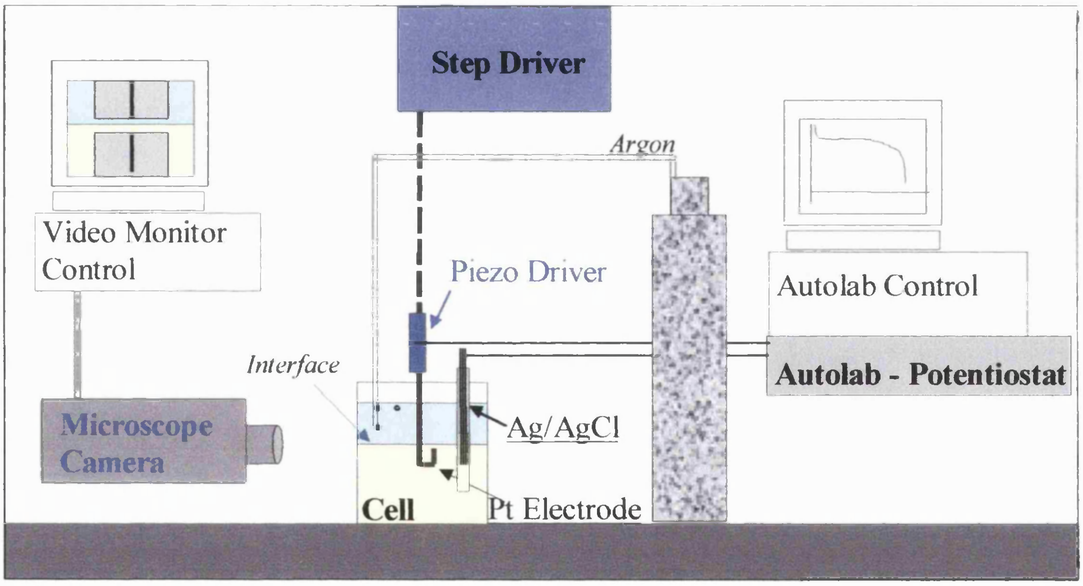

Figure 3. 9 The SECM set-up that consists of the video microsopy set-up, the step driver that drives the "hook" microelectrode, the degassing set-up and the current monitoring equipment.

The home-made SECM set-up shown in Figure 3.9 was initially tested by stepping the electrode to a known insulator such as air, while measuring the response at the "hook" microelectrode. Figure 3.10 shows a typical transient for an approach to the organic/air interface.

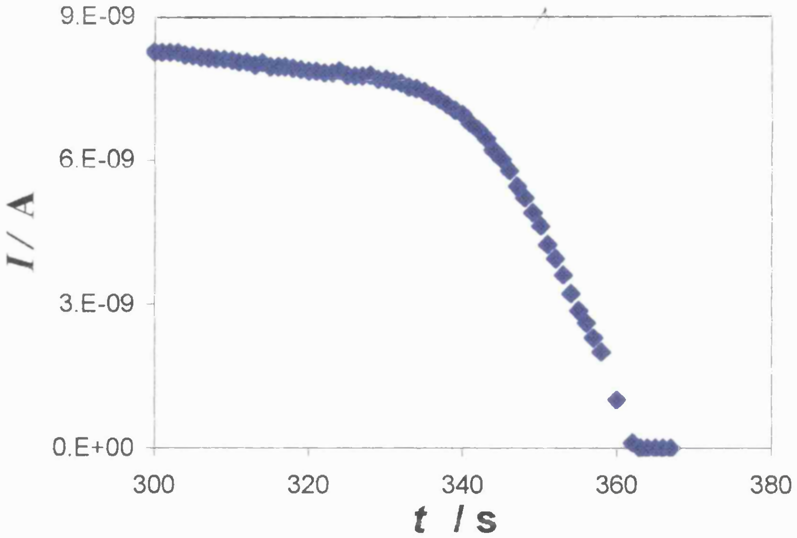

Figure 3.10 Chronoamperometric measurement as microelectrode approaches the air/DCE interface. The electrode was held at 0.5 V vs Ag/AgCl (wro), where the current is diffusion controlled for the oxidation of 1mM DiMFc in the organic phase with 0.01 M TEAClO$_4$ present and a reference junction of 10m M TEACl , 0.01 M LiCl / Ag/AgCl. Speed 4.6 µm/sec.

When the electrode was far away from the interface the current response was as expected for diffusion controlled oxidation of DiMFc to DiMFc$^+$. As the electrode approached the interface the DiMFc species were depleted within the gap between the electrode and the insulator (air) and therefore the current decreased, dropping to zero as the electrode penetrated the oil-air interface. This initially was taken as distance d=0, but it was realised that non-ideal experimental set-ups (tip position not normal to interface, RG=40), as well as electrostatic forces between tip and aqueous phase had to be taken into consideration. The distance was then estimated by comparing the measured curve with a theoretical approach curve calculated for an insulating substrate.

Figure 3.11 shows the resulting approach curve for normalised values (current I measured at time t divided by current I_0 measured at ~250 µm from interface vs. distance d divided by the electrode radius a).

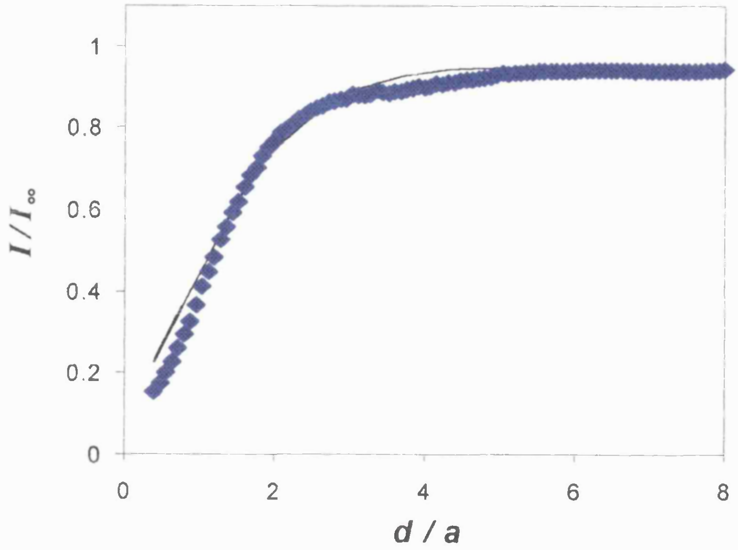

Figure 3.11 Normalised approach curve as derived from the transient shown in Figure 3.10. Distance *d*, normalised to electrode radius, *a*, current, *I*, normalised to current I_{∞}. (Diamonds): experimental data, (solid line):theoretical fit for an insulator's response

Figure 3.11 shows a good correlation of the experimental values with the expected simulated response for the negative feedback observed for an approach to an insulator. The system was optimised over some time, using better electrode RG, current collection rates, approach speed etc. A set-up of different cells and electrodes (RG=10) as shown in Figure 3.12, were used for monitoring interfacial ET and the effect of surfactant on it. Some of these experiments were carried out at Warwick University, where a different SECM equipment was used, described in more detail elsewhere[142].

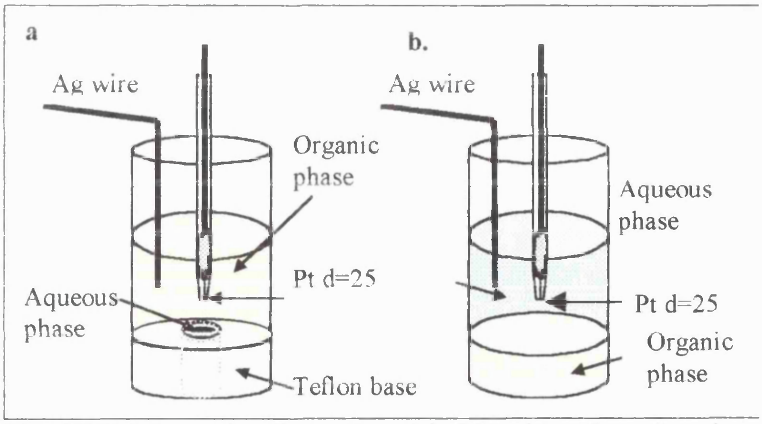

Figure 3. 12 The SECM electrochemical cell used in Warwick, where the microelectrode was immersed (a.) in the organic phase approaching a flat aqueous phase beneath held below the organic phase due to electrocapillary phenomena, and (b.) immersed in the aqueous phase approaching a concave organic phase at the middle of the interface.
The reference electrode was a Ag wire immersed in the respective phase.

The electrode in this case was controlled by a piezo-motor that followed a programmed approach with a speed of 0.6 μm s^{-1}. In cell 3.12.a the aqueous phase was held under the organic under capillary forces, whereas cell 3.12.b was used for studies where the electrode was immersed in the aqueous phase and approached the organic phase.

Chapter 4: Surfactant adsorption at a liquid/liquid interface

4.1 Introduction

The measurement of double layer capacitance, C_D, has already been used for studying the adsorption of molecules such as phospholipids[143,144] at the polarised liquid/liquid interface. Wandlowski *et al.* showed the Frumkin type adsorption isotherms obtained with various phospholipids[145], while Kakiuchi *et al.*[146] studied the Langmuirian adsorption of non-ionic surfactants at the water-nitrobenzene interface. It was observed that the surfactants lowered the C_D in the range of applied potential with no sign of ion transfer facilitation but of suppression of the convective motion near the interface[146]. The adsorption of sorbitan surfactants at the liquid/liquid interface (water/hexane) has also been studied with the surface tension method[128].

The adsorption of a similar organic soluble non-ionic surfactant, sorbitan monostearate, SM, at the H_2O/1,2-dichloroethane interface is presented in this chapter. The effect of specific adsorption of the base electrolyte ions at the interface is considered negligible, and not studied further. Adsorption isotherms obtained from analysis of impedance and interfacial tension measurements are compared.

4.2 Impedance measurements with various base electrolytes

Impedance measurements were carried out in the absence of any electroactive species and adsorbents. The procedure presented in this section was repeated for all impedance measurements. Three different cells were studied with the impedance technique: Table 4.1.

Table 4.1: Cells studied with impedance technique

Cell 1a	*Ag/AgCl*	**(wro)** 0.01 M LiCl 0.001 M BTPPA$^+$Cl$^-$	**(o)** *Pt* 0.001 M BTPPATPB	**(w)** *Pt* 0.1 M KH_2PO_4 0.1 M K_2HPO_4	*Ag/AgCl*
Cell 1b	*Ag/AgCl*	**(wro)** 0.01 M LiCl 0.001 M BTPPA$^+$Cl$^-$	**(o)** *Pt* 0.001 M BTPPATPB	**(w)** *Pt* 0.01 M LiCl	*Ag/AgCl*
Cell 1c	*Ag/AgCl*	**(wro)** 0.01 M TBuACl	**(o)** *Pt* 0.01 TBuATPB	**(w)** *Pt* 0.1 M KH_2PO_4 0.1 M K_2HPO_4	*Ag/AgCl*

Typical cyclic voltammograms with the potential windows established by the various cells of Table 1 are shown in Figure 4.1:

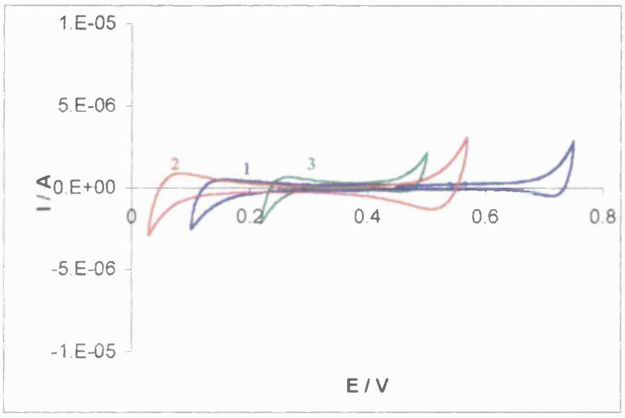

Figure 4. 1 Cyclic voltammograms showing the base potential window for various cells: (blue line 1): cell 1a, (red line 2): cell 1b, (green line 3): cell 1c, υ=25 mVs^{-1}, *A*= 28 mm^2.

Figure 4.1 shows the effect of different ionic compositions on the potential window edges. This was due to the reversible ion transfer of electrolytes from one phase to the other, as the aqueous phase became more positive or negative with respect to the organic phase. Within each defined potential window, no charge transfer across the interface was observed, and the impedance measurements should reflect the effect of adsorption. With BTPPATPB as the organic electrolyte, and phosphate as the aqueous buffer a very wide potential window is established, cell 1a.

For each dc- potential applied, following the *ac* perturbation superimposed, the resulting complex plane diagrams (imaginary *Z*" vs. real *Z'* impedance) was obtained. The complex plane diagrams for a range of potentials obtained with cell 1a, are shown in Figure 4.2. The change of impedance was followed, starting measurements from the middle of the potential window, stepping towards the positive end, then towards the negative end finally reaching the initial potential value. This procedure also gave an indication of the dynamic state of the adsorption process, since at equilibrium the initial and final values should superimpose.

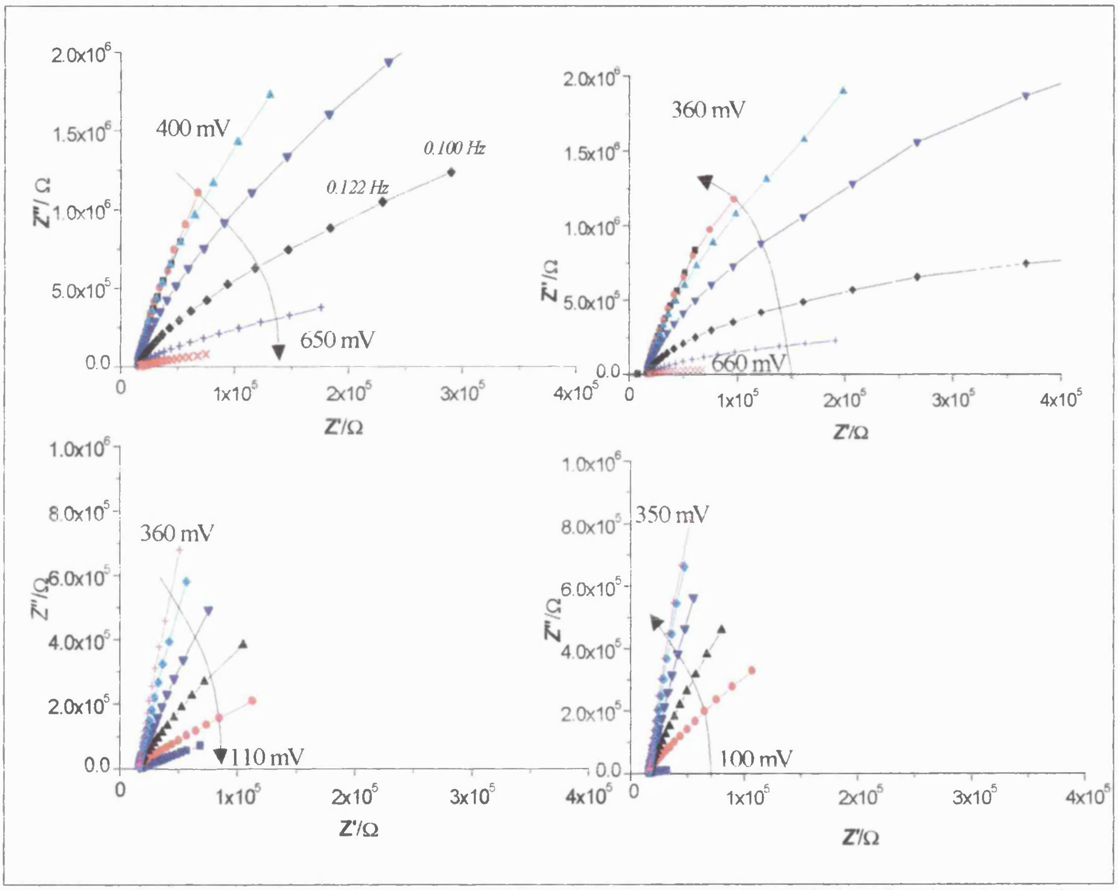

Figure 4. 2 Complex plane diagrams of Z''-Z' for various dc-E applied, following the cyclic voltammogram of cell 1a, Fig. 4.3,with 50 mV steps, f=0.1-10 Hz. Solid lines are drawn as a guide.

The resulting impedance values superimposed for similar potentials, provided that the interface remained stable over the period of the measurements (3 hours). This was usually the case, unless the interface was not flat in the end, as the larger volume of the aqueous phase would result in a concave curvature.

At the middle of the potential window, the response of the system acted as an equivalent circuit of resistance and capacitance in series, as shown in the inset of

Figure 4.3. This response was due to the electrolyte solution resistance, R_s, and the electrical double layer capacitance C_D. As the applied dc- potential values moved towards the edges of the potential window, the impedance response included a polarisation resistance, R_{CT}, due to the onset of ion transfer of the base electrolyte, which is parallel to the double layer capacitance.

The response for the totality of frequencies employed was simulated to fit this equivalent circuit, to give a capacitance values for each potential. Figure 4.3 shows the capacitance values based on the fits obtained for the three base potential windows of Figure 4.1:

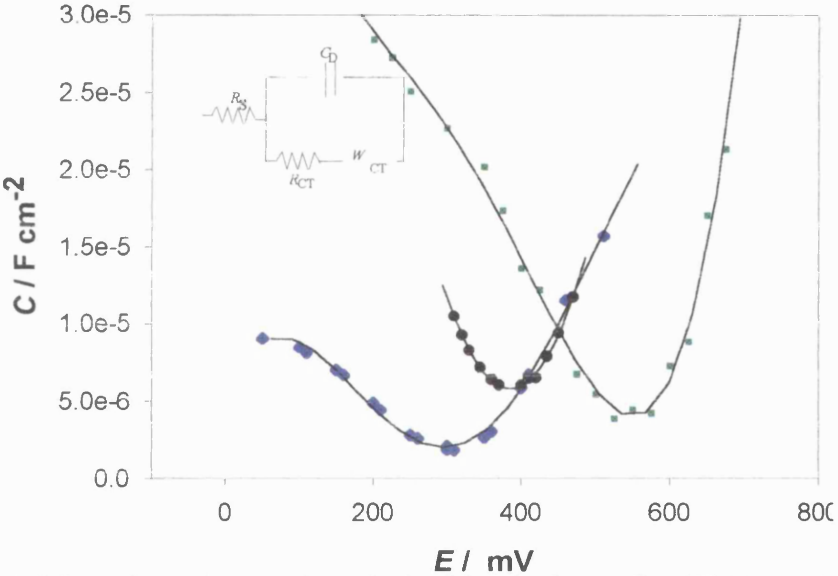

Figure 4. 3 Sets of capacitance values obtained for the three cells of Table 4.1 from fitting the equivalent circuit, shown in the inset. (squares): cell 1a, (diamonds): cell 1 b and (circles): cell 1c. Solid lines are fourth order polynomial fits.

Figure 4.3 shows that the cells exhibited good stability and the impedance measurements resulted in reproducible capacitance values, which fully characterised the interface in the absence of adsorbents. The solution resistance was also stable within the potential range, and was found to be dependent on ionic strength. R_s was ≈ 4500 Ohms for the cell of high concentration base electrolytes (cell 1c) and 15000-20000 Ohms for the cells of low concentration of base electrolytes (cell 1a-b).

4.3 Impedance study of SM adsorption

4.3.i Facilitated IT in the presence of SM

With cell 1a, the presence of surfactant, SM, resulted in a narrowing of the potential window with increasing surfactant concentration (Figure 4.4):

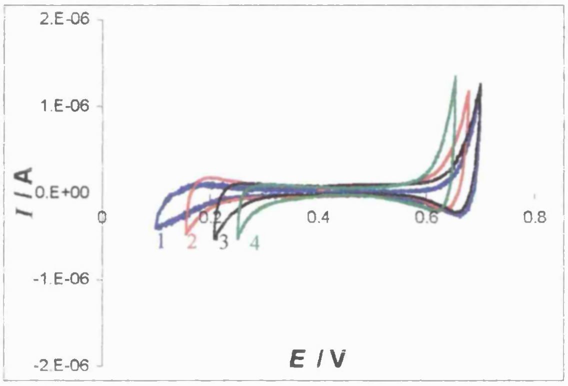

Figure 4. 4 IT induced by increasing SM concentration in cell 1a, υ=25 mVs^{-1}, A= 28 mm^2 (blue line 1): 0.1 mM, (red line 2): 0.5 mM, (black line 3):1 mM and (green line 4): 5 mM SM.

With increasing SM concentration the negative edge of the window was shifted to more positive potentials. As the aqueous phase became more negative with respect to the organic phase, either aqueous anions transferred into the organic phase or organic cations into the aqueous phase. Therefore it appears that the presence of surfactant SM resulted in a facilitated ion transfer. Since the surfactant is insoluble in water the most likely hypothesis is the facilitated transfer of aqueous phosphate anions into the organic phase. The impedance was measured within the available potential window. The fitting of the impedance values resulted in the capacitance-potential curves shown in Figure 4.5:

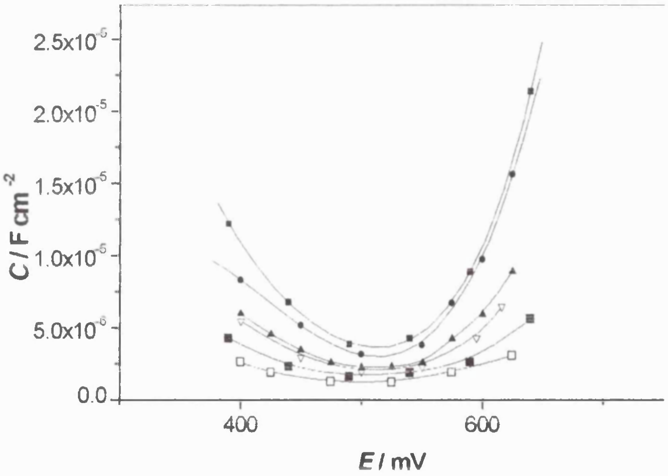

Figure 4. 5 Set of capacitance curves derived from fitting impedance measurements on cell 1a to the equivalent circuit of Figure 4.5. From top to bottom: 0, 0.05 , 0.1, 0.5, 1 and 5 mM SM.

It is shown that with the restriction of the available potential windows, the comparison of capacitance curves in the absence and presence of surfactant is limited within a small potential range. Nevertheless, the potential of zero charge for all the curves can be observed within this range and a slight displacement to more positive potentials with increasing surfactant concentration is observed. The effect of increasing surfactant concentration on the double layer capacitance at the potential of zero charge is given in Figure 4.11. Although the process of ion transfer can be separated and accounted for with the impedance measurements, the presence of the extra charge transfer might interfere with the film of adsorbed surfactant at the interface.

4.3.ii Measurements in the absence of facilitated IT

Using cell 1b, the presence of surfactant, SM, in the organic phase did not affect the edges of the potential window, as shown in Figure 4.6, with no external IR compensation used:

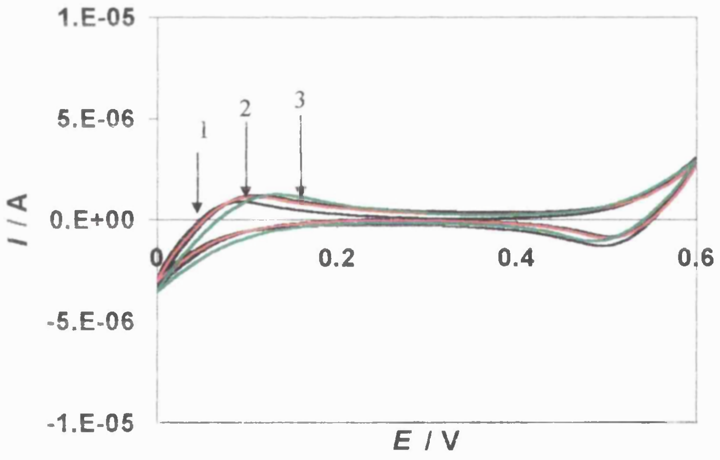

Figure 4. 6 Cyclic voltammograms showing the effect on the base potential window (black line 1) of 0.001 M: (red line 2)and 0.005 M: (green line 3)using cell 1b. , υ=25 mVs^{-1}, A= 28 mm^2.

The impedance diagram for each potential was again measured and each impedance diagram in the presence of the surfactant as shown in Figure 4.7 was fitted to the equivalent circuit shown in the inset:

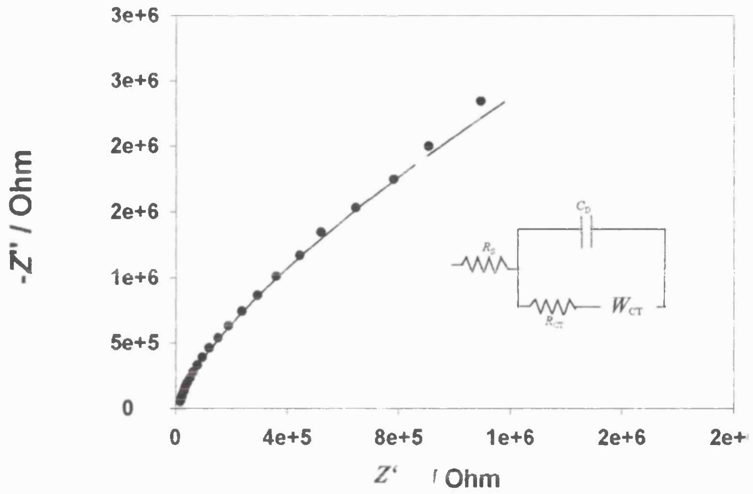

Figure 4. 7 Complex plane impedance plot for cell 1b at E=350 mV, with 0.0007 M surfactant present. Points: experimental values, line: fit of the equivalent circuit in the inset with R_s the solution resistance, C_D the double layer capacitance, W_{CT} is the diffusion (Warburg) impedance and R_{CT} the charge transfer resistance of the base electrolyte ion transfer processes.

All curves converged to one value at the *Z'* axis (high frequencies), which was the solution resistance $R_{s,\mathrm{Cell\ 1b}}$ =15000 Ohms. It was unnecessary to include in the equivalent circuit the extra adsorption impedance Z_{ads}, previously proposed for the adsorption of phospholipids[145]. The fitting errors for the equivalent circuit of the inset in Figure 4.7 were less than 2%. Figure 4.8 shows the derived capacitance values as a function of interfacial potential difference and surfactant concentration:

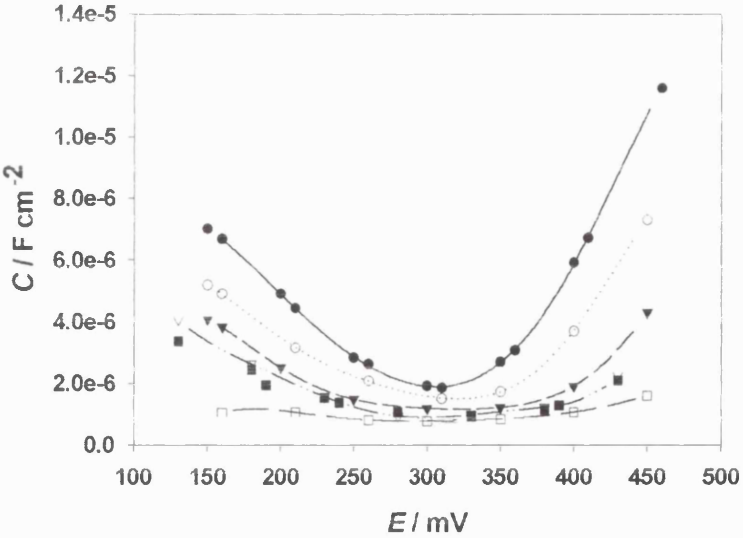

Figure 4. 8 Set of capacitance curves obtained from data as in Figure 4.7 with increasing sorbitan monostearate concentrations using cell 1b. From top to bottom 0, 0.2, 0.5, 0.7, 2 and 5 mM.

Figure 4.8 also exhibits a slight displacement of the potential of zero charge, *E*pzc (at each curve minimum), from *E*=310 mV in the absence of surfactant to *E*=340 mV in the presence of surfactant. Every SM concentration studied lowered C_D, showing significant adsorption, especially in the region negative of the pzc, where it was evident that the surfactant exhibits higher surface activity. The effect of the potential was much greater than that exhibited for similar surfactants at the nitrobenzene-water interface, studied by Kakiuchi and others[146]: a larger potential range was studied here. At high enough surfactant concentration, c=5mM, a potential-independent capacitance was obtained, consistent with complete surface coverage by surfactant, with the formation of a monolayer at the interface. The effect of increasing surfactant concentration on the double layer capacitance at the potential of zero charge is also given in Figure 4.11 for comparison.

4.4 Surface tension due to SM adsorption at a liquid/liquid interface

A plot of surface tension, γ, against ln(c) is given in Figure 4.9 with measurements carried out with cell 1b. Firstly, an indication of the critical micelle concentration was extracted from the break of the curve in γ-ln(c): c_{CMC} ≈10 mM.

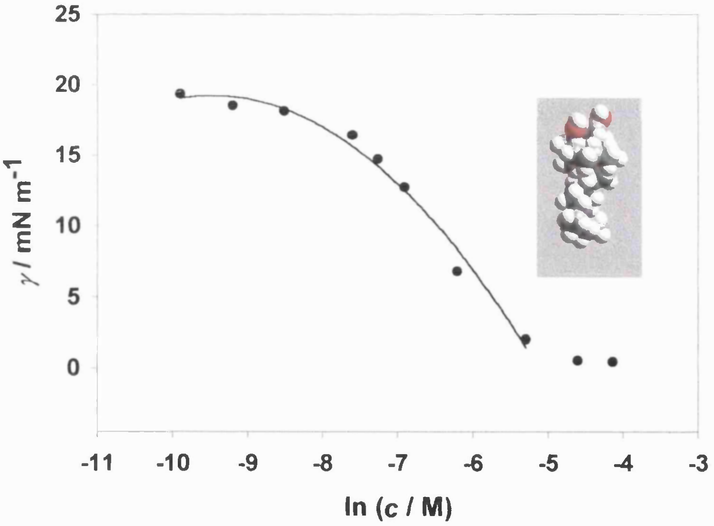

Figure 4. 9 Surface tension measurements with cell 1b after 1h. of equilibration for the adsorption of the surfactant SM at the liquid/liquid interface.

From the tangent of the quadratic fit shown in Figure 4.9 the surface excess, Γ_i, was calculated using the Gibbs relation, equation (2.15). Using the surface excess value calculated just below CMC the resulting area/molecule $A=1/\Gamma N_A$ was estimated to be A=47Å^2, which was in good agreement with reported values of the same surfactant at the water/hexane interface.[128] A space filling molecular model, calculated using Cerius2 software provided a picture of the surfactant that was slightly tangled in an ellipsoid of 15Å length and 4-8 Å wide. The model is shown as an inset in Figure 4.9. Assuming that the "protruding" polar part was a circle of radius 4 Å, the resulting approximate area was 50 Å^2. The coincidence of this value with the result of surface tension measurements indicates that the surfactant was adsorbed normal to the interface. If the molecule were lying flat on the surface it would have an area/molecule: 280 Å^2.

The effect of increasing surfactant concentration on the surface excess Γ is shown in Figure 4.10. From the surface excess at a fully covered interface, Γ_{max}, an adsorption isotherm can be obtained with the surface coverage estimated from $\theta=\Gamma_i/\Gamma_{max}$. The adsorption isotherm is superimposed in Figure 4.10.

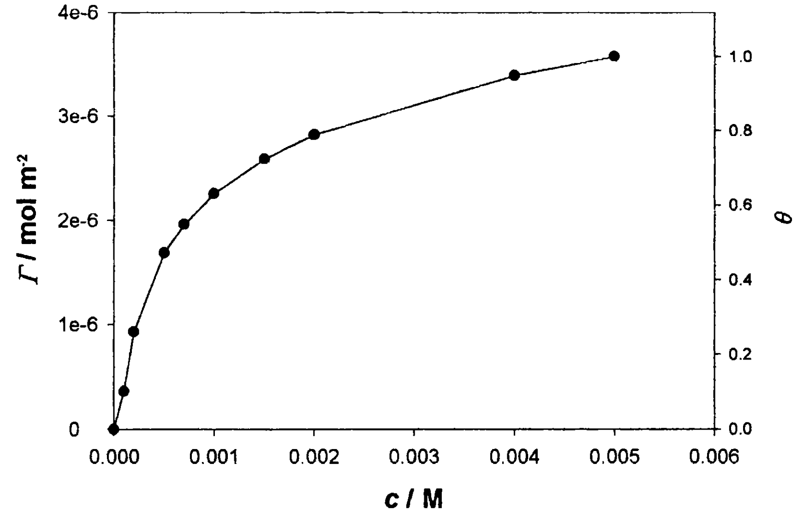

Figure 4. 10 Effect of SM concentrations on the surface excess Γ at the liquid/liquid interface calculated from Figure 4.9 and the resulting adsorption isotherm θ-c (see text)

4.5 Discussion on the effect of surfactant on C_D and γ

The comparison of voltammograms in Figures 4.4 and 4.6 strengthens the hypothesis made earlier for cell 1a, that the surfactant SM causes the IT facilitation of aqueous anions in the organic phase. When the phosphate buffer is replaced by LiCl in cell 1b, the negative edge of the potential window did not shift to more positive potentials with increasing surfactant concentration. Figure 4.11 shows the effect of the adsorption of the non-ionic surfactant on the capacitance values at the potential of zero charge, pzc, using both cells 1a and 1b:

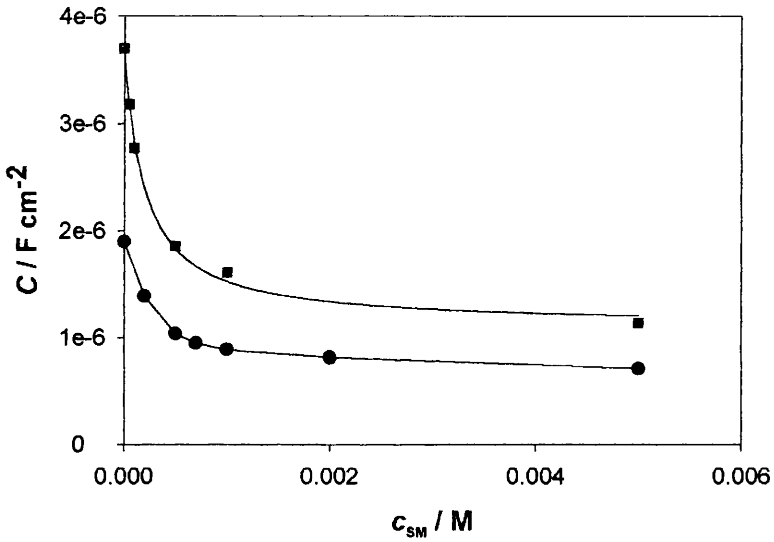

Figure 4. 11 Effect of increasing surfactant concentration on capacitance C_D at pzc, using cell 1a (squares) and cell 1b (circles)

Figure 4.11 establishes the effect of using different aqueous electrolytes on the double layer capacitance in the presence and absence of surfactant. The effect of different electrolytes on C_D in the absence of surfactant was thoroughly studied by Pereira *et al.*[147] where it was suggested that for lower electrolyte concentrations, the observed capacitance decreased. The magnitude of the effects was shown to be dependent on the concentration of either electrolyte. They concluded that the *C(E)* curves for liquid/liquid interface depend on both the ions and counterions on each side of the interface.

The effect of surfactant on C_D was treated by a simple model proposed by Kakiuchi[146], where the surfactant forms dense patches on the surface. In this case, the double layer capacitance can be approximated as a parallel combination of the double layer capacitance of the uncovered surface (potential dependent) with that of the surfactant covered patches (potential independent):

$$C_D = C_D^{\theta=1}\theta + (1-\theta)C_D^{\theta=0} \qquad \textbf{(4.6)}$$

with $C_D^{\theta=1}$ the capacitance value at maximum coverage, ~5 mM,

$C_D^{\theta=0}$ the capacitance value in the absence of surfactant and

θ the fractional coverage of the surface by surfactant patches.

The model applies if the electrical potential is uniform over the surface (i.e. the SM patches are at least large enough that there are no discreteness-of-charge effects), and the surface coverage does not vary with perturbation of the interfacial potential difference used for the measurement. From (4.6):

$$\theta = \frac{C_D - C_D^{\theta=0}}{C_D^{\theta=1} - C_D^{\theta=0}} \qquad \textbf{(4.7)}$$

The surface coverage, θ, calculated this way was found to be independent of potential with respect to the potential at zero charge, E-E_{pzc} within the potential range studied. The surface coverage θ obtained for both cells 1a and 1b was very similar as shown in Figure 4.12, indicating that the adsorption process of the surfactant was independent of the base electrolytes present.

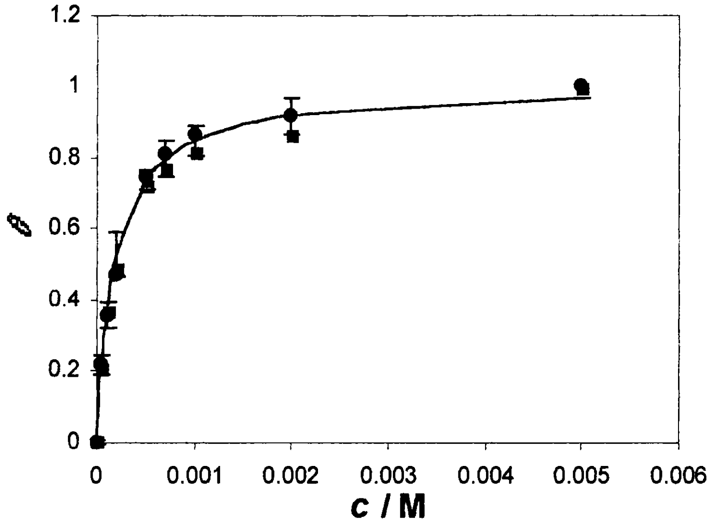

Figure 4. 12 Adsorption isotherm obtained from figure 4.11 using cell 1a (squares) and cell 1b (circles), error bars are the standard deviation from three measurements using cell 1a, and (solid line): Langmuir fit.

The surfactant layer could be modelled in both cases as a simple dielectric of thickness, χ, with relative permittivity ε taken for hydrocarbons as 2. From the capacitance value at full coverage the resulting layer thickness was calculated: $\chi \approx \frac{\varepsilon\varepsilon_0 A}{C_D^{\theta=1}} = 16\,\text{Å}$. This value correlates very well with the estimated length d=15 Å of the molecular model of the surfactant shown in the inset of Figure 4.9.

As a first approximation the applicability of the Langmuir isotherm was considered for the adsorption of the non-ionic surfactant, following the equation:

$$\frac{1}{\theta} = \frac{1}{Kc} + 1 \qquad \textbf{(4.8)}$$

with θ the fractional surface coverage, c the bulk concentration and K the equilibrium constant for adsorption

Plotting $1/\theta$ with $1/c$, as shown in Figure 4.13 using the surface coverage obtained from both cells 1a and 1b, results in a value of the equilibrium constant of K_L=(5.50±0.05) x 10^3 M^{-1}

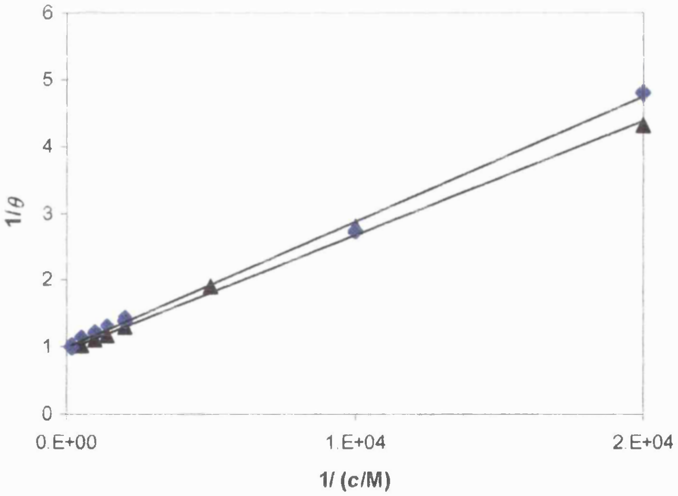

Figure 4. 13 Langmuirian treatment of the surface coverage values for SM adsorption obtained with capacitance measurements using cell 1a : (diamonds), cell 1b:(circles): and Langmuir fits (solid lines).

The Langmuir isotherm fitted indicates a negligible lateral interaction between the adsorbed molecules. Nevertheless a Frumkin isotherm treatment was also attempted for consistency with the surfactant patch model:

$$Kc = \frac{\theta}{1-\theta}\exp(-2a\theta) \quad \text{or} \quad \ln K + \ln c = \ln(\frac{\theta}{1-\theta}) - 2a\theta \qquad \textbf{(4.9)}$$

where a is the interaction parameter.

A plot of $\ln(\frac{\theta}{c(1-\theta)})$ vs. θ, is shown in Figure 4.14:

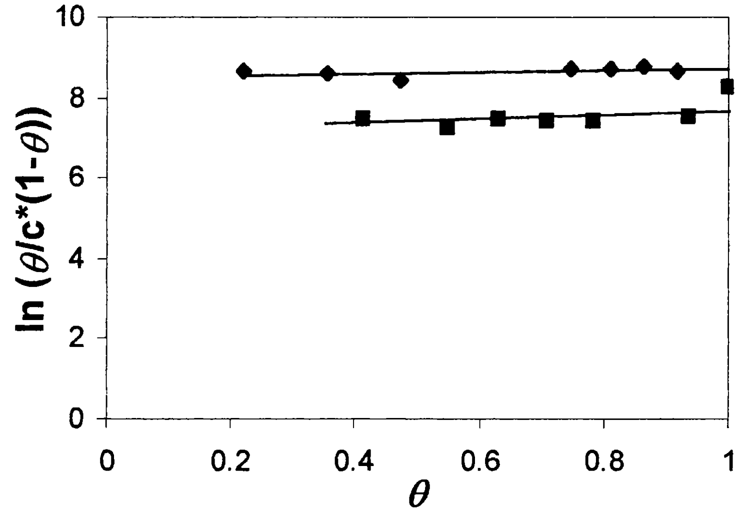

Figure 4. 14 Frumkin treatment for coverage values for SM adsorption at the interface with cell 1b, (diamonds): capacitance data, (squares): surface tension data and (lines): Frumkin fit.

which gives K_F= (5.00± 0.06)x 10^3 M^{-1}, which results in the apparent standard free adsorption energy of ΔG^{θ}_{ads}= -RTln(K_F) = -21 kJ mol^{-1}. This value is comparable with the energy values given for the adsorption of similar surfactants at the water/nitrobenzene interface (ΔG^{θ}_{ads}= -18.6 kJ mol^{-1}) yet smaller for those obtained for phospholipids (ΔG^{θ}_{ads}= -37 kJ mol^{-1})[146]. The positive yet small value of the lateral interaction parameter a=0.19, indicates a very weak attractive interaction between the adsorbed molecules. Both isotherms fit the capacitance measurement and seemed to be in broad agreement. Due to the small value of the lateral interaction parameter it was assumed that the adsorption of the SM at the 1,2-dichloroethane follows a Langmuirian behaviour.

In a similar way, as described for the capacitance results, various isotherms were applied to fit the results obtained from surface tension measurements. As a first approximation, the applicability of the Langmuir isotherm was considered for the adsorption of the non-ionic surfactant. Plotting $1/\theta$ with $1/c$ resulted in a straight line, suggesting a negligible lateral interaction between the adsorbed molecules, with a value of the equilibrium constant of K_L=(2.2 ±0.01)x10^3 M^{-1}. The Frumkin isotherm fitted better the values of high surfactant concentrations as shown in Figure 4.14. A plot of $\ln(c(1-\theta)/\theta)$ vs. θ, resulted in a straight line with K_F=(2.6±0.02) x10^3 M^{-1} and a≈1. The results of the fittings between the two different techniques here are found to be in good agreement.

The adsorption isotherms, $\theta - c$, derived from the capacitance and surface tension measurements will be further discussed in Chapter 9 in comparison with the isotherm derived from SECM measurements presented in Chapter 6.

4.6 Conclusions

- Cells of various ionic compositions were studied with the impedance method. Fitting the resulting complex diagrams to an equivalent circuit provided capacitance curves for different base electrolytes.
- When the surfactant SM adsorbs at the liquid/liquid interface, it forms patches and lowers the double layer capacitance within the potential range studied.
- From the effect on the capacitance at the potential of zero charge both Langmuir and Frumkin isotherm were fitted.
- The presence of SM can induce facilitated ion transfer, which restricts the available potential window when phosphate buffer was present.
- The presence of SM lowered the surface tension of the liquid/liquid interface, and from the effect on the surface excess the adsorption isotherm obtained could be fitted both to Langmuir and Frumkin adsorption models.
- The area per molecule estimated from surface tension measurements, and the layer thickness obtained from capacitance measurements correlated well with estimated values based on an energy minimised molecular model, with the surfactant chain oriented normal to the surface.

Chapter 5: Study of interfacial electron transfer

5.1 Introduction

In this Chapter, interfacial electron transfer (ET) across interfaces that are either polarisable or non-polarisable are presented. Surprisingly, some obvious assumptions have created some confusion in the literature, regarding the equality of potentials across the interface measured with a four-electrode system and potentials measured at a microelectrode[148,149]. A simple analysis and explanation is presented here. Interestingly as well, interfacial ET with dimethylferrocene, widely studied with four-electrode voltammetry has not been studied with SECM, whereas decamethylferrocene, used widely in SECM studies, has never been properly cited for ET with four-electrode voltammetry[150]. Interfacial electron transfer with these systems is presented in this chapter and the limitations of each method are discussed.

5.2 Microelectrode measurements

5.2.i Aqueous redox species

Various aqueous redox species were considered throughout the present study. Their redox behaviour was initially established with linear sweep voltammetry using a two electrode configuration with a Pt microelectrode as a working electrode vs a Ag/AgCl reference electrode:

Cell 2a:	*Pt*	(w) Redox species Aqueous Electrolyte	*Ref*

Three aqueous redox species were explored, hexacyanoferrate $Fe^{III/II}(CN)_6^{3-/4-}$, hexacyanoruthenate $Ru^{III/II}(CN)_6^{3-/4-}$, and hexaamineruthenate $Ru^{II/III}(NH_3)_6^{2+/3+}$. The iron-citrate complex was briefly explored, but was not considered further as its behaviour was not reversible. The results for the other three species are shown in Figure 5.1:

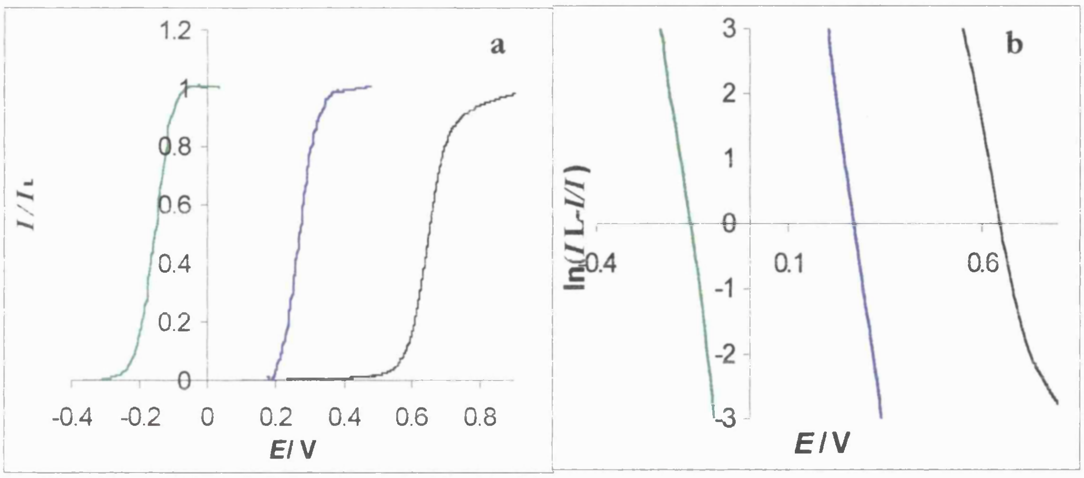

Figure 5. 1 a.Normalised cyclic voltammogram of 1mM $K_4Ru(CN)_6$ (1, black line), $K_4Fe(CN)_6$ (2, blue line), $Ru(NH_3)_6Cl_2$ (3, green line) at a 25 μm Pt microelectrode in 0.1 M NaCl, using cell III vs Ag/AgCl. υ= 10 mV/s. b: Semilogarithmic analysis

From each voltammogram, the limiting current, I_L, was obtained and from equation (2.1) the diffusion coefficient D was calculated, and is presented in Table 5.1. Semilogarithmic analysis based on equation 2.2 is also shown in Figure 5.1.b, from which the half wave potential of each redox species was derived. Table 5.1 shows the half wave potentials, $E_{½}$ and estimated standard potentials, E^0, using $E_{Ag/AgCl}$=0.220 V vs standard hydrogen electrode, SHE, in 0.1 NaCl:

Table 5.1 Half wave potential $E_{2,½}$, standard potential E^0 and diffusion coefficient D values for the aqueous redox species, cell 2

Species	$E_{2,½}$ /V vs Ag/AgCl	E^0/V vs SHE	E^0/V vs SHE*	D x10^6/ cm^{2}s^{-1}	*Slope nF/RT*
$Ru^{III/II}(CN)_6^{3-/4-}$,	0.650	0.870	0.858	9.3	44
$Fe^{III/II}(CN)_6^{3-/4-}$	0.270	0.490	0.460	5.5	41
$Ru^{II/III}(NH)_3^{2+/3}$	-0.220	0.065	-0.080 (HCl)	1.3	30

*Literature values from *Handbook of Chemistry*, CRC Press, 57th edition

Hexacyanoferrate $Fe^{II/III}(CN)_6$ exhibited the most reversible and consistent behaviour and was preferred for the majority of the later experiments.

5.2.ii Organic redox species

The oxidation of various organic species at a Pt microelectrode was studied using a two-electrode configuration, as described in the experimental section. Due to the lack of reference electrodes that can be directly used in the organic phase to give a stable reference potential, a reference junction is employed for the organic phase in cell 3a:

Cell 3a:	*Ag/AgCl*	(wro) 0.01 M LiCl 0.001 M BTPPACl	(o) x M x-Fc 0.001 M BTPPATPB	***Pt*** ***(d=25μm)***

With x= - , DiM- , DcM-, for the different ferrocene derivatives, and BTPPA TPB the organic electrolyte. Cyclic voltammetry was used for the characterisation of the oxidation process for the three organic species. The cyclic voltammograms obtained with cell III, are shown in Figure 5.2:

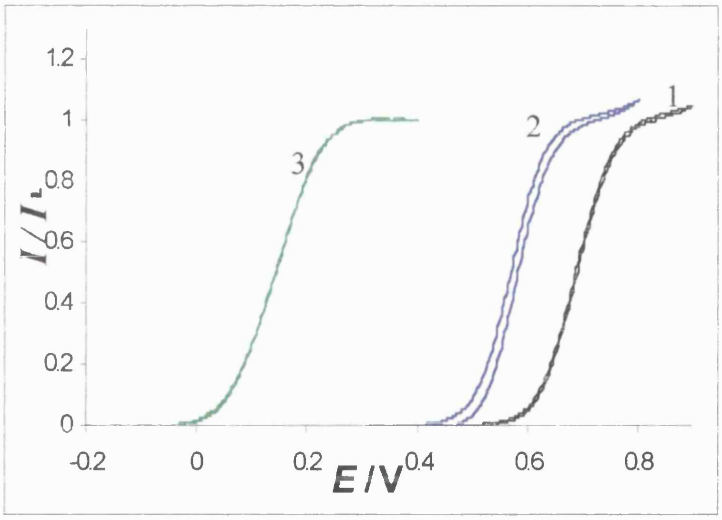

Figure 5. 2 Normalised cyclic voltammograms for the oxidation of 0.9 mM Fc(1, black line), 0.25 DiMFc(2, blue line)and 1mM DcMFc (3, green line) at a 25 μm Pt microelectrode in 1,2-DCE, using cell 3. υ=10 mV/s.

The limiting current value, I_L, from each voltammogram gives the diffusion coefficient D from equation (2.1), presented in Table 5.2. From the semilogarithmic analysis implied by equation (2.2) Figure 5.3 was obtained:

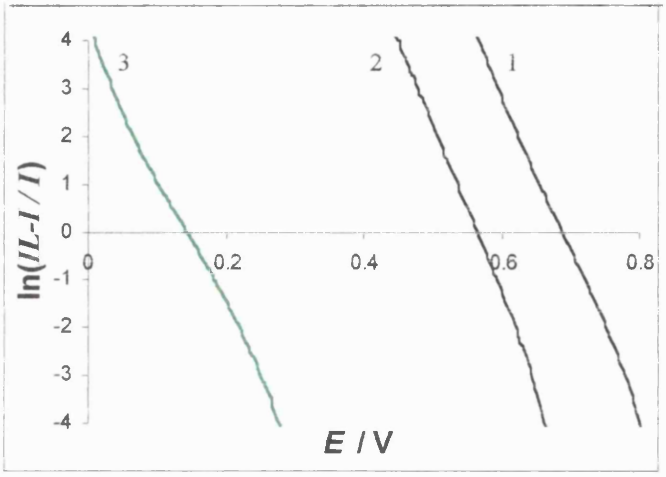

Figure 5. 3 Semilogarithmic analysis based on the data shown in Figure 5.2

The half wave potential for the oxidation of the ferrocene derivatives at the Pt electrode was obtained, $E_{3,½}$ vs. the reference junction of Cell 3. The standard potential of each organic species vs SHE was calculated from:

$$E^0 = E_{3,½} + E_{Ag/AgCl} + \Delta\phi^0_{BTPPA^+} \qquad (5.1)$$

with $E_{Ag/AgCl} = 0.320$ V for the present system and $\Delta\phi_{BTPPA^+} = -0.405$V

This calculation was carried out assuming that the diffusion coefficients of the redox species are the same ($D_R = D_O$), with the concentration of the two redox species equal at the half wave potential, while ignoring the different ionic activity coefficients. The result of this analysis is given in Table 5.2:

Table 5.2 Half wave potential $E_{3,½}$, standard potential E^0 and diffusion coefficient D values for the organic redox species, cell 3

Species	$E_{½}$ /V vs. WRO	E^0/V vs. SHE	E^0/V vs. SHE*	$D \times 10^6$/ $cm^2 s^{-1}$
Fc	0.690	0.615	0.640	9.5
DiMFc	0.570	0.485	0.550	21
DcMFc	0.140	0.055	0.070	5.9

*Formal potentials based on experimental measurements against Fc^+/Fc couple[4]

Three electrode voltammetry was also carried out with a macroelectrode (BAS Pt, d=3 mm) as the working electrode. The cyclic voltammograms for DiMFc and DcMFc were stable and consistent, although quasi-reversible in the absence of IR compensation. Based on the Randles-Sevcik equation the diffusion coefficient for DiMFc was estimated to be D=5.91 x 10^{-6}cm^2 s^{-1}.

5.3 Electron transfer measurements with a four-electrode cell.

Interfacial electron transfer was measured directly with the four-electrode cell. The same reference junction was used for the four-electrode cell, 4a:

		(wro)	**(o)**	**(w)**	
			Pt	***Pt***	
Cell 4a:	*Ag/AgCl*	0.01 M LiCl	0.0001 M x-Fc	Aq. Redox couple	***Ref***
		0.001 BTPPACl	0.001 BTPPA TPB	Aq. Electrolyte	

With x=-, DiM-, DcM-, the different ferrocene derivatives, while various ratios for the aqueous redox species, and different aqueous supporting electrolytes and reference electrodes were used, indicated in every case.

As was established in the Chapter 1, in the case of oxidation of organic species, its redox potential should lie just below the equilibrium potential established by the aqueous redox couple, so that no spontaneous ET takes place. If the extra necessary potential difference ($\Delta\phi$) needed is provided externally to the interface, the interfacial ET process between the organic and aqueous redox species takes place. This potential difference needs however to be close to zero or in the order of mV, in order to be observed within the potential window established by the electrolytes. Within this window as well, it is necessary that no other charge transfer processes occur, (for example ion transfer) since such processes would contribute to the ET current measured and therefore impede the study of ET.

5.3.i Interfacial ET with DcMFc at the liquid/liquid interface

Interfacial ET was attempted between DcMFc [E^0=0.055 V] and the hexacyanoferrate couple [E^0=0.490 V]. The potential difference between the two species established spontaneous ET that could not be "shut off" by external polarisation within the available potential window. Instead an offset of current was observed as shown in Figure 5.4, indicating that the ET process was taking place over the whole potential window established, and therefore could not be further studied by this technique.

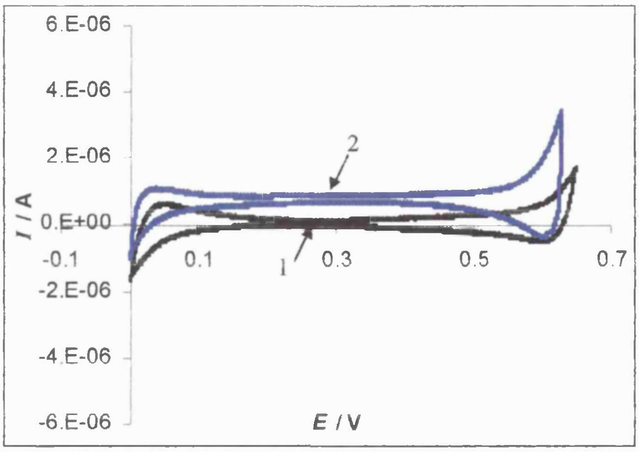

Figure 5. 4 Cyclic voltammograms for cell 4a, (black line 1): base CV in the absence and (blue line 2): in the presence of 0.01M/0.1M $Fe^{II/III}(CN)_6$, υ=25 mVs^{-1}, A= 28 mm^2.

Next the aqueous $Fe^{II/III}$(Citrate) couple [E^0=0.090 V] was tried using two different organic electrolytes, (THepATPB and BTPPATPB), known to establish large potential windows. The electron transfer was found to be impossible to study within the potential windows established by this technique. However interfacial electron transfer could be observed for DcMFc with hexaamineruthenate [E^0=0.065 V] as the aqueous redox couple. In the absence of either redox species the base potential window is shown in Figure 5.5.a. The effect of interfacial ET is shown in Figure 5.5.b:

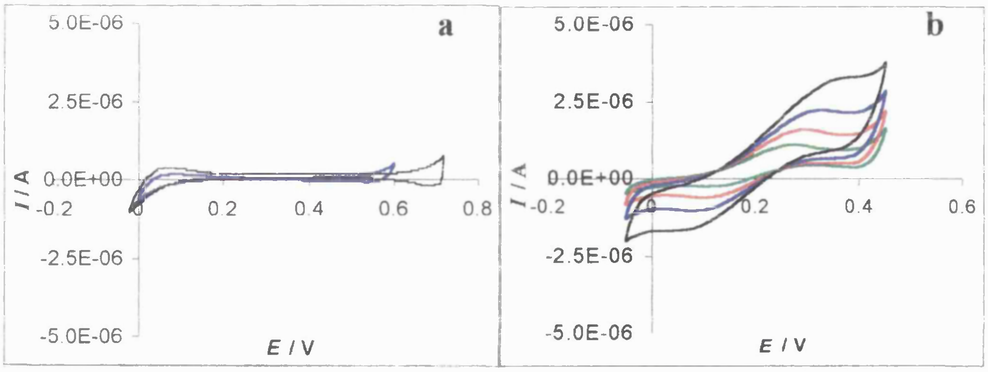

Figure 5. 5 Cyclic voltammograms for cell 4, (a): Base CV in the absence of DcMFc (blue line) and $Ru^{II/III}(NH)_3$ (black line) (b): interfacial ET for DcMFc and 0.01 M/ 0.1 M $Ru^{II/III}(NH)_3$, A= 28 mm^2, υ=10, 25,50,100 mV/s.

After maximum IR drop compensation, the process looked quasi-reversible with peak separation of 200 mV.

5.3.ii Interfacial ET with DiMFc at the liquid/liquid interface

Figure 5.6 illustrates the oxidation of DiMFc [E^0=0.485 V] by the aqueous hexacyanoferrate redox couple [E^0=0.490 V]. The potential window in the absence of either redox species is shown in Figure 5.6.a. The cyclic voltammetry of the interfacial ET is shown in Figure 5.6.b:

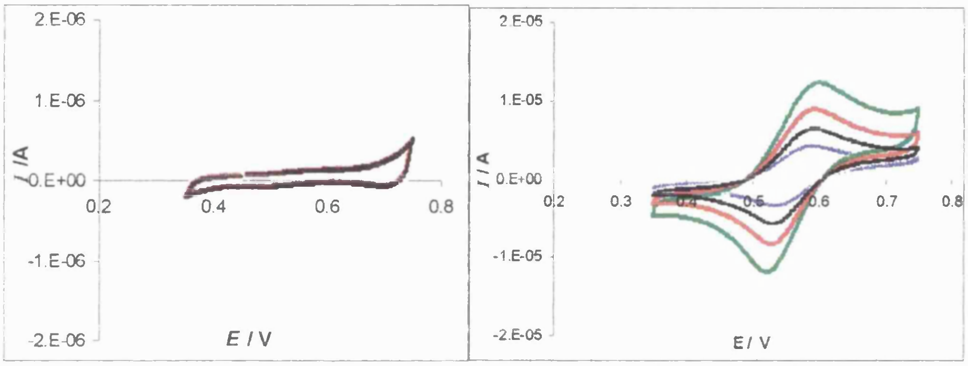

Figure 5. 6 Cyclic voltammograms of interfacial ET between 0.1mM DiMFc in 1,2- DCE, with a reference junction: *Ag/AgCl*/0.001M BTPPA Cl/ 0.001M BTPPA TPB and the aqueous 0.01 M/ 0.1 M $Fe^{II}/Fe^{III}(CN)_6$ in 1.5M $LiSO_4$, with Pt as a ref, cell 4, A= 28 mm^2, υ=10,25,50,100 mV/s.

Figure 5.6.b shows that ET was a reversible process with peak separation ≈60 mV. The small difference between the forward and reverse scan peak currents could be attributed to charging current, or difference in the diffusion coefficients of the two different species (charged and neutral DiMFc). Based on the Randles-Sevcik equation, the peak currents obtained from Figure 5.6.b, were plotted against the square root of the sweep rate to produce a linear fit, shown in Figure 5.7. From the slope, the diffusion coefficient was calculated to give D=5.8 x10^{-6} cm^2 s^{-1}, almost half than observed for microelectrode experiments, but very similar to the 3-electrode measurement at the macroelectrode (d=3mm).

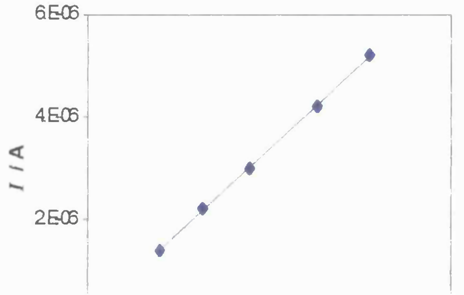

Figure 5. 7 Plot of the peak currents based on the forward scan of the data presented in Figure 5.6 with the square root of the sweep rate. Sweep rates 10,25,50,100,150 mV/s.

5.3.iii Effect of aqueous redox ratio on $E_{1/2}$ of interfacial ET

The process of the reversible interfacial electron transfer between DiMFc and the hexacyanoferrate couple was further studied. The effect of different ratios for the aqueous redox couple, using cell 4 was investigated. When using a Pt wire in the aqueous phase as a pseudo-reference electrode in cell 4, for three different concentration ratios, the resulting voltammograms are shown in Figure 5.8:

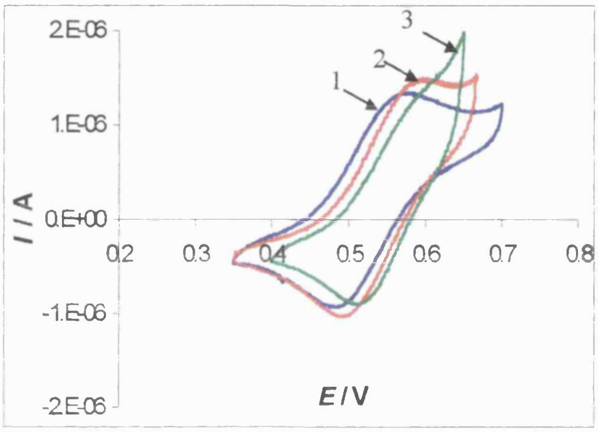

Figure 5. 8 CV of interfacial ET between 0.0001M DiMFc, and different concentration ratios for the aqueous $Fe^{II}/Fe^{III}(CN)_6$ in 1.5M $LiSO_4$ with Pt as a ref, using cell 4, (blue line 1): 0.01M/0.1M, (red line 2): 0.1M/0.1M and (green line 3): 0.1/0.01. A= 28 mm², υ=25mV/s.

There was a very small effect of the concentration ratio of the aqueous redox couple on the experimental half wave potential. The cyclic voltammograms showed $E_{4,1/2}$ ≈570 mV vs WRO for all ratios. Figure 5.9 shows the different cyclic voltammograms obtained for the three different concentration ratios, when SCE was used as the aqueous reference electrode in cell 4:

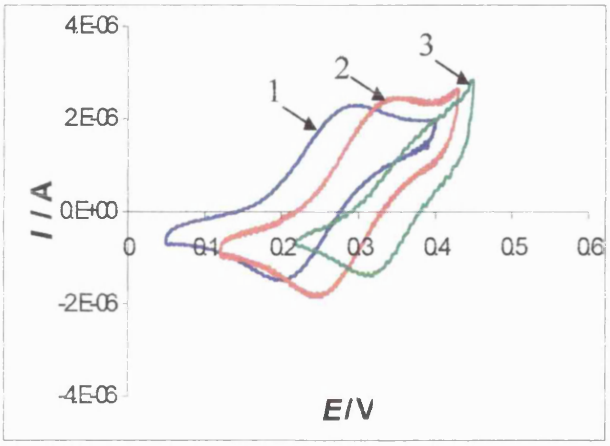

Figure 5. 9 CV of interfacial ET between DiMFc, as above and different ratios for the aqueous $Fe^{II}/Fe^{III}(CN)_6$ as in Figure 5.9 with SCE as a ref. A= 28 mm², υ=25mV/s.

The effect on the observed half wave potential was evident in this case, where there was a significant change in the half-wave potential difference measured for different concentration ratios of the aqueous redox couple, in contrast to results shown in Figure 5.8. The values of the half wave potentials are given in Table 5.3 as they are discussed next.

5.4 Discussion on electron transfer at a polarisable interface

The restrictions and difficulties related with matching potentials, were probably the reason why the interfacial ET for DcMFc (E^0=0.055V) has not been properly reported in the literature. Cunnane *et al.*[150] studied the interfacial ET between decamethylferrocene and the $Fe^{II/III}$(Citrate) couple. They showed that the process was so irreversible that it was not possible to record a proper CV within the established window. The irreversibility of this system was also established in the present work even in the presence of different electrolytes that provided large potential windows.

The discrepancy between diffusion coefficients at microelectrodes and liquid/liquid interfaces has already been reported for DiMFc[150]. This was attributed to a catalytic cycle at the microelectrode involving oxidation of ferricenium by TPB^- from the supporting electrolyte. However, Quinn *et al.*[151], by using inert anions for the supporting electrolyte, have shown that this interpretation was incorrect and discrepancies are due to formation of precipitates at the liquid-liquid interface or due to partitioning of $DiMFc^+$ produced. In the latter work it was also suggested that the oxidation of DiMFc was far from ideal and can be impaired by side reactions and precipitates at the interface. In the present work these side-reactions have been investigated further (see Appendix III) and it was concluded that provided the conditions are controlled and the potential range used restricted ($\Delta\phi$>-0.260 V), an ideal behaviour of ET with DiMFc was ensured.

The effect of different ratios for the aqueous redox couple is further considered here. The experimental half wave potential for interfacial ET, from Figure 5.8 was $E_{4,½}$ =0.575 V for all ratios used. As before, this value is corrected to give a value for $\Delta\phi_{½,\ \mathrm{ET}}$ based on the Galvani potential scale, where potential values are corrected vs. a common reference electrode in one phase, e.g. the aqueous SHE, based on IUPAC cell notations (see Introduction, equation (1.22)). In this case, for the highest ratio used, (10:1), $E_{\mathrm{Aq.Ref}}=E_{\mathrm{Rest}\ (10:1)}$ and from the value taken from Table 3.5:

$$\Delta\phi_{½,E.T} = E_{4,½} + E_{Ag/AgCl} + \Delta\phi^{0}_{BTPPA^{+}} - E_{Aq.\mathrm{Re}f} \quad \textbf{(5.2)}$$

$$= 0.575 + 0.320 + (-0.400) - 0.545 \quad = -0.055\mathrm{V}\ vs\ SHE$$

The latter value is the half wave Galvani potential difference, $\Delta\phi_{½,\ \mathrm{ET}}$, for interfacial ET between DiMFc and the 10/1 ratio of the aqueous $\mathrm{Fe^{III}/Fe^{II}(CN)_6}$ used, with Pt as a reference electrode.

This value can be compared with another calculation of the half wave potential, $\Delta\phi_{1/2,\mathrm{ET}}$, from the difference between the standard redox potential of the organic species $E^0_{(o)}$ and the equilibrium potential $E_{\mathrm{Eq(w)}}$ of the aqueous redox couple (see introduction, equation (1.21)):

$$\Delta\phi_{\mathrm{ET}\ 1/2} = E^{0}_{\mathrm{DiMFc}} - E_{\mathrm{Eq(10/1)}} = 0.485 - 0.545 = -0.060\ \mathrm{V}\ vs\ SHE \quad \textbf{(5.3)}$$

The expected theoretical value was only slightly different to the experimental value obtained above. For different ratios, different values for $\Delta\phi_{1/2,\mathrm{E.T}}$ are obtained as shown in Table 5.3.

By rearranging equation (5.2) the experimental half wave potential, $E_{4,1/2}$, obtained from four electrode-potentiostat measurements is obtained:

$$E_{4,½} = -E_{Ag/AgCl} - \Delta\phi^{0}_{BTPPA^{+}} + \Delta\phi_{1/2,E.T.} + E_{Aq.\mathrm{Re}f} \quad \textbf{(5.4)}$$

with the half-wave Galvani potential difference $\Delta\phi_{1/2,\mathrm{ET}}$ given by equation (5.3). Therefore:

$$E_{4,½} = -E_{Ag/AgCl} - \Delta\phi^{0}_{BTPPA^{+}} + E^{0}_{(o)} - E_{Eq(w)} + E_{Aq.\mathrm{Re}f} \quad \textbf{(5.5)}$$

If a Pt wire is used as the aqueous pseudoreference electrode, $E_{Aq.Ref} = E_{Eq(w)}$. Therefore:

$$E_{4,½} = -E_{Ag/AgCl} - \Delta\phi^0_{BTPPA^+} + E^0_{(o)} \qquad \textbf{(5.6)}$$

The equilibrium potential established by different ratios of the aqueous redox species cancels out and $E_{1/2}$ measured in the liquid/liquid experiment is the same as that measured in a microelectrode experiment:

$$E_{4,½} = E_{3,½} \qquad \textbf{(5.7)}$$

Experimental results for the oxidation of DiMFc at the microelectrode and at the liquid/liquid interface, with a Pt wire as a reference electrode showed $E_{3_{1/2}} = 0.570mV$ and $E_{4_{1/2}} = 0.575mV$. Furthermore, cell 4 is a combination of cells 2 and 3:

$$E_{4,½} = E_{3,½} - E_{2,Eq(w)} \qquad \textbf{(5.8)}$$

In this case it can be crudely assumed that $E_{2,Eq} = 0$ using a Pt as a working electrode vs Pt as a reference.

On the other hand when SCE was used as a reference electrode, there was also a change in the experimental half wave potential difference measured with cell 4 for different ratios, shown in Figure 5.9. This can be attributed to the fact that for equation (5.5):

$$E_{4,½} = -E_{Ag/AgCl} - \Delta\phi^0_{BTPPA^+} + E^0_{(o)} - E_{Eq(w)} + E_{Aq.\mathrm{Re}f}$$

$E_{Aq.Ref}$ is not equal to $E_{2,Eq(w)}$ and therefore cannot cancel each other out. In this case equation 5.7 does not hold either, and the potential measured at a microelectrode is different to the one observed for the liquid/liquid interface. On the other hand equation (5.8) is still valid with the correction for the aqueous reference electrode being $E_{Aq.Ref} = E_{SCE\ vs\ SHE} = 0.244V$. The experimental and estimated values for the half wave potential using cell 4 with SCE as the reference electrode are given in Table 5.3, for the three different ratios.

Table 5.3 Predicted and experimental potential values for interfacial ET with various ratios of aqueous redox species concentrations, using SCE as a reference electrode, E^0_{DiMFc}=0.485 V

E_2/V *		$\Delta\phi_{1/2,E.T}$/V	**Estimated** **	**($E_{3,½}$-$E_{2,Rest}$)** ***	**Experimental**
Vs. SCE	***Vs SHE***	$=E_0 - E_{Eq}$	**$E_{4,½}$/V**	**$E_{4,½}$/V**	**$E_{4,½}$/V (SCE)**
10/1 : 0.302	0.545	-0.060 V	0.264 V	0.268	0.248
1/1 : 0.246	0.488	-0.003V	0.321 V	0.324	0.300
1/10 : 0.198	0.440	0.045V	0.340 V	0.372	0.370

*From Table 3.5 **From equation (5.4) ***From equation (5.8)

There is a discrepancy of about ±20mV but the experimental error has to be accounted for, together with the assumption made for the activity coefficients. The table provides a satisfactory corroboration for the theoretical analysis presented above. A suggestion is therefore made, it is only when Pt is used as a pseudo-reference electrode that there is no effect on the experimental half wave potential $E_{4,1/2}$ when altering the concentration ratio of the aqueous redox couple. In this case only, the experimental value obtained from Cell 4 with a four-electrode potentiostat at a liquid/liquid interface was found to be equal to the half wave potential value obtained from microelectrode experiments, $E_{3,1/2}$ vs WRO.

5.5 Interfacial electron transfer at a non-polarisable interface

In the case of non-polarisable interfaces, as explained in the Introduction (Chapter 1), the potential difference $\Delta\phi$ is constant, provided by partitioning ions that also maintain electroneutrality. The $\Delta\phi$ established must provide the driving force for the redox reaction across the interface. Meanwhile, it must also deter any extra ion transfer processes from occurring that could complicate the system studied. The interfacial ET for DiMFc with SECM has never been cited in the literature, as it has a very low Gibbs energy of transfer, ($\Delta\phi_{IT}$=–90mV), and the usual potential determining ions used establish an interfacial potential difference ($\Delta\phi$<–90mV) that promotes DiMFc$^+$ transfer [150].

5.5.i Interfacial ET with SECM

A potential difference of $\Delta\phi$=−30mV was established by an appropriate potential determining ion, $TPrA^+$, at a ratio of C_o/C_w =3/1. Alternative potential determining ions (TEA^+, TMA^+) that could be used instead in order to provide higher $\Delta\phi$, proved to have limited solubility in the organic phase. The literature value for the redox potential of DiMFc is higher than that of $Fe(CN_6)^{4-/3-}$. Therefore the inverse redox reaction, to that used so far was studied to ensure $\Delta E>0$. The cell described in section 3.3.ix was used:

At the electrode: $DiMFc \rightarrow DiMFc^+ + e^-$ (In the organic phase)

At the interface: $DiMFc^+ + Fe(CN_6)^{4-} \rightarrow DiMFc + Fe(CN_6)^{3-}$

The reduction of $DiMFc^+$ at the interface was monitored with:

	Pt (o)	(w)
Cell 5a	0.001 M DiMFc 0.1 M TPrATPB	x M $Na_4[Fe(CN)_6]$ 0.01 M TPrACl
	Ag	

The approach curves obtained for this system are shown in Figure 5.10 together with theoretical curves that provide the interfacial rate constants of this process.

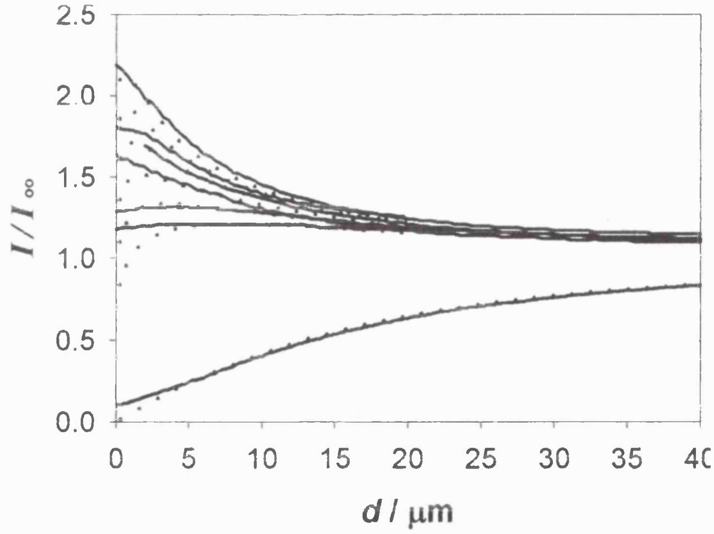

Figure 5. 10 Approach curves using cell 5a, with the approach curves (2μm/sec) of a microelectrode (Pt=12.5 mm, RG=10) in organic phase and the aqueous containing from top to bottom: (Solid lines): 0.01, 0.007, 0.005, 0.002, 0.001, 0.0007, 0 M $Na_4[Fe(CN)_6]$, (Dashed lines): theoretical curve fits, for top to bottom: k =11.2, 9.8,8.4,7,5.6, 4.2 cm $s^{-1}M^{-1}$, insulator.

It was established that for interfacial ET using DiMFc as an organic redox species, with increasing concentration of the aqueous redox species the rate of interfacial ET increases.

5.5.ii Interfacial ET with MEMED

The microelectrode used in the microelectrochemical measurements at an expanding drop (MEMED) also studied indirectly the interfacial ET process. It monitored the local changes in the ferrocyanide concentration near the drop surface where ET occurred between DcMFc [E^0=0.055 V] and ferricyanide [E^0=0.490 V] as soon as the two phases came into contact. The redox potential of DcMFc was lower than that of hexacyanoferrate and for the interfacial oxidation of DcMFc, ΔE=435 mV. The presence of ClO_4^- as a potential determining ion establishes a $\Delta\phi$ of –138 mV, that maintains favourability while ensuring that $DcMFc^+$ would not transfer ($\Delta\phi_{IT}$=310 mV)[152]:

At the interface: $DcMFc + Fe(CN_6)^{3-} \rightarrow DcMFc^+ + Fe(CN_6)^{4-}$

At electrode: $Fe(CN_6)^{4-} \rightarrow Fe(CN_6)^{3-} + e^-$ (In the aqueous phase)

For these experiments the following cell was used:

	(o)	**(w)**	
		0.001 M $Na_3[Fe(CN)_6].10H_2O$	***Pt***
Cell 5b:	0.01 M DcMFc	0.25 M $NaCLO_4$	
	0.1 M $THexACLO_4$	0.002M $NaHCO_3$	
		0.1 M NaCl	
		x M Triton X-100	***Ag/AgCl***

The two phases were not pre-equilibrated and the organic phase was an expanding droplet that finally came into contact with the electrode that is in the aqueous phase and detached. Typical current time transients for different flow rates for the feeder (organic) liquid are shown in Figure 5.11:

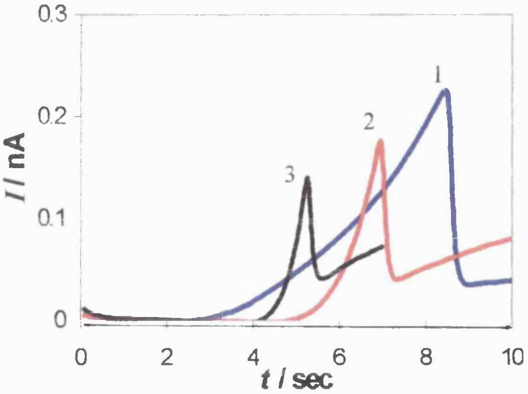

Figure 5. 11 Current-time transient for the oxidation of $[Fe(CN)_6^{4-}]$ at Pt ultramicroelectrode (a=2μm) in the aqueous phase, produced with the interfacial ET using Cell IV, with pH=7.7, as the expanding drop approaches the microelectrode with different flow rates, (blue line 1): 200μl/h, (red line 2):300μl/h, (black line 3): 400μl/h.

The current measured at the stationary microelectrode continuously increased as the drop/interface approached its tip, because the concentration of $[Fe(CN)_6^{4-}]$ increased near the interface. Figure 5.10 also shows the difference of the transient shape at different flow rates used, i.e. for different approach rates of the interface to the tip. When the drop touches the interface there was a sudden decrease, denoting the contact point. The local mass transport to the electrode was by steady state diffusion only, as the electrode used was very small and its diffusion layer $\approx 100\mu m$. The diffusion relaxation time then was fast compared to the rate of movement of the drop and diffusion was rapid compared to convection.

5.6 Discussion on interfacial ET at a non-polarisable interface

SECM measurements are presented for the interfacial reaction of $DiMFc^+$ with $TPrA^+$ as the potential determining ion (PDI). However the potential difference established by this PDI, in order to deter ion transfer of $DiMFc^+$ is close to the value for $\Delta\phi_{IT}$. In this case ion transfer of the dimethylferricenium ion produced should be taken into account, which would complicate the calculation of *k* from the analysis of the SECM curves. Therefore, further studies of interfacial ET at a non-polarisable interface were carried out using DcMFc as an organic species, that has a very low value of $\Delta\phi_{IT}$=-310mV[152] and is widely used in similar systems. A thorough SECM study and kinetic analysis of the interfacial ET with DcMFc was carried out by Zhang and Unwin[153]. The effect of surfactants on this well characterised interfacial process will be presented in Chapter 6.

Further work was also carried out with the MEMED system of DcMFc and hexacyanoferrate by Zhang *et al.*[154]. In this work the authors suggest that the system is not straightforward, as the interfacial ET rate constant increases with an increase in $\Delta\phi_i$ established by ClO_4^-. However, it is suggested here that this system actually exhibits a normal behaviour. With an increase in $\Delta\phi$ the driving force (ΔE+$\Delta\phi$) increases therefore the rate of ET also increases.

An attempt was made here to study similar systems with the two different electrochemical techniques. However the interfacial ET of DcMFc at a polarisable interface was found to be irreversible, whereas DiMFc exhibited a reversible behaviour. On the other hand, the interfacial ET of DiMFc at a non-polarisable interface could be complicated by the resulting ion transfer process of $DiMFc^+$, whereas the DcMFc is not complicated by this process. Further studies, in the presence of surfactants will be presented for the most reversible and straightforward system in each case, and comparisons are made assuming that the ferrocene derivatives have similar behaviour at the liquid/liquid interface.

5.7 Conclusions

- Individual redox processes were studied and characterised in respective phases in order to provide parameters such as diffusion coefficient and standard potentials.
- Interfacial ET with four-electrode voltammetry is not very facile and can only be established by combining appropriate electrolytes and redox species. DiMFc with hexacyanoferrate was established as a reversible system, while DcMFc with hexamineruthenate was irreversible.
- The half wave potential of the four-electrode cell can be estimated. It is equal to the half wave potential of the microelectrode experiment for the oxidation of the organic species at the electrode: $E_{4,½} = E_{3,½}$ when Pt is used as a pseudoreference electrode. For all other reference electrodes: $E_{4,½} = E_{3,½} - E_{2,\mathrm{Re}\,st}$, with $E_{2,\mathrm{Re}\,st}$ the rest potential of the aqueous redox couple present.
- The role of a PDI for the SECM and MEMED measurements is very important. The interfacial ET of both DcMFc and DiMFc were studied, but the latter was complicated by possible ion transfer.

Chapter 6: Effect of adsorbed surfactants on electron transfer

In chapter 4 the adsorption of non-ionic surfactants at the liquid/liquid interface was shown, followed by chapter 5, where systems of interfacial electron transfer across this interface were established. In this chapter the effect of the adsorbed surfactant on these interfacial electron transfer processes will be presented. The study of this effect is explored both at the ionically polarisable and non-polarisable interface. The effect of the surfactants on the electrochemistry of the individual components in either phase was also established. The solubilities of the surfactants in either phase and the procedure followed were described in the experimental part (chapter 3).

6.1 Voltammetric studies on the effect of surfactants in either phase

6.1.i Effect of surfactants on oxidation of $[Fe(CN)_6]^{4-}$ at Pt

Initially the effect of both surfactants on the oxidation of the aqueous redox species at a Pt microelectrode was studied, using a two-electrode configuration.

Cell 2b:	*Ag/AgCl*	**(w)** 0.001M $Na_4Fe(CN)_6$. 0.01 M NaCl x mM Surfactant	*Pt(25μm)*

The linear sweep voltammograms obtained using cell 2b in the absence and presence of the surfactants are given in Figure 6.1:

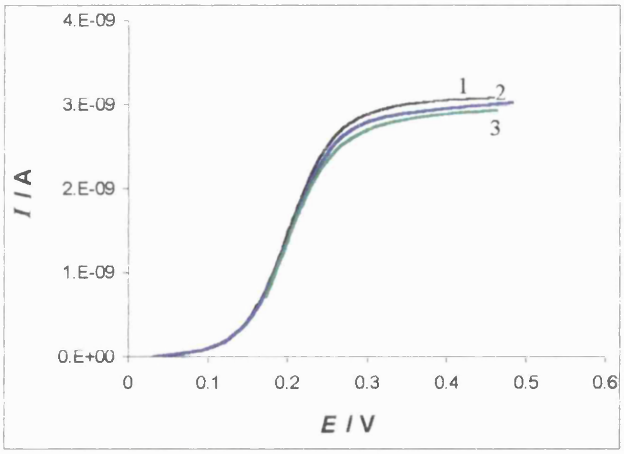

Figure 6. 1 Cyclic voltammogram for the oxidation of 1mM $Na_4Fe(CN)_6$ using cell 2b (Black line 1): no surfactant present, (Blue line 2): 0.5mM Triton and (Green line 3): 0.5mM SM. A= 20 μm², υ=10 mV/s.

It was established that the presence of either surfactant in the aqueous phase did not affect the electrochemical properties of the aqueous redox species, within experimental error. Similar cyclic voltammograms were carried out prior to every SECM approach curve transient.

6.1.ii Effect of surfactants on oxidation of x-Fc at Pt

The effect of the presence of the surfactants in the organic phase was also studied, using again a two-electrode configuration.

Cell 3b:	*Ag/AgCl*	**(wro)** 0.01 M LiCl 0.001MBTPPA Cl	**(o)** 0.01 M DiMFc 0.001 M BTPPA TPB x mM Triton x-100	*Pt (50 μm)*
Cell 3c:	*Ag/AgCl*	**(wro)** 0.1 M $NaClO_4$	**(o)** 0.01 M DcMFc 0.01 M $ThexAClO_4$ x mM SM	*Pt (25 μm)*

The cyclic voltammograms obtained using cells 3b and c in the absence and presence of the surfactants are given in Figure 6.2:

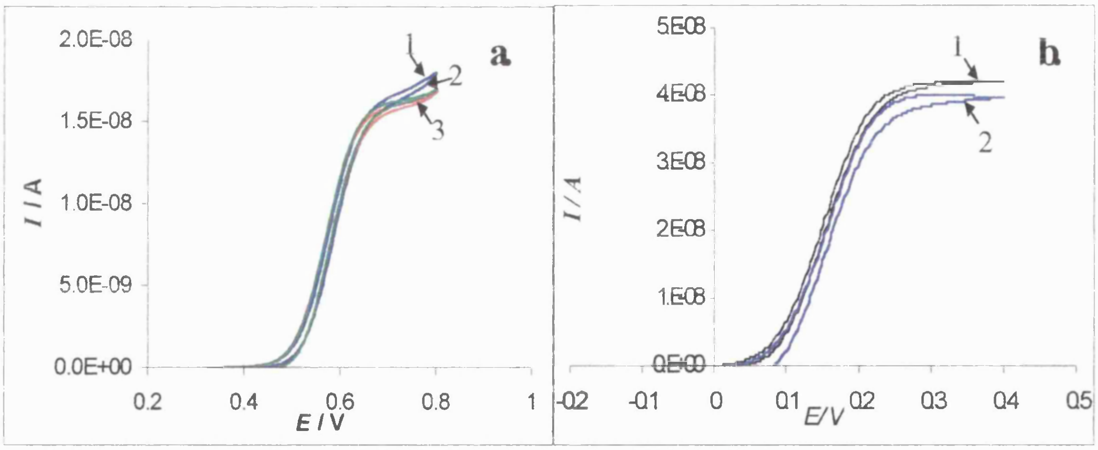

Figure 6. 2 a. Cyclic voltammogram of 0.01M DiMFc using cell 3b, (blue line 1): no surfactant, and addition of (green line 2) of 0.2 mM and (black line 3): 0.4mM Triton x-100
b. Cyclic voltammogram of 0.01M DcMFc using cell 3c, (black line 1) no surfactant and addition of (blue line 2) of 0.2 mM SM. A= 20 μm², υ=10 mV/s.

Both Figures 6.2 a and b establish that there was little to no effect of the surfactants' presence in the organic phase, while studying the oxidation of either of the organic redox species.

6.2. Results for electron transfer measurements in the presence of surfactant at a non-polarisable interface

6.2.i MEMED studies on effect of Triton X-100

In chapter 5 interfacial ET reaction in the absence of surfactants was studied and characterised using the MEMED technique under different flow rates. The study of the effect of surfactants on the following process was explored using cell 5c:

At the interface: $DcMFc + Fe(CN_6)^{3-} \rightarrow DcMFc^+ + Fe(CN_6)^{4-}$

At electrode: $Fe(CN_6)^{4-} \rightarrow Fe(CN_6)^{3-} + e^-$

	(o)	(w)	
Cell 5c:	0.01 M DcMFc 0.1 M ThexAClO$_4$	0.001 M Na$_3$[Fe(CN)$_6$].10H$_2$O 0.25 M NaClO$_4$ 0.002M NaHCO$_3$ 0.1 M NaCl x M Triton X-100	***Pt*** ***Ag/AgCl***

A range of different additions to the aqueous phase from a stock solution of surfactant allowed a range of different bulk concentrations to be studied. The current-time transients were measured again under different flow rates. Figure 6.3 shows typical MEMED curves for one specific flow rate, 200 µl/h, in the absence and presence of surfactant.

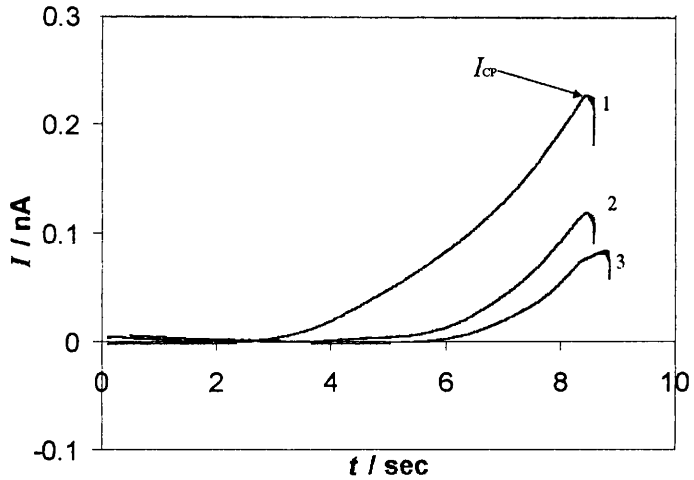

Figure 6. 3 Current-time transients for the oxidation of $Fe(CN)_6^{-4}$ at the Pt microelectrode in the aqueous phase, produced following interfacial ET, using cell 5c, in the absence of surfactant (line 1) and in the presence of 0.25 mM: (line 2) and 0.50 mM: (line 3) Triton X-100. Flow rate 200 µl/h,

Each surfactant addition lowered the current detected at the electrode as the drop approached it, suggesting that the rate of interfacial ET decreased. In order to further explore the effect of adsorbed surfactants on interfacial ET reaction a characteristic value of the MEMED *I-t* transients was chosen, i.e. the maximum current obtained at contact point (I_{CP}) prior to the expanding drop touching the electrode. Figure 6.4 shows the variation of I_{CP} with various surfactant concentrations, normalised with the current obtained in the absence of surfactant, for each flow rate, showing similar effect with all flow rates used.

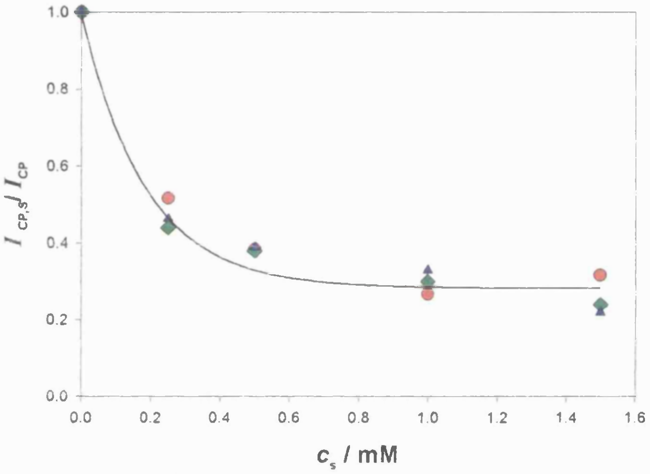

Figure 6. 4 Effect of Triton X-100 on the normalised current I_{CP}, as in Figure 6.3 for different flow rates, 200μl/h (circles), 300μl/h, (diamonds), 400 μl/h (triangles)

6.2.ii SECM studies on effect of sorbitan monostearate

The effect of adsorbed sorbitan monostearate, SM, with DcMFc was studied with the SECM technique:

At electrode: $Fe(CN_6)^{4-} \rightarrow Fe(CN_6)^{3-} + e^-$

At the interface: $DcMFc + Fc(CN_6)^{3-} \rightarrow DcMFc^+ + Fc(CN_6)^{4-}$

Cell 5d:	**(o)** 0.01 M DcMFc 0.1 M ThexAClO$_4$ **x M SM**	**(w)** ***Pt*** 0.001 M Na$_4$[Fe(CN)$_6$] 1 M NaClO$_4$ ***Ag***

For these experiments, partitioning of perchlorate ion established the interfacial potential difference ($\Delta\phi$=−138 mV) well negative of the pzc, ensuring surfactant adsorption in a regime where the coverage was potential-independent, as established from capacitance measurements. The approach curves for increasing surfactant concentrations are shown in figure 6.5:

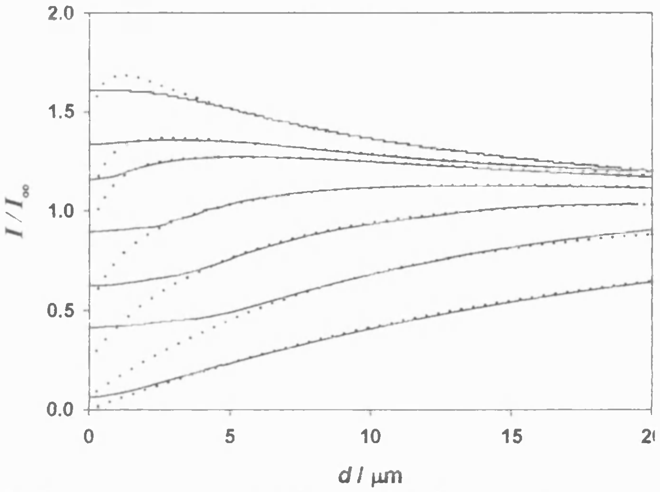

Figure 6. 5 Set of SECM approach curves using cell 5d. The experimental curves are shown as solid lines, with surfactant concentrations from top to bottom: 0, 0.1 mM, 0.2 mM 0.5 mM, 1 mM, 5 mM. The corresponding theoretical curves are shown in dashed lines (see text).

The top SECM approach curve of Figure 6.5 illustrates the current enhancement due to the regeneration of ferrocyanide by the interfacial reaction whereas the bottom curve shows the current decrease due to the approach to an insulator. Adsorption of surfactant caused a decrease in the feedback current, which was attributed to a diminution in the rate of the ET process at the liquid/liquid interface. Each approach curve was fitted to theory, to allow the rate constant for the ET process to be obtained. The fitting of approach curves and determination of the distance of closest approach followed the procedures have been outlined in detail elsewhere[153]. The theoretical simulations were based on the assumption that the surfactant covers the surface in patches and that surfactant patches are inactive for the interfacial ET reaction[153]. Figure 6.6 shows the decrease of the bimolecular rate constant with increasing surfactant concentration:

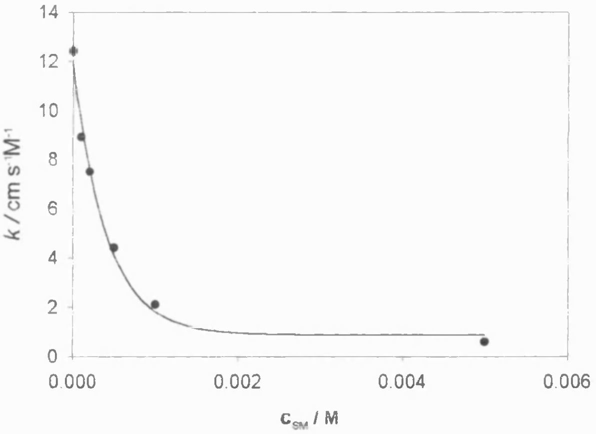

Figure 6. 6 Effect of SM on the bimolecular rate constant obtained from the SECM approach curves in figure 6.4, with increasing surfactant concentration.

6.3 Results for electron transfer measurements in the presence of surfactant with four-electrode voltammetry

The literature work on charge transfer across adsorbed layers presented in chapter 1 implies that the transport of ionic species through adsorbed layers to the interface might be more facile than that of uncharged species, in the absence of effects due to the surface potential induced by adsorbed charged species.[155-157] It has been already established that non-ionic surfactants adsorbed at the liquid-liquid interface form patches that greatly inhibit interfacial ET at an ionically polarisable interface.[153,158] Since four-electrode measurements on ET necessarily monitor a change of charge, they could highlight different effects of the adsorbed layer on the approach of charged and uncharged species to the interface.

6.3.i Effect of Triton X-100

The effect of the aqueous soluble Triton X-100 surfactant on interfacial ET was studied initially.

Cell 4b:	*Ag/AgCl*	**(wro)** 0.02 M LiCl 0.001M BTPPACl	**(o)** *Pt* 0.001 M DiMFc 0.001 BTPPA TPB	*Pt* **(w)** 0.1 M $Fe(CN)_6^{3-}$ 0.01 M $Fe(CN)_6^{4-}$ x M Triton X-100	*Pt*

Figure 6.7 shows some preliminary results of the effect of Triton X-100 on interfacial electron transfer process using cell 4b. In this case the aqueous redox couple was $Na_4Fe(CN)_6$ /$Na_3Fe(CN)_6$:

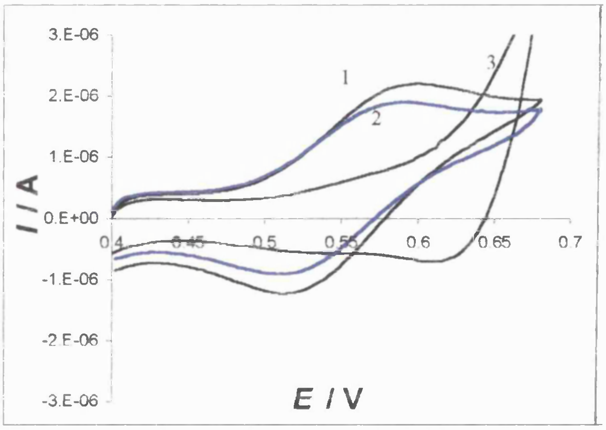

Figure 6. 7 Cyclic voltammograms of interfacial ET between DiMFc and 0.1 M $Na_3Fe(CN)_6$ and 0.01 M $Na_4Fe(CN)_6$. (Black line 1): no surfactant present, (Blue line 2): 0.15 mM and (green line 3) 0.35 mM Triton x-100, A= 28 mm², υ=25 mV/s.

The first addition of the surfactant had a significant effect on the peak current of interfacial ET. The current decreased for both the forward and the backward scan with a slight shift of the peak potentials. The second addition of a substantial concentration of the surfactant (>CMC) appeared to completely inhibit the electron transfer process, with both voltammogram peaks disappearing. Further studies on the effect of Triton X-100 with cell 4b were carried out with $K_4Fe(CN)_6$ /$K_3Fe(CN)_6$ as the aqueous redox couple. Figure 6.8 shows that in this case in the presence of Triton X-100 another charge transfer process at the interface takes place, in the absence of DiMFc.

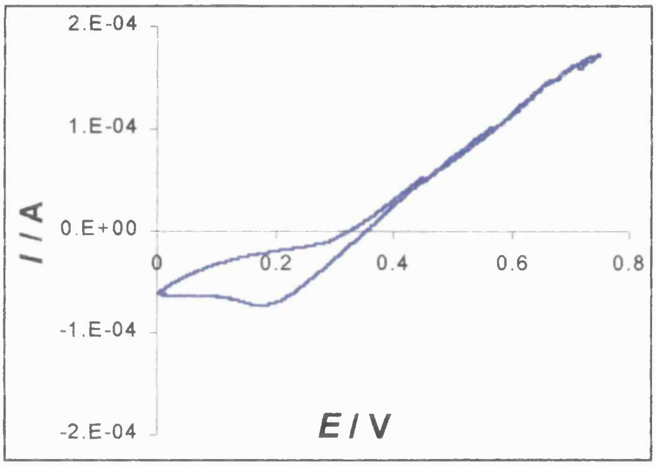

Figure 6. 8 Effect of the presence of 0.250 mM of surfactant Triton X-100, on the base potential window of Cell 4b in the presence of 0.1 M $K_3Fe(CN)_6$ and 0.01 M $K_4Fe(CN)_6$, A= 28 mm^2, υ=25 mV/s.

It is suggested that as the aqueous phase became more positive with respect to the organic phase in the presence of surfactant Triton X-100 an onset of facilitated ion transfer resulted in currents of the mA range. This was observed in the presence of potassium ions either as an electrolyte or in the ferrocyanide couple. For potentials E>0.350 V, Triton X-100 seemed to complex with the aqueous potassium ions and transfer them in the organic phase. In this case, the presence of Triton X-100 restricted the base potential window within a range of E=0.100-0.350 V using cell 4b. However, for this cell, interfacial ET process takes place for potentials E>0.350 V, therefore the onset of the facilitated ion transfer process prevented any further study by four-electrode voltammetry of electron transfer in the presence of Triton X-100.

6.3.ii Effect of sorbitan monostearate

The effect of SM on the base potential window was already established in Chapter 4.

		(wro)	(o)	(w)	
Cell 4c:	*Ag/AgCl*	0.01 M LiCl 0.001 M BTPPACl	***Pt*** 0.001 M DiMFc 0.001 BTPPA TPB x M SM	***Pt*** 0.1M $K_3Fe(CN)_6$ 0.01M $K_4Fe(CN)_6$ 1.5 M $LiSO_4$	***Pt***

Figure 6.9 shows the effect of various SM concentrations in the organic phase on interfacial ET using cell 4c.

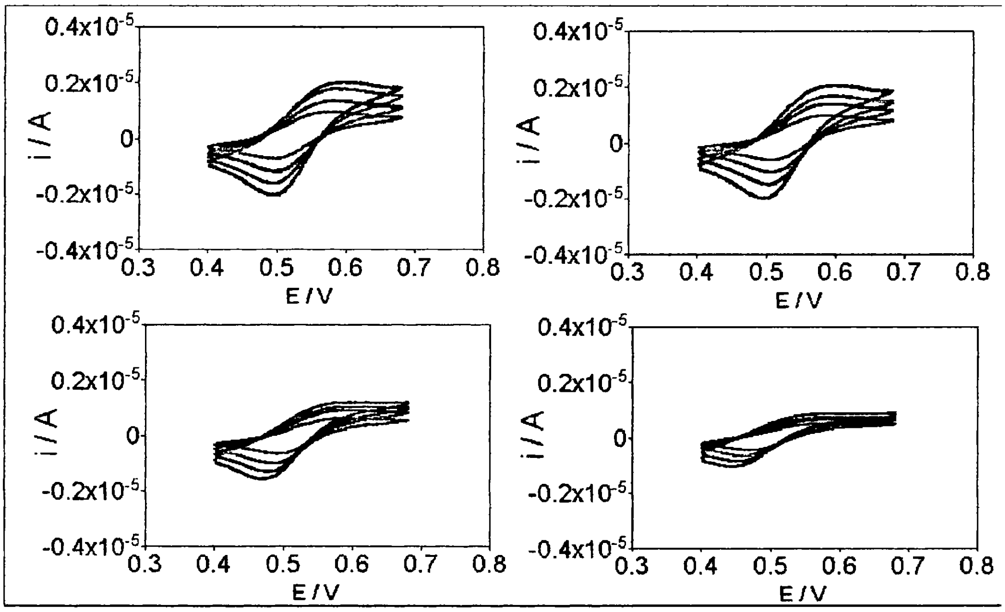

Figure 6. 9 Cyclic voltammograms showing the effect of different SM concentrations on the interfacial ET between 0.1mM DiMFc and the ferro-ferricyanide couple, using cell 4c. From left to right, top: SM= 0.7, 1 mM, and bottom: 2, 5 mM, A= 28 mm^2, υ=10, 25, 50, 100, mV/s.

In the absence of both redox couples, within the window established there was no current across the interface by transfer of the supporting electrolyte, and no effect of surfactant. Figure 6.9 shows how the reversible interfacial ET, seen in the absence of surfactant, was inhibited by addition of surfactant. As the surfactant concentration was increased from zero, the effect on the ET process depended on the direction of the reaction. For the reduction of DiMFc$^+$ (reverse sweep), the effect on the peak shape was as expected for an ET process becoming progressively more irreversible with increase of surfactant concentration: the peak simply shifted to more negative values of the interfacial potential difference, and broadened. For the oxidation of DiMFc however (forward peak), the effect was different: the peak developed into a plateau of significantly reduced magnitude and independent of scan rate.

6.4 Discussion

Section 6.1 established that there was no effect of the surfactant's presence on the electrochemistry of the individual components in either phase. Therefore any effect observed in the presence of surfactant on the interfacial ET response was attributed due to the adsorption of the surfactant at the liquid/liquid interface.

The MEMED measurements depicted in Figures 6.3 and 6.4 show that there was a significant decrease of measured current in the presence of increasing Triton X-100 concentration. The CMC of Triton X-100 is 300 μM, therefore the saturation of the interface in the presence of concentrations *c*>CMC can be understood. Figure 6.4 shows that the effect of the surfactant was the same for all flow rates used. It is suggested that the bulk concentrations used here and the transport rate to the continuously expanding interface were very high. This resulted in surfactant coverage of the interface that was at equilibrium for all expanding drop flow rates used. Further MEMED studies on the effect of lower concentration range of Triton X-100 on a system where instead of DcMFc, TCNQ was used, were carried out by Zhang *et al.*[158]. They developed a numerical model for the surfactant adsorption at a symmetrically growing sphere of one fluid in the other, where spontaneous ET occurs. Their data was satisfactorily explained using a model, which assumed that adsorption of surfactant was Langmuirian and that ET occurred only at the interface that was free of surfactant. The same idea can be applied to the data of Figure 6.4, bearing in mind the high concentration range used. In this case θ_s reaches a maximum value $\theta_{s,max}$, which is the value obtained in equilibrium with surfactant micelles above the CMC. The equilibrium of free surfactant and surfactant in micelles is normally written:

$$mS \xleftrightarrow{Km} S_m \qquad \textbf{(6.1)}$$

$$\text{with } K_m = {[S_m]}\big/{[S]^m} \qquad \textbf{(6.2)}$$

and $c = [S] + m[S_m]$, where *c* is the total surfactant concentration and m the amount of molecules that micellise

The equilibrium of free and adsorbed surfactant can be written, assuming a Langmuir isotherm.

$$S \xleftrightarrow{Kads} S_{ads} \qquad \textbf{(6.3)}$$

$$\text{with } K_{ads} = \frac{\vartheta}{(1-\vartheta)[S]} \qquad \textbf{(6.4)}$$

Substituting $[S]^m$ from equation 6.2 gives an equation for the concentration

$$c = [S] + mK_m[S]^m \qquad \textbf{(6.5)}$$

Above CMC, since $[S_m] >> [S]$, equation 6.5 reduces to $c \approx mK_m[S]^m$ and $[S] = \sqrt[m]{\frac{c}{mK_m}}$ whereas for *c* sufficiently lower than CMC, $c \approx [S]$.

Assuming that the surfactant-covered area completely inhibits ET, then

$$1-\vartheta \approx \frac{I_{CP,s}}{I_{CP}} \qquad \textbf{(6.6)}$$

It is therefore suggested that for concentrations sufficiently below CMC:

$$\frac{\vartheta}{1-\vartheta} \approx K_{ads}c \qquad \textbf{(6.7)}$$

whereas for concentrations sufficiently higher than CMC

$$\frac{\vartheta}{1-\vartheta} \approx K_{ads}\sqrt[m]{\frac{c}{mK_m}} \qquad \textbf{(6.8)}$$

Plotting $\log[\theta/(1-\theta)]$ vs. log*c* in Figure 6.10, revealed the two regions proposed

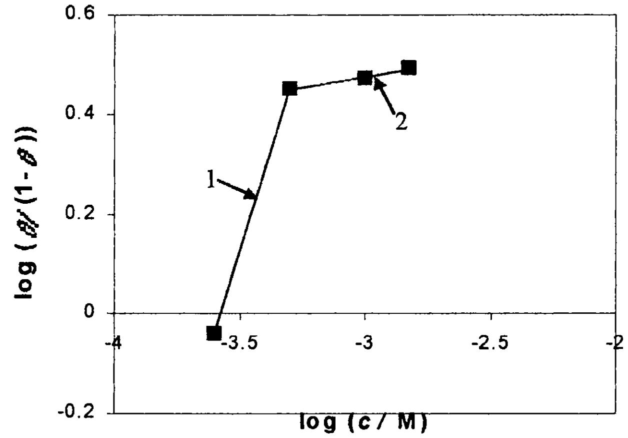

Figure 6.10 Treatment of surface coverage obtained from Figure 6.4 at 200 μl h^{-1}, for two different concentration ranges, (1): below CMC, (2) above CMC.

Despite the limited MEMED data available, an extrapolation for $\log[\theta/(1-\theta)]=0$, at low concentrations results in an adsorption constant of $K_{ads}=4\text{x}10^3$ M^{-1}, whereas from the high concentration range the slope (1/m) suggest a value of m=14. This value is very low but can be justified within experimental error and considering the assumptions madc.

As noted above, Zhang *et al.*[153] used a Langmuirian model also for SECM studies of the effect of Triton X-100 adsorption on ET with DcMFc, where they observed that the rate constant for c_b<CMC decreased to 15% of its initial value in the absence of surfactant. Moreover, Figure 6.4 shows that the measured current for all flow rates decreased at high concentrations to 35% of its initial value in the absence of surfactant. The effect of the organic soluble SM on interfacial ET was more profound than that of the aqueous soluble Triton X-100. From Figure 6.6 a 95% decrease on the interfacial rate constant was observed with the organic soluble SM. At near CMC concentrations ET was almost completely inhibited. The effect of SM observed with SECM could also be understood with a similar adsorption model, as outlined elsewhere[153], based on the assumption that surfactant patches block ET. It was therefore possible to estimate the surface coverage at each surfactant concentration:

$$\theta = \frac{k - k_s}{k} \tag{6.9}$$

where k_s (cm s^{-1} M^{-1}) is the bimolecular rate constant in presence of SM and k the rate constant in the absence of surfactant.

This analysis was based on the hypothesis that interfacial ET occurs only at the uncovered area of the interface, and the proposed model is shown in Figure 6.11. From the resulting surface coverage values obtained from SECM approach curves, the same process of fitting both Langmuir and Frumkin isotherms described in Chapter 4, was carried out. Plotting $1/\theta$ vs. 1/c gave K_L= (4.20 ±0.15)x 10^3 M^{-1} and $\ln\frac{\theta}{c(1-\theta)}$ vs. θ gave K_F=(3.00± 0.10) x 10^3 M^{-1}. There was again a reasonable agreement between the two isotherms. Due to the small value for the lateral parameter surfactant adsorption assuming a Frumkin isotherm, the system was thought to exhibit a Langmuirian behaviour. The model proposed in Figure 6.11 assumes a uniformly reactive interface, i.e. that spatial variations in reactivity between active and inactive sites occur on a length scale small compared to that of the SECM measurement.

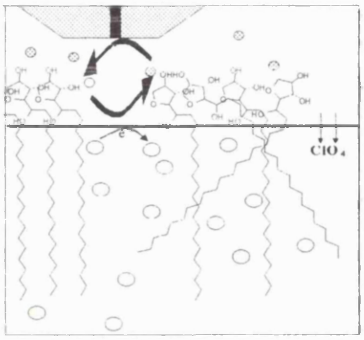

Figure 6. 11 Proposed schematic (not in scale) for interfacial ET studied with SECM

The validity of this assumption will be shown in the last chapter where the resulting isotherm (*θ-c*) of the SECM analysis will be compared to classical surface tension and capacitance isotherms. The cyclic voltammograms in Figure 6.9 suggest that in the presence of surfactant SM but with surface coverage not complete, the geometry of the ET process appeared to be dependent on the direction of ET. The forward peak in the presence of high surfactant concentration has a form characteristic of an array of microelectrodes sufficiently spaced that the diffusion fields do not overlap. The voltammograms were further analysed in order to demonstrate the effect of the different SM concentrations on the peak separation ΔE at 10 mV/s. Figure 6.12 shows the differential variation $|\Delta E_p - \Delta E_{ps}|$ of the potential differences between oxidation and reduction peaks, in the absence and presence of surfactant.

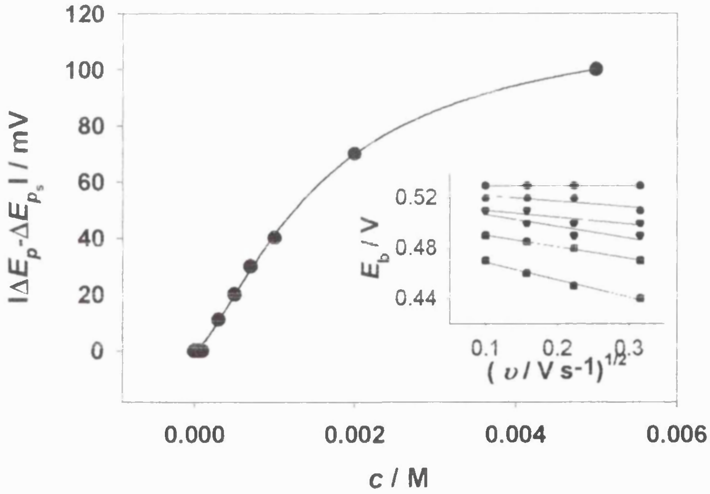

Figure 6. 12 The variation of differential variation (ΔE_p-ΔE_{ps}) of the peak potential differences in the presence and absence of surfactant against different surfactant concentrations. Inset shows the variation of the reduction peak potential, E_b, with scan rate at different surfactant concentrations, from top to bottom: 0, 0.5, 0.7, 1, 2, 5 mM.

It is obvious that the peak potential separation becomes larger as the fractional coverage increases. The inset shows the variation of the reduction peak potential, E_b, with scan rate at different surfactant concentrations, establishing the increasing irreversible character of the process. Figure 6.13 shows the variation of the peak height, I_f, of the oxidation peak potential with scan rate. The variation of peak position and peak height with scan rate was to some degree dependent on the reliability of the compensation for the effects of solution resistance between reference electrode tip and interface, and the scaling of the peak height also introduces an error.

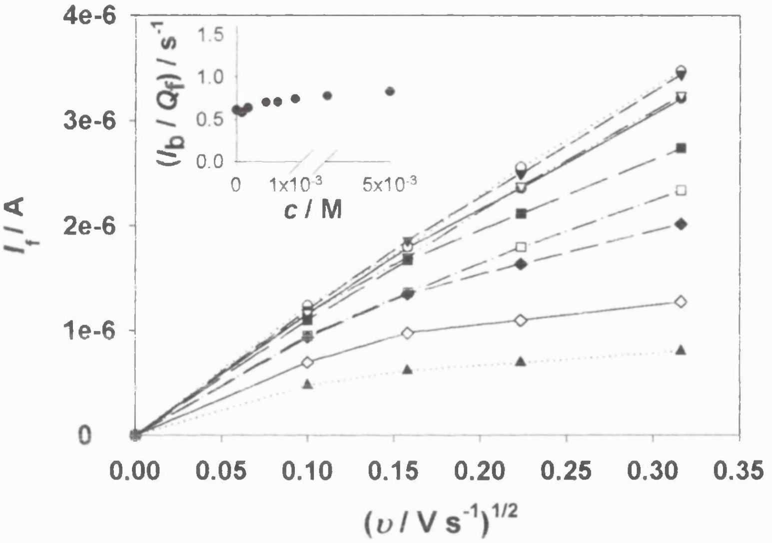

Figure 6. 13 The variation of the peak height, I_f, of the oxidation peak potential with scan rate, from top to bottom 0, 0.05, 0.1, 0.2, 0.5, 0.7, 1, 2, and 5 mM. In the inset the reduction peak height, I_b, at the highest scan rate, corrected for the capacitive current and scaled by the charge Q_f passed in the preceding oxidation wave.

Two factors are evident in Figures 6.12 and 6.13: firstly that there was an effect of change in the double layer potential caused by surfactant adsorption, which shifted the reduction peak potential even at low scan rates. Secondly, significant effects of surfactant coverage on the rate of the reduction of $DiMFc^+$ were actually very small and evident only at high surfactant coverage. The main effect of the surfactant was on the rate of oxidation of the uncharged DiMFc, where the ET in the absence of surfactant was a reversible process. The apparent geometry of diffusion of the neutral DiMFc and the charged $DiMFc^+$ became different as surfactant covers the surface. $DiMFc^+$ continues to access the entire surface as the surface coverage increases, with only a relatively slight decline in the rate constant.

In this respect, the behaviour of DiMFc$^+$ parallels the behaviour of other ionic species: ion transfer was not much inhibited by adsorbed surfactants, apart from the effects of change in the double layer potential.

The theory of ET at a partially covered electrode based on a model by Amatore *et al.*, proposed for blocked electrode interfaces, can therefore be applied[159] for the oxidation of the uncharged species (forward peak). It appears that the surfactant adsorbed at the interface creates microholes through which the reacting species, the large organic molecule, must diffuse through in order to react at the interface, resulting in a response analogous to that of a microelectrode array. With increasing surfactant coverage, the holes become smaller, less numerous and more widely spaced, resulting in the characteristic plateau response of an array of microelectrodes whose diffusion fields do not overlap. From the fractional coverage of surfactant patches and the limiting oxidation current of the voltammogram, i_{lim}, an estimate of the hole size and spacing can be obtained using the following equation given by Amatore *et al.* [159]:

$$i_{\lim} = \frac{FSc^o D(1-\theta)^{1/2}}{0.6R_o} \qquad \textbf{(6.11)}$$

where S is the total surface area of the interface, F is the Faraday constant,

c^0 is the bulk concentration of the redox species,

D is the diffusion coefficient of the redox species,

R_o is the radial distance between the active holes of radius $R_a = R_o(1-\theta)^{1/2}$.

With $\theta = 0.98$, from the limiting oxidation current of the voltammogram, with i_{lim} obtained at 10 mV/s, the distance between the holes was estimated to be $R_o = 20$ μm, and the hole diameter ca. 200 nm. It was speculated that the surfactant layer blocks the diffusion of neutral DiMFc but cannot block the diffusion of charged DiMFc$^+$ species because the layer was disrupted by the charge, perhaps as a consequence of the image forces induced across the interface as the charged species approaches.

For quasi-reversible behaviour, as shown for the reduction of the charged species, it was suggested by Amatore, that under certain conditions and for θ<1, in the case of blocked electrodes that it was only the rate that decreases by partial blocking. Therefore the voltammograms obtained were similar to those obtained with an unblocked electrode of the same surface area. In the inset of Figure 6.13 the reduction peak height, I_b, at the highest scan rate, is shown, corrected for the capacitive current and scaled by the charge passed in the preceding oxidation wave, Q_f. The latter compensates for the decrease, with increasing surfactant coverage, in the amount of DiMFc that was oxidised during the forward scan, depending on the available area. It is shown that the normalised current depending on the available area remains constant with concentration. Therefore, this aspect of the behaviour also mimics that expected from a simple partially blocked electrode.

6.5 Conclusions

- The presence of surfactant in respective phases did not affect the individual electrochemical processes, ensuring that any effect observed on interfacial processes was due to the presence of the surfactant at the interface
- The presence of the surfactants at the ionically polarisable interface inhibited the interfacial rate constant. The effect of Triton X-100 on ET was studied with MEMED and that of SM on ET with SECM.
- For both surfactants a patch model was proposed with ET occurring only at the interface that remains uncovered. A Langmuirian adsorption behaviour was suggested for both surfactants and it is suggested that the organic soluble SM blocks interfacial ET more efficiently than the aqueous Triton X-100.
- The four-electrode results complimented the SECM findings and the presence of surfactants at the liquid/liquid interface also decreased the rate of ET.
- The analysis of the voltammograms revealed an asymmetry for the geometry of the interface due to the presence of SM at the liquid/liquid interface with microholes of estimated diameter *d*=200 nm, and a response that was dependent on the species charge.

Chapter 7 GOx adsorption at interfaces

7.1 Introduction

The adsorption of proteins at liquid/liquid interfaces has already been reported in the literature. Paul *et al.*[160] and Strutwolf *et al.*[155] studied the co-adsorption of protein and lipids at the liquid/liquid interface. Hickel *et al.*[161] investigated the ranges of time, solvents and pH where hydroxynitrile lyase denatured, using interfacial tension results with the pendant drop technique. It has been argued by Ismond *et al.*[162] that some globular proteins, despite conformational limitations, have the capacity to self-associate into a micellar-like clusters under certain environmental conditions. They argued that in order for a protein to form micelle formation, it should have a specific intramolecular balance of hydrophobic and hydrophilic residues. Gajraj *et al.*[163] studied the absorption of lysozyme (Lys) and bovine serum albumin (BSA) with total internal reflection fluorescence microscopy. They argued that "soft" proteins such as BSA are quite hydrophobic with limited conformational stability on adsorption and may adsorb onto any surface regardless of charge, relating the concentration where breaks appeared in their physical properties measurements to CMC. In contrast, "hard" proteins like Lys, are less hydrophobic, therefore they experience little or no structural change on adsorption and tend to adsorb to surfaces having a charge opposite to the net charge on the protein. In this case there were no breaks observed in the physical properties following lysozyme adsorption[163].

Vanysek *et al.*[164,165] were the first to study the adsorption of proteins using ac-impedance at different pH and temperatures. They observed that the adsorption of BSA at the liquid/liquid interface exhibited some very interesting characteristics. With increasing concentration, the capacitance decreased, exhibiting a minimum at a concentration of ca. 10 ppm, whereas for higher concentration capacitance increased again, followed by another minimum at 50 ppm.

The enzyme used throughout this study was GOx. GOx is an enzyme that has attracted immense interest, due to its applicability in biosensors[166] for the determination of glucose in body fluids, as well as for removing glucose and oxygen from beverages and food products. It is a dimeric globular glycoprotein of dimensions 60x52x77 Å, made up from two identical sub-units, each of molecular weight circa 77000 Da, which are tightly bound with disulfide bridges[167] and hydrogen bonds. Sun *et al.*[168] showed that the observed surface area per enzyme molecule at the water/air interface varied from 700 to 2200 Å, depending on the conditions of spreading the enzyme in the subphase, whereas Fiol[169] based on the dimensions given above by Hecht estimated an area for the dimer of 3900±800 $Å^2$/molecule.

The mean diameter of the native enzyme according to photon correlation spectroscopy data is 76 Å at pH 7.4[170], in solution. The same group gives a Stokes radius for the molecule to be 43 Å with a frictional ratio of 1.21, from which they conclude that the enzyme is an elongated protein with rigid structure. In aqueous solutions each monomer is a compact spheroid of dimensions 60x52x37 Å[167]. GOx consists of various aminoacids of known sequence[171], and a redox coenzyme, flavin adenine dinucleotide (FAD) per monomer. The FAD is not covalently bound to the protein and can be released under denaturing conditions. The native protein is acidic with an isoelectric point of 4.44, while at pH 7 it is negatively charged with 11 charges. The holoenzyme has a diffusion coefficient of 4.94×10^{-7} $cm^2 s^{-1}$ in 0.1 M NaCl and a considerable part of hydrophobic side-chains located near the surface[172].

GOx adsorption at the liquid/liquid interface is presented in this chapter with capacitance and surface tension. The resulting adsorption isotherm and surface excess are discussed in conjunction with surface tension results obtained at the water/air interface. Neutron reflection measurements were also carried out for the GOx adsorption at the water/air interface, in order to estimate the thickness of the enzyme layer and the extent of immersion.

7.2 Impedance results for GOx adsorption at liquid/liquid interface

The effect of increasing GOx concentrations on the double layer capacitance was studied with two different cells. The two cells differed both in the nature of the cation and the ionic strength of the organic phase.

Cell 1a:	*Ag/AgCl*	**(wro)** 0.01 M LiCl 0.001 M BTPPACl	**(o)** ***Pt*** 0.001 M BTPPATPB	***Pt*** **(w)** 0.1 M KH_2PO_4 0.1 M K_2HPO_4 x nM GOx	*Ag/AgCl*
Cell 1c:	*Ag/AgCl*	**(wro)** 0.01 M TBuACl	**(o)** ***Pt*** 0.01M TBuATPB	***Pt*** **(w)** 0.1 M KH_2PO_4 0.1 M K_2HPO_4 x nM GOx	*Ag/AgCl*

7.2.i GOx adsorption with time

Figure 7.1 depicts typical cyclic voltammograms obtained with cell 1c, in the presence of increasing GOx concentration.

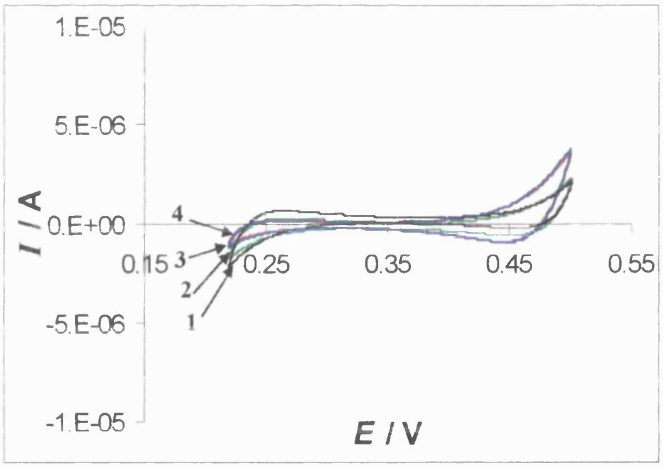

Figure 7. 1 Effect of GOx on the base potential window (black line 1), using various enzyme concentrations with cell 1c: 100 nM (green line 2),400 nM (red line 3) 1000 nM (blue line 4). A= 28 mm^2, υ=25 mV s^{-1}.

Figure 7.1 establishes that within the potential window studied, no potential window edge shifts were observed. In contrast, Vanysek *et al.* reported window edge shifts following BSA adsorption[165]. This suggests that GOx adsorption in this case does not induce or participate in any charge transfer process. Therefore the impedance measurements should reflect the change in the interfacial capacitance due to the interfacial enzyme film established. Furthermore, in this case there was no visible indication of contact denaturation, in contrast to other observations of protein adsorption, where there was a visible film adsorbed at the interface[165].

A similar procedure as that described in chapter 4 was followed here. Impedance measurements were started with cell 1c after 1h of equilibration and the experiments took up to 4h. The potential range *E*= 0.25-0.45 V was scanned twice, with the impedance response found considerably time-invariant, especially for higher enzyme concentrations. This led to the assumption that sufficient time was ensured for the establishment of adsorption equilibrium. The complex plane diagrams obtained, shown in Figure 7.2, were fitted using the equivalent circuit shown in the inset.

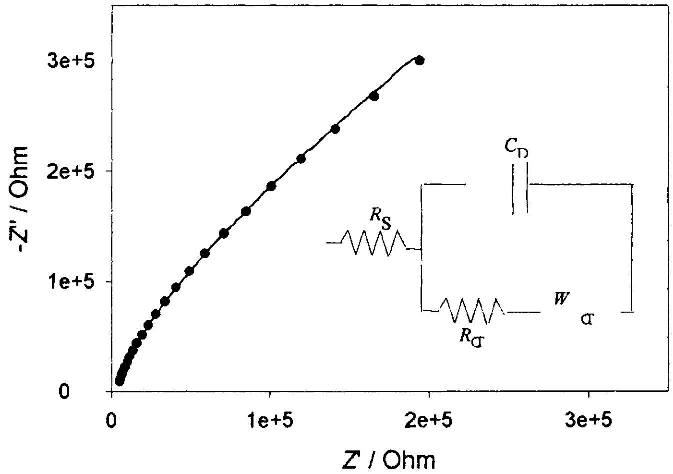

Figure 7. 2 Complex plane impedance plot of Z" vs. Z' for *f*=0.1-10 Hz, experimental set-up as in cell 1a, E=360 mV, with 400 nM enzyme present. Experimental values are represented as points, solid line is the fit using the equivalent circuit shown shown in inset (R_{CT} not used here)

At potentials close to the limits of the window, charge transfer resistance was added in the circuit in series with the Warburg impedance. The fitting errors were less than 2%, indicating a good fit without the inclusion of an adsorption impedance element in the equivalent circuit. The derived capacitance values from the responses at different potentials and in the presence of various GOx concentrations are shown in Figure 7.3.

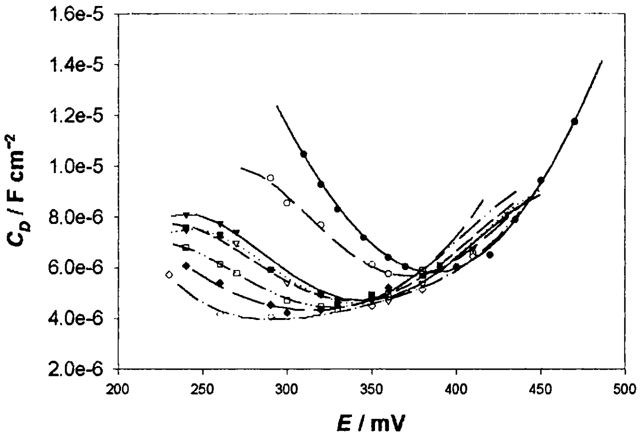

Figure 7. 3 Capacitance curves extrapolated from data as in Figure 7.2 with potential, with increasing GOx concentrations, using the four electrode cell (see text). From top to bottom 0, 50, 100 150, 200, 300, 400, 500 nM.

For all enzyme concentrations studied, C_D was lowered for potentials negative to E=350 mV and the minimum of the curves was displaced to increasingly more negative potentials. This minimum denoted the potential of zero charge E_{pzc}. For potentials higher than 350 mV the capacitance responses were either coinciding or higher than the capacitance curve of the base electrolyte. At even more positive potentials E>400 mV the capacitance response decreased, indicating desorption of the enzyme. This was attributed to electrostatic repulsion as well as to the onset of base electrolyte ion transfer. At concentrations equal or higher than 600 nM, the capacitance values measured here were irreproducible, showing occasional shifts of E_{pzc} to more positive potentials and giving higher capacitance values than that observed for lower concentrations. The capacitance values at E_{pzc} from Figure 7.3 are plotted against bulk concentration in Figure 7.4:

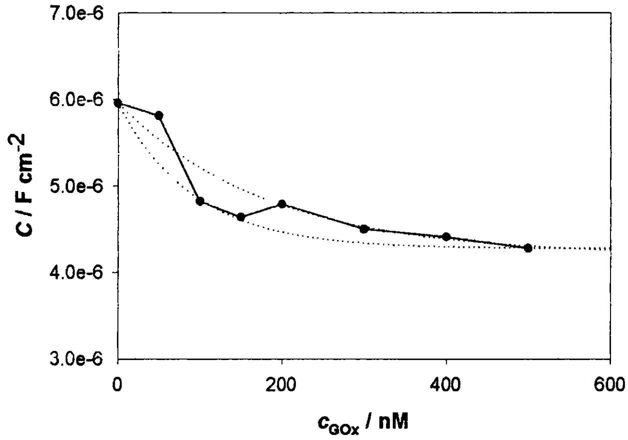

Figure 7. 4 Effect of enzyme on the interfacial capacitance at the pzc with cell 1c. Points and solid line: experimental points, Dashed lines: exponential decay for two different ranges

Figure 7.4 shows an overall decrease of the capacitance response with an initial minimum at 100 nM and a saturation point at 500 nM. It appears from figure 7.4 that the adsorption of GOx at the liquid/liquid interface is governed by two different processes and that the system switches from one adsorbed state to another with increasing enzyme concentration. In order to clarify this matter further a more detailed kinetic study was undertaken.

The capacitance values as a function of time are shown in Figure 7.5 for two different enzyme concentrations, 50 nM and 400 nM with impedance measurements at a selected potential starting immediately after the formation of a new interface.

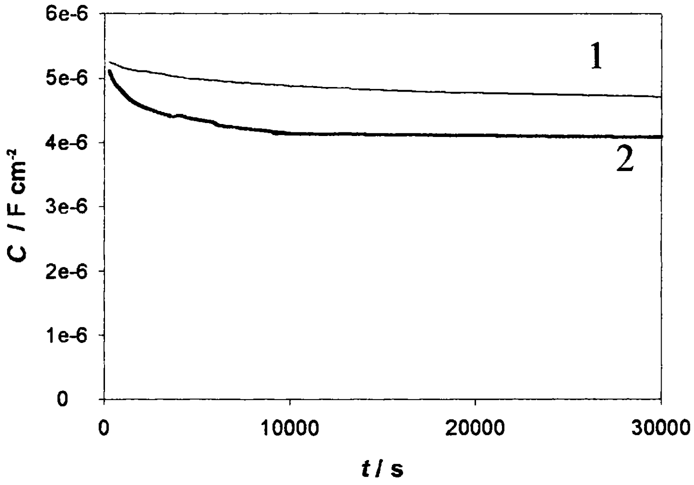

Figure 7. 5 Change of the double layer capacitance with time at E= 350 mV, for two different enzyme concentrations. (line 1): 50 nM, (line 2): 400 nM.

Figure 7.5 shows that the double layer capacitance for high concentrations reached a steady value within 3 h whereas for lower concentration 10 hours were required. It appears that the adsorption process at the liquid/liquid interface is slower than assumed earlier especially in the presence of low bulk concentrations. The long time and the slow process over which the enzyme adsorbed at the interface shown in Figure 7.5 accounted for the similar impedance response obtained as dc-potentials were scanned twice.

7.2.ii GOx adsorption in the presence of different electrolyte

There was an effect of the concentration and nature of cations present in the organic phase. Figure 7.6 shows typical voltammograms using cell 1a:

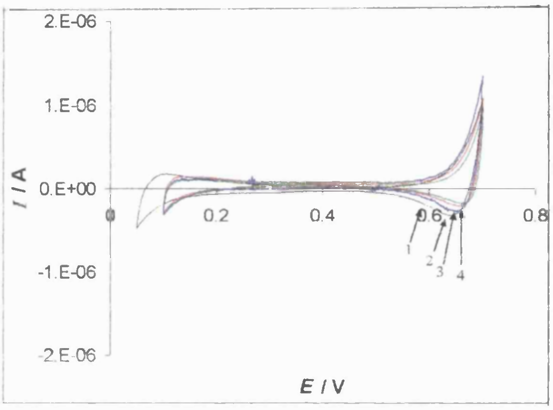

Figure 7. 6 Effect of GOx on the base potential window (black line 1), using various enzyme concentrations with cell 1a: 150 nM (green line 4),300 nM(red line 3) 1000 nM (blue line 2), A= 28 mm^2, υ=25mV/s.

The complex diagrams obtained for this cell following GOx adsorption were also fitted with the equivalent circuit shown in the inset of Figure 7.2. Figure 7.7 shows the resulting capacitance values obtained from two sets of experiments with cell 1a, after allowing the system to equilibrate for a shorter time (½ hour).

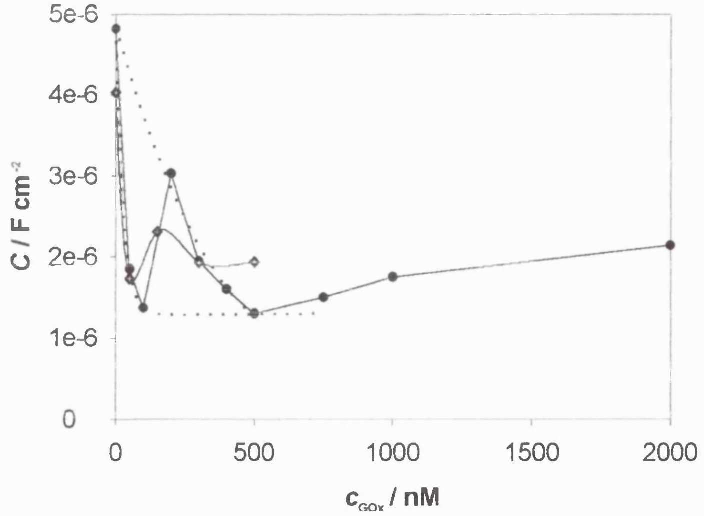

Figure 7. 7 Effect of enzyme adsorption on the interfacial capacitance at E_{pzc}=0.35 V with cell 1a. Circles & diamonds: two sets of experimental data, Dashed lines: Fits for two adsorbed states

As in Figure 7.4, Figure 7.7 shows that GOx adsorption lowered the C_{dl}, showing significant adsorption in the potential range negative to the E_{pzc}=350 mV. Although reproducibility within this time range was poor a first minimum appears in both cases at 50-100 nM, and a saturation point at 300-500 nM with a further increase in this case for higher concentrations. Again, a switch between two different adsorbed states is suggested with increasing concentration.

7.3 Surface tension results of GOx adsorption

A plot of surface tension, γ, against c and $\ln(c)$, where c is the bulk GOx concentration in H_2O, is shown in Figure 7.8. Initially surface tension was measured every half an hour, which revealed the dynamics of the adsorption process.

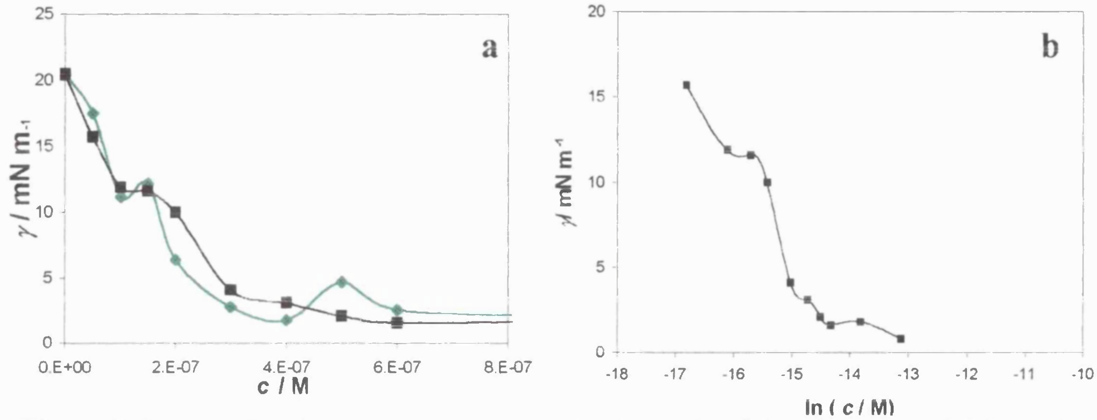

Figure 7. 8 a. Interfacial tension measurements for the study of the adsorption of GOx at the aqueous-organic interface, after 2 hours (diamonds) and 4 hours (squares) of equilibration. b. Plot of $\ln(c)$-γ after 4 hours of equilibration

Every GOx concentration lowered the surface tension of the uncovered liquid/liquid interface. Two minima were observed in Figure 7.8.a, at 100 nM and at 400 nM, and the adsorption process was found to be very time dependent. Figure 7.8.b shows several breaks in the surface tension curve and that γ did not level off within the concentration region studied. The effect of higher GOx concentrations (>1000nM) on the surface tension was not reproducible.

Figure 7.9, shows the plot of surface tension, γ, measured at the water/air interface with increasing bulk concentration of GOx in H_2O. The surface tension measurements were also dynamically monitored, and Figure 7.9.a shows the effect of GOx adsorption on surface tension with time. In this case a similar range of concentrations was used as in Figure 7.8 but two different aqueous ionic strengths were studied.

Figure 7.9.a shows two minima appearing in the surface tension measurements at 50 nM and 400 nM for the measurements within shorter periods (high ionic strength). After 14 h of equilibration there was a big change on the surface tension profile, with the second minimum observed at earlier measurements still apparent.

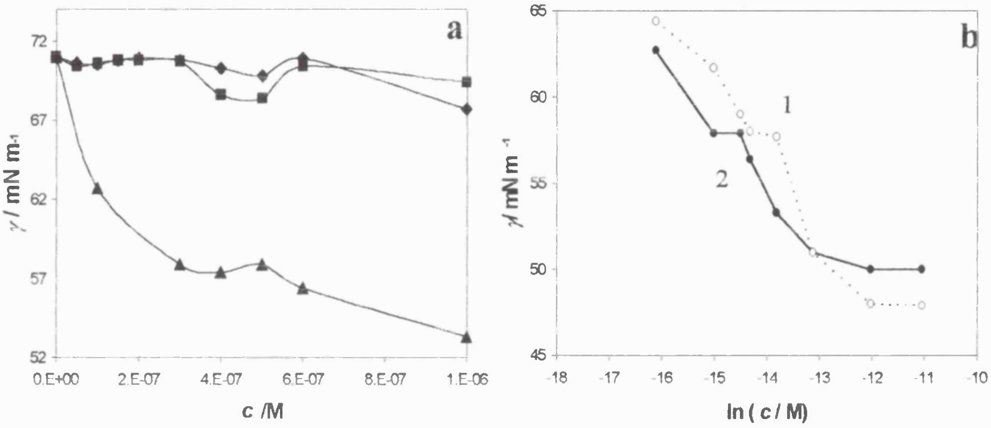

Figure 7. 9 a. Plot of γ vs. c for high ionic strength, after ½ h (diamonds) 2 h (squares) and 14 h(triangles) of equilibration. **b.** Surface tension lnγ–c measurements after 14 hours for equilibration of the adsorption of GOx at the water/air interface, at low ionic strength (dotted line 1) and high ionic strength (solid line 2), see text.

The adsorption process at the water/air interface was established as time, concentration and ionic strength dependent. The different minima and breaks of the surface tension plots in both cases also suggest that the adsorption of the enzyme involves various dynamic processes. Figure 7.9.b compares the curves obtained after 14 h for both ionic strengths studied. There is an apparent shift of the profile closer to the origin of the co-ordinates in the presence of high ionic strength. However, both curves have similar trends, particularly showing a break at around 500 nM and a levelling off of the surface tension at 6 μM. Assuming that the proposition put forward by Ismond *et al.*[162] is true, this concentration value could be tentatively suggested to be the concentration where GOx forms aggregates. During these measurements it was observed that for higher concentrations (>400 nM) as the ring approached the interface, it was repelled causing an extra decrease in surface tension of ~ 2-3 mN/m.

7.4 Neutron reflection for GOx adsorption at water/air interface

7.4.i Introduction

Structural parameters of the adsorbed layer can provide a better insight on the process of enzyme adsorption. These were obtained with neutron reflection measurements at the water/air interface. This is also a hydrophilic/hydrophobic interface, which is more easily studied with neutron reflection than the liquid/liquid interface, where it was assumed that the adsorption behaviour of the enzyme should be similar to the adsorption at the liquid/liquid interface.

It has been established that proteins exhibit surface activity, with uneven distribution of polar, non-polar and charged groups and adsorb spontaneously on a wide range of surfaces. For the water/air interface it has been found that proteins either simply expose their hydrophobic part, or change their conformation to selectively expose their hydrophobic moieties to the air phase, thus losing their tertiary structure[173]. Therefore the main thermodynamic force for protein adsorption should be the removal of non-polar amino acids side-chains, from their unfavourable aqueous environment. This process consisted of two different regimes, adsorption and conformational changes, and was dependant on many factors such as temperature, changes in protein conformational structure, protein-protein interactions and lateral molecular mobility within the layer[174]. In this case the water/air interface does not have an intrinsic charge, therefore there is no electrostatic interaction between the surface and the enzyme, but there are still electrostatic forces within the layer.

Calculations of area/molecule and surface excess were obtained from equation 2.20 based on the layer thickness and scattering length density obtained from the fit of simulated reflectivity profiles to the experimental data. The MW and total scattering length (17382,73 Å^2) of GOx were obtained based on the sequence and ligands of its crystal structure[167]. Two ionic strengths were also studied, a high one, I=0.2 M and a low one, I=0.002 M.

7.4.i Reflection in null reflecting water (low ionic strength)

Adsorbed layers were first studied at low ionic strength. The specular reflectivity obtained due to contrast with null reflecting water (NRW: $D_2O:H_2O\approx1:11$) was attributed solely to the adsorbed layer. The adsorption process, was also found extremely time-dependent, with typical time-scales needed to reach equilibrium for high concentrations (2000 nM) ca. 6 h and for low concentrations (10 nM) ca. 14 hours. The period needed for the system to reach equilibrium was based on the variation of the reflectivity at θ_0=1.5° with time, as shown in the inset of Figure 7.10, until no further variation in reflectivity response was observed. In Figure 7.10, the variation of the neutron reflectivity R is shown with increasing GOx concentration, in the form of log (R) versus momentum transfer Q.

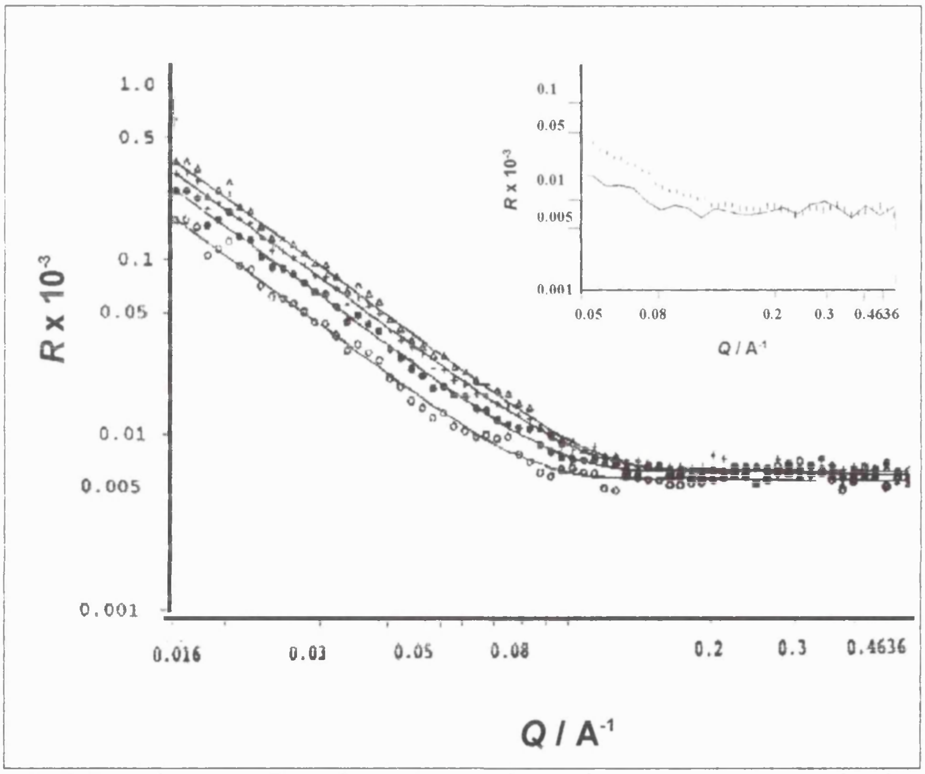

Figure 7. 10 Experimental reflectivity profiles for increasing enzyme concentration in NRW, from bottom to top bulk concentrations: 10, 100, 400 and 1000 nM of GOx in pH =7. The solid lines represent fits using the uniform layer model (see text). Inset shows the increase in reflection for 100 nM and θ_0=1.5°, after (solid line): 1h and (dashed line) 12h

Most of the variation in reflectivity occurred at values of Q below 0.1 Å^{-1} and above this all the curves fell to the level of flat background. The level of reflectivity was an indication of the surface coverage and its slope was related to the thickness of the adsorbed layer.

Quantitative information about the adsorbed layer structure was obtained by model fitting based on the optical matrix method outlined in Chapter 2. In this case, all GOx concentrations were fitted using a model of a single uniform layer with fits shown as continuous parallel lines in Figure 7.6. This indicates that the adsorbed layers are reasonably uniform, and therefore the adsorbed molecules probably retain their globular structure. From the fits of the single uniform layer model the layer's thickness τ and scattering density ρ can be obtained. From these fits the variation of surface excess and total thickness of the GOx layer with respect to the bulk enzyme concentration were obtained and are presented in Table 7.1.

Table 7.1 Structural parameters for the GOx layer adsorbed on the surface of water at I=0.002M

c / µM	τ±3 / Å	A / Å^2	Γ±0.20 mg dm^{-2}
0.01	38	12040	2.5
0.1	35	7200	4.1
1	40	5053	6.0

It was obvious that as the surface excess increased with concentration, the layer thickness remained reasonably constant. A preliminary attempt to follow the variation of adsorption with time, as shown in the inset of Figure 7.10 revealed in the case of 100 nM GOx, a change of layer thickness and area/molecule from 48 to 35 Å and from 10345 to 7200 Å^2 respectively, within 12 h. However, since time reproducibility was generally poor, all neutron experiments are subsequently restricted to equilibrium states, with results obtained after allowing sufficient time. The time effects observed here however suggested that GOx adsorption at the water/air interface was very time dependent with a rate of attainment of equilibrium was in broad agreement with results from other techniques in the literature.[175,176]

7.4.ii Effect of high ionic strength on GOx adsorption

In Figure 7.11, the variation of the neutron reflectivity is shown for the same range of concentrations as in the previous section, but for a higher ionic strength, i.e. 0.2 M of phosphate buffer. The time scale of the process this time was different, with low concentrations reaching equilibrium after at least 20h, whereas for high concentrations, equilibrium was reached within 5h. In this case, GOx adsorption exhibited different behaviour within different concentration ranges as shown in Figures 7.11.a and 7.11.b. The effect of adsorption in this case proved to be different than shown for low ionic strength in Figure 7.10.

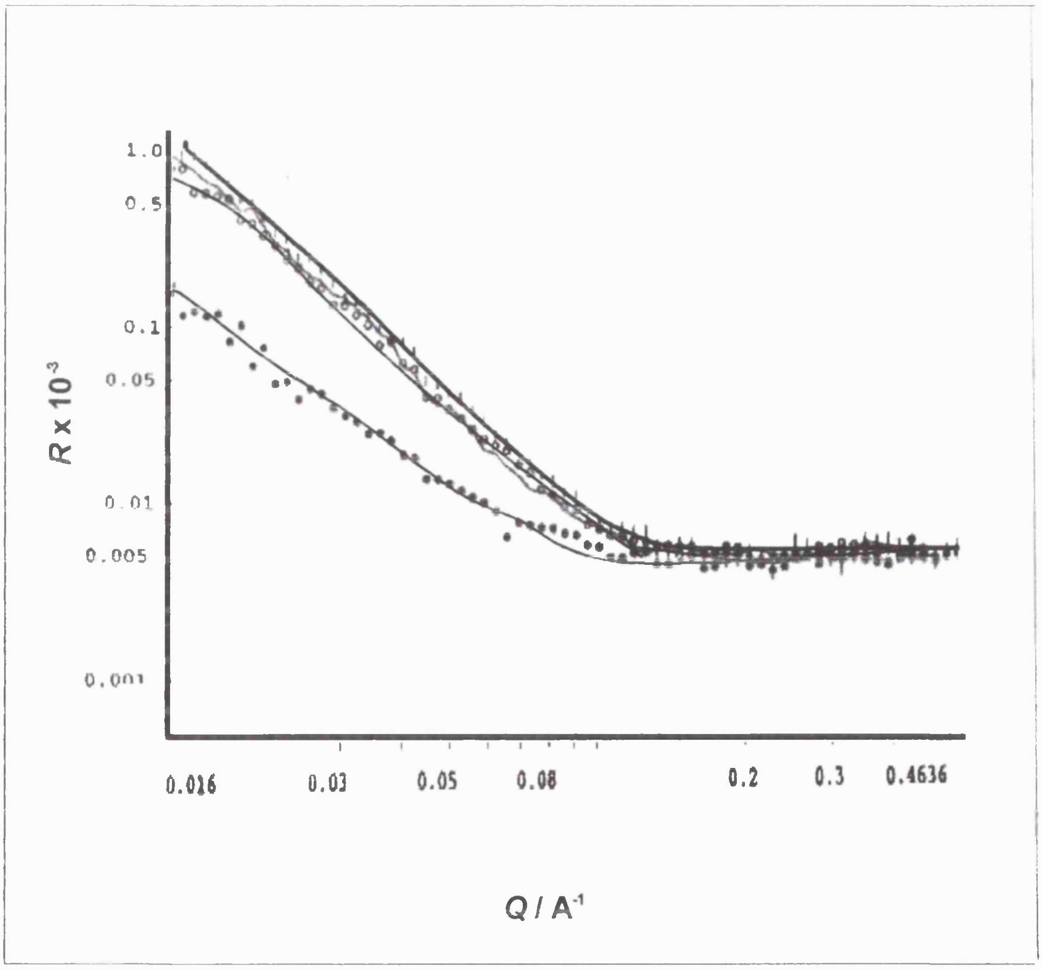

Figure 7. 11. a

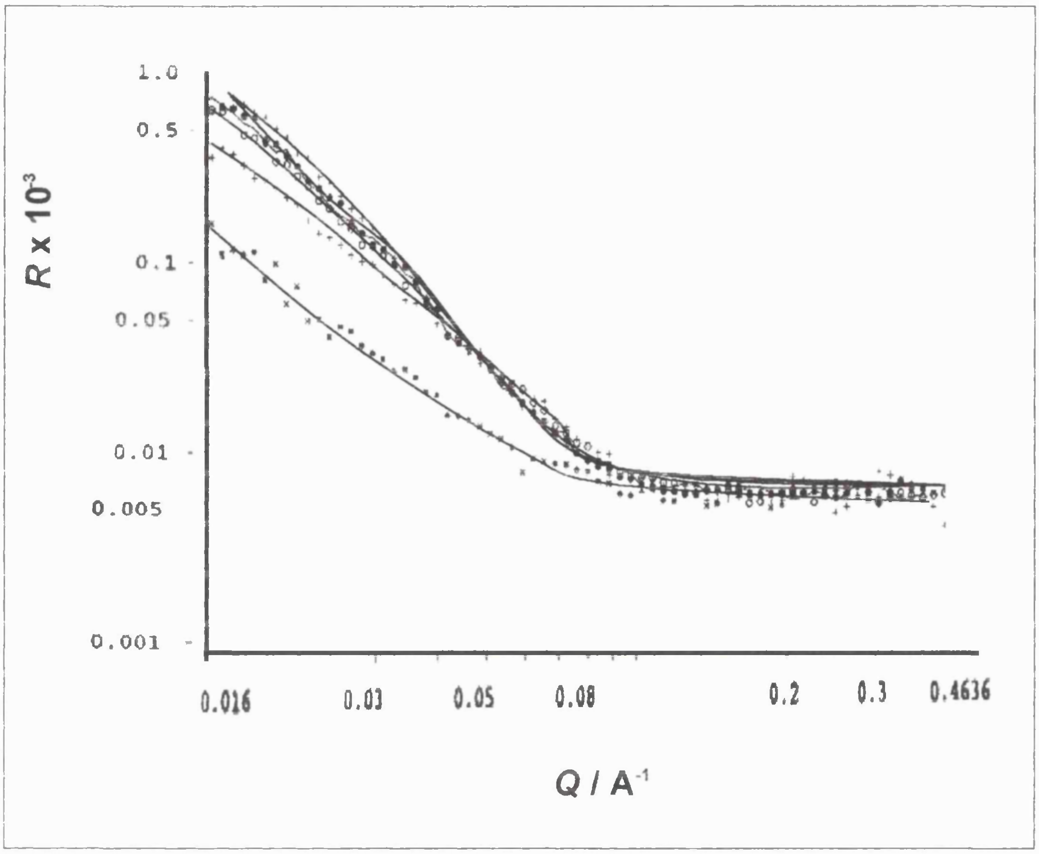

Figure 7. 11. b Experimental reflectivity profiles for increasing enzyme concentration in NRW, in high ionic buffer solution, a. from bottom to top bulk concentrations: 10, 100, 1000, 400 nM b. from bottom to top bulk concentrations: 10, 100, 1000, 2000, 6000 nM . The solid lines represent fits using the uniform layer model (see text).

Figure 7.11.a shows the range of concentrations from 10 nM to 1000 nM, at high ionic strength. It is shown that with increasing bulk concentration of GOx, there is an initial increase of the level of reflectivity, up to 400 nM. Meanwhile, the slope of the curves is different to the one observed in Figure 7.10. The reflectivity profiles shown in Figure 7.11.a decay faster, indicating that the thickness of the adsorbed layer was increased. Another interesting feature of Figure 7.11.a is that the magnitude of *R* rapidly increased in the range of low concentrations, i.e. from 10 nM to 30 nM, while remaining approximately constant for higher concentrations (*c*=100-400nM).

For concentrations higher than 400 nM, (1000 nM) the magnitude of the reflectivity profile, *R*, decreased whereas the slope continuously changed to become steeper for higher concentrations. In 7.11.b the response at 400 nM has not been re-plotted for clarity. There was a further subsequent increase on the magnitude of *R* profiles for higher concentrations. Following similar fitting procedures as described above the fitted solid lines of Figure 7.11 were obtained with the structural parameters, shown in Table 7.2. The profiles for the first range (Figure 7.11.a) of concentrations, fit a uniform layer with resulting thickness that initially increases with concentration, i.e. from 41 ±3 Å at 10 nM to 50 ±3 Å for concentrations 10-400 nM. For the second range of interest (>400 nM), the uniform layer was not an appropriate fit anymore. Instead, a two-layer model, incorporating a second layer beneath the main surface layer, was found to fit better the neutron reflectivity profiles. In fitting these two layers, the upper layer was taken to be similar to that obtained previously for the single uniform fit.

Table 7.2 Structural parameter for the GOx layer adsorbed on the surface of water at I=0.2 M

c / μM	τ_1±3 / Å	A_1/ Å^2	τ_2±3 / Å	A_2/ Å^2	Γ±0.20 mg m^{-2}
0.01	41	10870	-	-	2.75
0.1	50	5040	-	-	5.93
1	48	4895	55	31605	6.11
2	50	4760	56	31040	6.28
6	51	4426	57	20330	6.75

Although a two-layer model was used for this range of concentrations, no other possible fit of less ordered fragment distributions could be in accordance with the experimental profiles. This suggested that the protein does not denature and its globular framework does not break down to its peptide fragments, for all the ranges of concentration studied. Complete denaturation of the protein would result in a more complex structure at the interface, with various layers and different densities, as shown in the literature[177].

7.4.iii Extent of immersion of enzyme layer in water

Up to recently it was assumed that the monolayer formed by globular proteins at the water/air interface was fully immersed in water. It was however established that adsorbed molecules with distinct hydrophobic regions tend to expose a significant fraction of their molecules completely out of the underlying aqueous subphase[17]. Although in the case of globular proteins a distinct segregation between hydrophobic and hydrophilic parts does not exist, the molecule may sometimes gain some advantage by exposing some of the globular assembly to the air phase. The extent of immersion of the adsorbed layers at the water/air interface was obtained from experiments in pure D_2O, which was very sensitive in specifying the extent of mixing, in comparison with the results obtained previously in NRW.

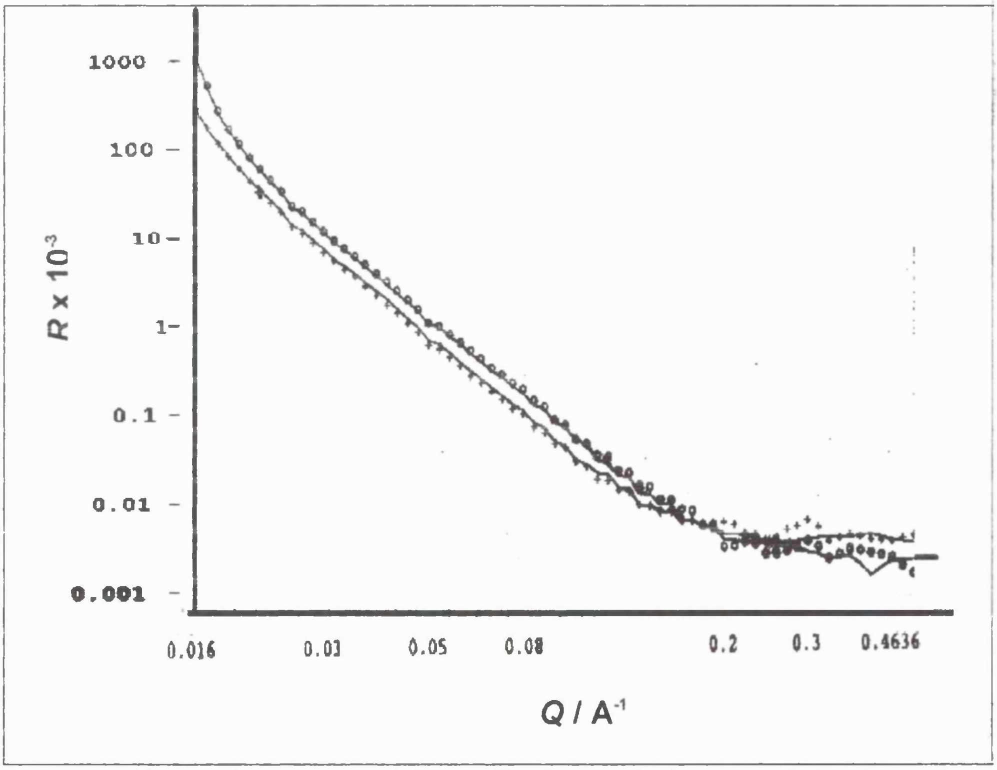

Figure 7. 12 Experimental reflectivity profiles from GOx layers on air/D_2O interface. Lower curves for 1 μm GOx bulk concentrations in (Points): I=0.2 M and (Line): I=0.002 M and upper curves for 0.01 μm GOx bulk concentration in (Points): I=0.002 M and (Line): I=0.2 M

In this case after allowing for the complete substitution of hydrogens by deuteriums at the immersed part, the specular reflection response was obtained from both regions above and below the interface but with different scattering length densities. At this point, the thickness and composition of the layers was already known from the experiments in NRW, shown above, therefore identical structural models may be applied to fit the D_2O data, allowing for the different scattering length density of the enzyme in heavy water to be accounted for. Figure 7.12 shows the reflectivities measured at two extreme concentrations, 10 nM and 1000 nM in D_2O, at high and low ionic strength values. It can be seen that the responses are quite similar for both ionic strengths. Since the reflectivity profiles recorded were measured at equilibrium, i.e. when there was no longer any change in the response, it was assumed that almost complete (>90%) exchange of labile protons with D^+ had taken place. For the non-equilibrated protons that exist at very hydrophobic areas of the enzyme, it was assumed that the contribution to the overall response was negligible.

7.5 Discussion

7.5.i Capacitance measurements

The shift of E_{pzc} for c<500 nM, shown in Figure 7.3, is attributed to increased adsorption of GOx as the water phase becomes more negative with respect to the organic. The excess of positive ions present on the organic side of the interface electrostatically attracts the negatively charged enzyme. This shift is combined with a lowering of capacitance at the negative branch of the curves only, indicating an assymetrical adsorption. The increase of capacitance values observed for the positive branch, was attributed to reorientation and partial desorption of the enzyme with the change of potential difference across the interface as proposed for phospholipids by Wandlowski *et al.* [144]. All capacitance curves in the presence of enzyme had a common intersection point at a critical value of 300 mV. This behaviour has also been observed for the adsorption of phospholipids and it was ascribed by Kakiuchi *et al.*[178] to a point of inflection on the adsorbed amount, suggesting that a non-equilibrium process occurs at the interface. The latter accounted for the variation of capacitance values, obtained within short time periods of equilibration (Figure 7.7). The results shown in figure 7.4 were obtained after longer times are thus not indicative of a complete equilibrium process either, especially for lower concentrations.

The change in the mode of concentration dependence of C_D vs. E in Figures 7.4 and 7.7 indicates the presence of two different adsorption states. These adsorbed states appeared to have different geometries at the interface, which accounted for the two minima of the capacitance curves. The apparent surface coverage of the interface due to the adsorption of the enzyme, was estimated from the curve presented in Figure 7.4 by assuming that at c_{GOx}=500 nM, where the capacitance values reproducibly levelled off, the enzyme is present only in state 2, that fully saturates the interface. The resulting apparent surface coverage was approached based on a model by Kakiuchi's[178] for phospholipid adsorption in two adsorbed states. In this case, the apparent surface coverage is calculated using equation 4.7, $\theta_{app} = \frac{C_D - C_D^{\theta=0}}{C_D^{\theta=1} - C_D^{\theta=0}}$, with $C_D{}^{\theta=0}$ and $C_D{}^{\theta=1}$ capacitance values in the absence and presence of a saturated monolayer at the interface, assuming one adsorption state present.

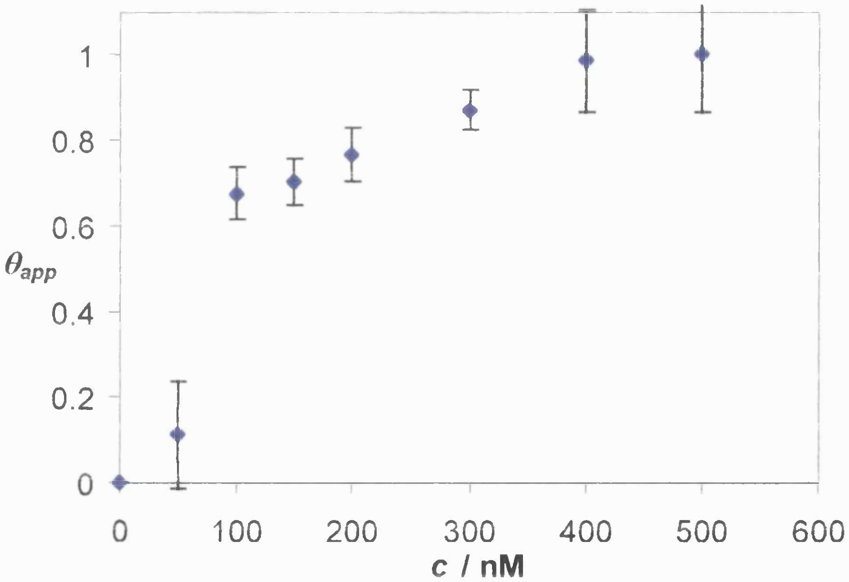

Figure 7. 13 Apparent surface coverage vs. enzyme concentrations, obtained from capacitance values at the E_{pzc}, assuming two states.

However, the apparent surface coverage observed here was similar to the one observed by Kakiuchi *et al.*, as it exhibited a break at a concentration of 150 nM, suggesting the presence of two states. For concentrations lower than 150 nM, the adsorbed molecules exist in adsorption state 1, with a fractional coverage of $\vartheta_1 = \frac{\Gamma_1}{\Gamma_{\mathrm{max},1}}$, whereas for c>150 nM, the molecules assume a second state 2, with $\vartheta_2 = \frac{\Gamma_2}{\Gamma_{\mathrm{max},2}}$, and the two states co-exist with a total fractional coverage of $\theta = \theta_1 + \theta_2$. $\Gamma_{\mathrm{max},a}$ is the maximum adsorption in either state. The apparent surface coverage of Figure 7.13, could not be therefore fitted by a Langmuir or Frumkin model, and there is insufficient data to treat the two regions separately.

The capacitance values for c>150 nM are therefore due to areas covered by state 1 and state 2 that are in parallel:

$$C_{D,obs} = C_{D,1} + C_{D,2} + C_{D,uncovered} \qquad \textbf{(7.1)}$$

so

$$C_{D,obs} = {}^1C_{D_1}^{(\theta_1=1)}\theta_1 + {}^2C_{D_1}^{(\theta_1=1)}\theta_2 + C_{{}_1D}^{(\theta_1=0)}(1-\theta_1-\theta_2) \qquad \textbf{(7.2)}$$

Although it was not able to extract any further information about the adsorption rates for either state, capacitance data established a model for the adsorption of enzyme that includes two different adsorption states.

7.5.ii Surface tension measurements

There have been many surface tension studies that have followed the changes of protein adsorption with time and concentration at the water/air interface [125-127]. During studies of GOx adsorption at both the liquid/liquid and liquid/air interfaces, the maximum decrease in surface tension was ca. 20 mN m^{-1}, in agreement with a value given in the literature[126]. Both surface tension studies exhibited multiple breaks, which strengthened the suggestion of different adsorption states based on the capacitance results. The surface tension results indicate a similar trend for the adsorption process at both interfaces, but for adsorption at the liquid/liquid interface the kinetics appear to be faster. Within a period of 2 h, there seems to be a decrease of 20 mN m^{-1} of surface tension at the water/oil interface, within a concentration range that resulted in an overall decrease of 2 mN m^{-1} at the water/air interface for the same period of time elapsed. The surface tension measurements at the liquid/liquid interface shown in Figure 7.9 were obtained after 4 h of equilibration, which was approximately the time needed for the completion of each capacitance measurement.

Assuming that the interface saturates at the second break of each curve the surface excess obtained from the slope prior to that, based on the Gibbs equation, gave area/molecule values of $A=1/\Gamma N_A$ =2500 Å^2 for the air/liquid interface and 3010 Å^2 for the liquid/liquid interface, both for high ionic strength. The estimated area per molecule from surface tension measurement correlated well with literature values by Sun *et al.* [168] (700 to 2200 Å^2) and Fiol *et al.* [169] (3900 ± 800 Å^2).

For the surface tension measurements at the water/air interface, shown in Figure 7.10 there is a difference observed between the different ionic strengths. For high ionic strength there was an increased enzyme adsorption, which could reasonably be attributed to reduced lateral electrostatic repulsion. Generally, the presence of a high concentration of buffer screens the charges of the adsorbed charged molecules, usually lowering the adsorbed area/molecule while increasing adsorption. It is suggested that the difference in the nature and the concentration of the electrolyte ions affect the structure of the interface, where the enzyme adsorbs.

7.5.iii Neutron reflection measurements

Figure 7.10 (low ionic strength) shows that with an increase of bulk enzyme concentration there was a steady increase of the magnitude of the reflectivity profiles, but no change in the shape or the slope as observed for high ionic strength in Figure 7.11. Therefore the increase in bulk concentration in this case resulted only in the increase of adsorbed amount with a similar layer thickness throughout the studied range. The adsorbed enzyme's physical state can be further explored by comparing the layer structure with the enzyme dimensions from the crystal structure (elongated dimer: 60x52x77 Å and compact monomer spheroid: 60x52x37 Å). Table 7.1 suggests that for low concentrations the enzyme adsorbs at the interface and then flattens out, to give a short thickness layer (38 Å) and a large area per molecule. At higher bulk concentrations, the adsorbed GOx molecules start to repel each other due to the charge of the enzyme at this pH, which combined with closer packing, prevents the molecules from flattening out. The layer thickness in this case increases slightly (40 Å), whereas the area per molecule decreases from 12040 to 5053 Å^2. The adsorbed enzyme molecules at high concentrations retain their global rigidity after adsorption due to intermolecular repulsion, with their y-axis (52 Å^2) normal to the interface, while x and z remain parallel to the interface. In this case the estimated surface area was 4630 Å^2 for sideways-on adsorption, which correlates well with the experimental value. As a first approach this could be attributed to the breaking of the disulphide bridges between the enzyme's monomers, followed by a monomer adsorption with their short axial z-axis 37 Å normal to the interface. This suggestion however was ruled out, as this process has not been cited following GOx adsorption and the large area per molecule obtained could not be accounted for: in the case of a monomer adsorption the expected A would be 3120 Å^2.

Table 7.2 showed that salt addition (high ionic strength) reduced the variation in surface excess obtained with increasing enzyme concentration, particularly for $c >$ 100 nM. A reasonable proposition is that at sufficiently high ionic strength, the electrostatic charges on the protein are screened, which increased adsorption whilst maintaining a reasonably constant layer thickness. In the case of high ionic strength, at very low concentrations (10 nM) similar suggestions can be put forward as above, where the enzyme adsorbs at the interface and flattens to give a layer of thickness of 41±3 Å and A=10870 Å^2. For higher concentrations (100 nM<c<400 nM), despite the substantial charge screening that takes place, local charges contribute to electrostatic interactions. Therefore the enzyme adsorbs at the interface while retaining its dimer structure, and molecules start repelling each other. The thickness of the closely packed layer established thus increased (50 ±3 Å) and was comparable to the short axial axis of the enzyme's globular dimer structure of 52 Å. This suggests that at this ionic strength, the enzyme adsorbs with both its long axes 60 or 77 Å parallel to the water/air interface. The resulting area/molecule (5038.5 Å^2) was also comparable to the estimated A for sideways-on adsorption of 4620 Å^2.

For even higher concentrations (c>1000 nM) another model was used to take into account a second layer of enzymes adsorbed underneath the first one established. The upper layer has a thickness of 50 ± 2 Å, consistent with the adsorption of the enzyme with the short axial axis of 52 Å normal to the interface. The lower layer had a thickness of 56 ± 2 Å. The upper layer was indeed similar in thickness to the single uniform layer obtained in the lower range of concentrations. The area/molecule corresponding to the packing of the layers also remained for the upper layer reasonably constant at 4893-4426 Å^2. In contrast, for the totally immersed second layer the area/molecule decreased from 31604 to 20330 Å^2. Table 7.2, shows that within this range the surface excess and the layer thickness remained reasonably stable over the whole of the high concentration range.

There were also some preliminary measurements on the extent of immersion of the layers described above in the aqueous subphase. It seems that there was not an apparent trend of the variation of the extent of immersion with respect to the ionic strength. The upper layer observed for high ionic strength was almost fully protruding out of water, whereas the second layer was immersed in water to a similar extent to that of the layer observed in low ionic strength. In both cases as the surface concentration increases the electrostatic repulsion between adjacent molecules would increase. This effect could be partly reduced by increasing the dielectric screening, i.e. by greater immersion in water. It appears that with increasing bulk concentration the extent of immersion of protein increases. For higher concentrations there was a second upper layer for the high ionic strength medium.

7.5.iv GOx adsorption model

Based on the collective findings of all the techniques used so far for GOx adsorption at a hydrophilic/hydrophobic interface the model illustrated in Figure 7.14 is proposed for the case of high ionic strength. It is suggested that the mechanism of enzyme adsorption involved different adsorption states that were concentration and time dependent. Capacitance minima and surface tension breaks over similar concentration ranges supported the neutron reflection findings. The model implies that at low concentration the initial adsorption of the enzyme at the interface is followed by conformational changes and reorientation of the adsorbed molecules that consequently flatten out (Figure 7.14).

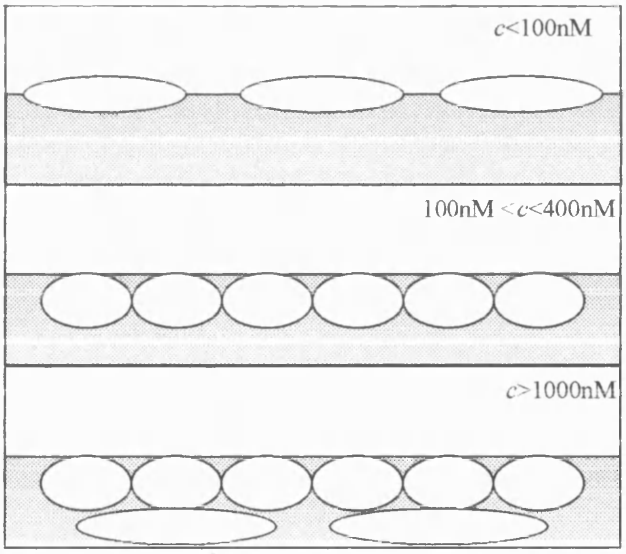

Figure 7. 14 Schematic representation of the change of the average surface coverage and conformation of GOx layers at the hydrophilic/hydrophobic interface.

At higher concentrations lateral interactions prevent the denaturation of the enzyme at the interface, which saturates quicker. For even higher concentrations a second layer of flattened molecules adsorb underneath the upper layer. This interfacial layer of increasing thickness therefore consists of bi-layers of adsorbed enzyme that interact with each other. Keeping in mind the size of the enzyme, the interfacial layer could be considered as a third phase forming at the interface with intermediate properties, that could account for the irreproducible results obtained with the surface tension and capacitance methods at the liquid/liquid interface.

This model could also account for the SHG findings of Rinuy *et al.*[179] on GOx adsorption at the water/air interface. The SH signal for GOx adsorbed at the water/air interface (high ionic strength) exhibited a shoulder at 100 nM and a maximum at 400 nM, subsequently decreasing for higher concentrations. At this point they noted that the onset of protein-protein interactions commenced, and they commented that this could be due to the dynamic nature of the process, involving rearrangement and re-orientation of the enzyme molecule at the interface. GOx adsorption was found to be very similar to BSA adsorption at the liquid/liquid interface[165]. From the neutron reflection results, it was also obvious that GOx adsorption at the water/air interface was very similar to BSA adsorption[130]. Based on these comparisons it is argued that GOx appears to be a "soft" protein with limited conformational stability on adsorption depending on concentration. It should be pointed out here that BSA adsorption at the water/air interface was also found to be remarkably similar to that at the hydrophilic silica/water interface[180] with respect to the model of adsorption, surface excess and layer thickness, despite the different nature of the interfaces. This conclusion strengthens the assumption made in this chapter that the water/air interface and liquid/liquid interface can be treated as similar.

The proposed model in Figure 7.14 could also give an insight into the interpretation of more detailed surface tension studies of adsorption of GOx at the water/air interface. The adsorption of GOx at the water/air interface, its penetration into lipid monolayers and possible kinetic regimes have been thoroughly studied by Rosilio *et al.*[125,175,181] Adsorption was found to be spontaneous but slow and enhanced in the presence of phospholipids. These authors proposed that the mechanism of GOx adsorption consists of three different steps or kinetic regimes:[127,175,176] an induction time to allow for the enzyme to diffuse to the interface, time for penetration of the enzyme at the adsorbed layer, and a mesoequilibrium regime, where the ***adsorbed molecules*** re-organises and re-arranges itself at the interface. Rosilio *et al.* found a maximum surface potential value established by a bulk concentration of 100 nM. At this concentration the authors believed that full surface coverage occurred following conformational changes. They also observed a maximum decrease in surface tension at a concentration of 5.5 μM of GOx concentration, without further considering the two different minima.

The preliminary dynamic experiments with every technique (especially Figure 7.5) presented in this chapter support the kinetic regimes described above, and correlate well with the model in Figure 7.14. Saturation of the interface initially occurs at lower concentration, following conformational changes (flattening out). For higher concentrations, as adsorbed enzymes molecules interact with each other they maintain their rigid conformation and the interface becomes saturated. The estimated values for area/molecule from the surface tension measurements are lower than the ones estimated ones the neutron measurement but within broad agreement with the literature values. It has been suggested that surface tension results should only be used qualitatively as the estimation of surface excess from semi-empirical equations has already led to various literature inconsistencies [130].

7.6 Conclusions

- The difference in electrolyte nature and concentration has a significant effect on the GOx adsorption at both the liquid/liquid and liquid/air interfaces.
- GOx adsorption involves at least two different adsorbed states, that are time and concentration dependent
- The dynamics of adsorption of GOx measured by interfacial impedance confirmed that there are three different, kinetic regimes: induction/diffusion, penetration and re- orientation/rearrangement
- The capacitance findings were further corroborated with surface tension measurements at the liquid/liquid and air/liquid interface
- Similarity of surface tension results strengthened the assumption of considering the liquid/liquid interface similar to the liquid/air interface.
- Structural parameters of the interfacial enzyme layer were provided by the neutron reflection technique, at the water/air interface. From these results it was concluded that at low concentrations for both ionic strengths studied, the enzyme adsorbed as flattened molecules exhibiting a greater degree of structural deformation, forming a layer of thickness 38 ±3 Å.
- For concentrations up to 400 nM, in high ionic strength medium, the enzyme retained its rigidity and adsorbed as a dimer with a layer thickness of 50 ±2 Å. For even higher concentrations, bi-layers of enzyme started to form, and the inter-layer interaction resulted in less densely packed layers, that caused a further decrease in reflectivity and capacitance.

Chapter 8: Interfacial electron transfer via adsorbed GOx

8.1 Introduction

In the previous chapters, studies of components used for a model of a biological membrane were presented. This included the adsorption of enzyme and surfactant at a liquid/liquid interface and the effect of the latter on interfacial electron transfer. This chapter presents a study with some of the components of a transmembrane electron transfer put together. Interfacial ET was established via an enzyme adsorbed at a surfactant modified interface, with the substrate in one phase and the mediator in the other. The reaction was studied using SECM:

Aqueous phase: Glusose + $GOX_{(FAD)} \rightarrow$ Gluconolactone + $GOX_{(FADH_2)}$
At the electrode: x-Med $\xrightarrow{Electrode}$ x-Med$^+$ (In the organic phase)
At the interface: x-Med$^+$ + $GOX_{(FADH2)} \rightarrow$ x-Med + $GOX_{(FAD)}$

As the electrode, immersed in the organic phase, approaches the interface from the organic side, the positive feedback current measured at the SECM tip indicated the occurrence of the interfacial enzyme-catalysed reaction and allowed the calculation of the rate constant.

8.2 Results

8.2.i Established protocol for enzyme system

The choice of appropriate components needed for an enzyme system that could be studied with SECM at the liquid/liquid interface proved very difficult. An extended number of organic electrolytes, potential determining ions as well as organic mediators were explored. Various combinations of the above included electrolytes and PDI such as BTPPATPB, TEATPB, TBuATPB, $TEAClO_4$, $TPrAClO_4$, and organic redox species such as ferrocene, decamethylferrocene and dimethylferrocene. Dimethylferrocene and the single electrolytes shown in Table 8.1 were found to be the most reliable components with reproducible results, a study of this enzyme system. Table 8.1 also presents the calculated equilibrium solution compositions established by the various SE used and the resulting interfacial potential:

Table 8.1: Calculated final concentrations of the potential determining ions after equilibration with C_{init}=0.010 M in either phase initially, and resultant interfacial potential differences $\Delta_{(o)}^{(w)}\phi_{eq}$.

Electrolyte	$C^{(w)}_{TAlkA+}$/M	$C^{(w)}_{ClO4-}$/M	$C^{(o)}_{TAlkA+}$/M	$C^{(o)}_{ClO4-}$/M	$\Delta_{(o)}^{(w)}\phi_{eq}$ /V
$TMAClO_4$	0.020	0.020	0.00049	0.00044	+0.005
$TEAClO_4$	0.019	0.019	0.00068	0.00064	-0.067
$TPrAClO_4$	0.016	0.015	0.005	0.004	-0.130

The choice of SE and resulting potentials was taken into account in conjunction with the potential value for ion transfer of $DiMFc^+$ occurring at $\Delta\phi$=−90mV. For this experiment the initial cell configuration used was as shown in the experimental section 3.3.ix. That required the "hook" electrode to be used which had the disadvantage of a very large glass sheath (RG=40). The pH chosen was ideal for the enzyme used to be mediated by an artificial mediator such as ferrocene derivatives.

8.2.ii Regeneration of DiMFc in the absence of enzyme

SECM measurements were carried out using cell 6a.

		(wro)	(o)	(w)
Cell 6a:	*Ag/AgCl*		*Pt* *Pt*	560 nM *GOX,*
		10 mM LiCl	1 mM DiMFc	0.05 M Glucose
		10 mM	10 mM $T(Alk)AClO_4$	0.2 M K_2HPO_4
		T(Alk)ACl		10 mM $T(Alk)ClO_4$
				0.25 mM Triton X-100

Initially blank measurements were carried out in the absence of key components of cell 6a. Typical responses in the absence of enzyme are given in Figure 8.1:

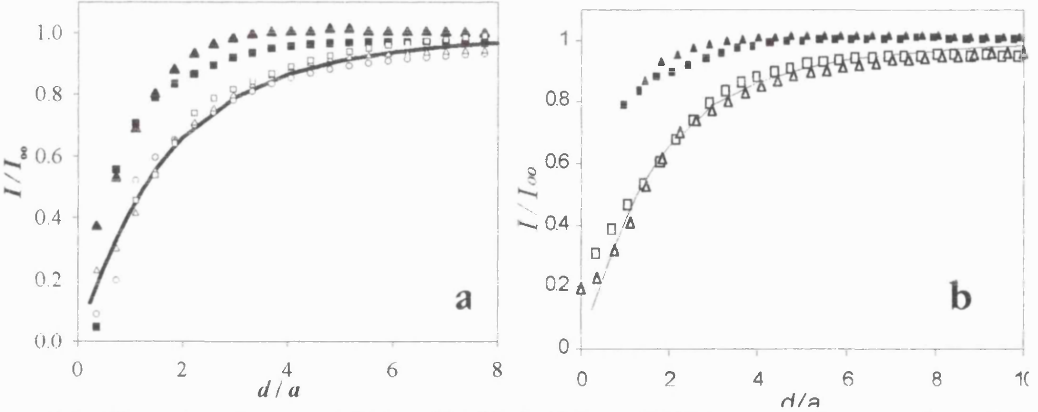

Figure 8.1 Effect of surfactants (a:Triton X-100, b: SM) on SECM approach curves for cell 6a in the absence of aqueous redox species. The electrode tip was held at +450 mV vs. Ag/AgCl in the reference junction, and approach rate is 4.6 μm/sec. (Filled symbols): absence of surfactants and (open symbols): presence of surfactants with PO_4 only (squares) and Glucose + PO_4 (triangles). *a*=12.5 μm. The solid line represents the theoretical behaviour for an insulating substrate.

Figure 8.1 shows the unexpected reaction of $DiMFc^+$ to DiMFc at the DCE/H_2O interface in the absence of any other redox species, in well-degassed and pre-equilibrated solutions. A similar process was observed even in the absence of glucose in the aqueous phase. There was no catalytic cycle involving oxidation of $DiMFc^+$ by glucose in the organic phase as saturation of the organic solvent with glucose, explored separately, had little to no effect on the diffusion limited current for DiMFc oxidation. Furthermore there was no indication from UV-Vis spectrophotometric analysis that DiMFc partitioned into the aqueous phase (see Appendix III). Furthermore when the tip touched the interface the current decreased instantaneously to zero due to the absence of redox species in the aqueous phase. When non-ionic surfactants (Triton X-100 in Figure 8.1.a and sorbitan monostearate in Figure 8.1.b) were added near the interface they blocked the DiMFc recycling reaction, resulting in a variation of current with distance that was in good agreement with the expected response for approach to an inert surface. Triton X-100 (aqueous soluble) gave more reproducible results and was preferred for further experiments. The unexpected regeneration after equilibrating the two phases of Cell 6a, in the absence of surfactant or enzyme, was also obtained with an electrode of RG=10, and a computer controlled approach speeds of 0.6 μm/s. This allowed a closer approach of the interface within 2 μm shown in Figure 8.2:

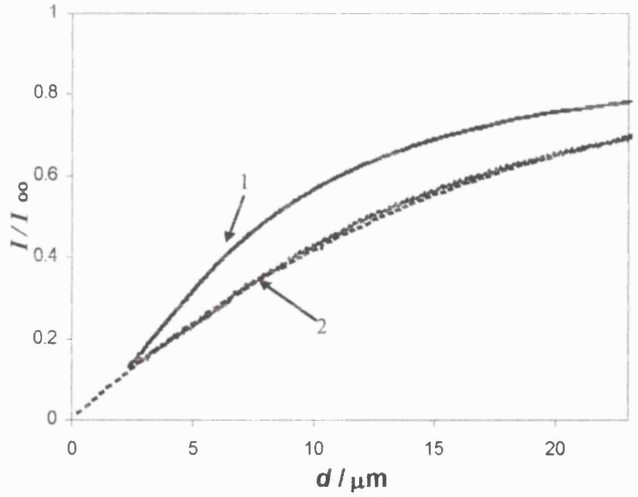

Figure 8.2 Same cell conditions as in Figure 8.1, with RG=10 and approach speed 0.6 μm s^{-1}. Non-negative feedback (solid line 1) response in absence of redox species, when the two phases have $\Delta\phi$=–0.067V established after equilibration, and (solid line 2) no equilibration, *a*=12.5 μm. (Dashed line): theoretical fit for insulator response

8.2.iii DiMFc regeneration by enzyme: Variations of $\Delta\phi$

Figure 8.3 shows the various SECM responses in the presence of the enzyme on the surfactant-modified interface. The enzyme was injected at the interface in microliter volumes, with no further stirring in the cell. In the absence of glucose the approach curve characteristic of an inert interface was obtained with both the surfactant and the enzyme present. In the presence of glucose the effect of the positive feedback current due to the enzyme reaction mediated by DiMFc$^+$ could clearly and reproducibly be seen.

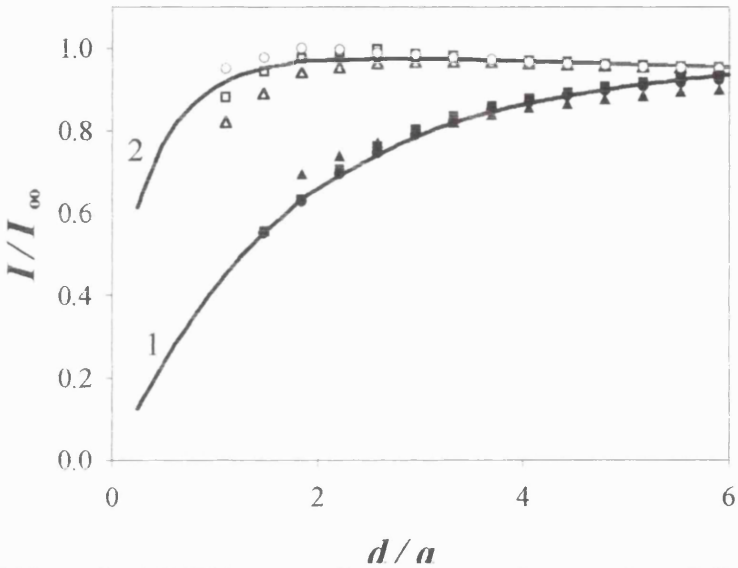

Figure 8. 3 Normalised SECM current-distance approach curves for cell 6b with similar conditions as in Fig. 8.8, with the different $\Delta\phi$ established by various SE: TMAClO$_4$(triangles), TEAClO$_4$(squares), TPrAClO$_4$(circles). Filled symbols in the absence of glucose and green symbols in the presence of glucose with the enzyme GOX and the surfactant Triton X-100. The solid lines represents the theoretical behaviour for an insulating substrate (solid line 2) and the feedback response (solid line 1) with a dimensionless rate constant K=0.3, a=12.5 μm.

The interfacial ET via the co-adsorbed enzyme could also be influenced by the electrochemical potential difference established. This was controlled by varying the ratio and nature of PDI distributed across the interface, shown in Table 8.1. There was not a big variance between the three potential differences established. The range of potentials chosen spanned the standard potential for DiMFc$^+$ transfer between DCE and water, and their effect was distinct but rather small.

8.2.iv Effect of degassing and surfactants

Figure 8.4 establishes the effect of degassing for the interfacial reaction using the enzyme system. In the absence of surfactant but in the presence of the enzyme, the feedback current due to the recycling of DiMFc$^+$ to DiMFc near the electrode increased further than already observed by the side-reaction, observed in Figure 8.1. This effect could only be observed if the aqueous solution was thoroughly degassed: if this was not the case, then the current enhancement in the presence of the enzyme was almost absent. In the absence of degassing, when the tip penetrated the interface there was a manifold increase of current due to the presence of H_2O_2 in the aqueous phase following the enzymatic reaction catalysed by O_2 present in solution.

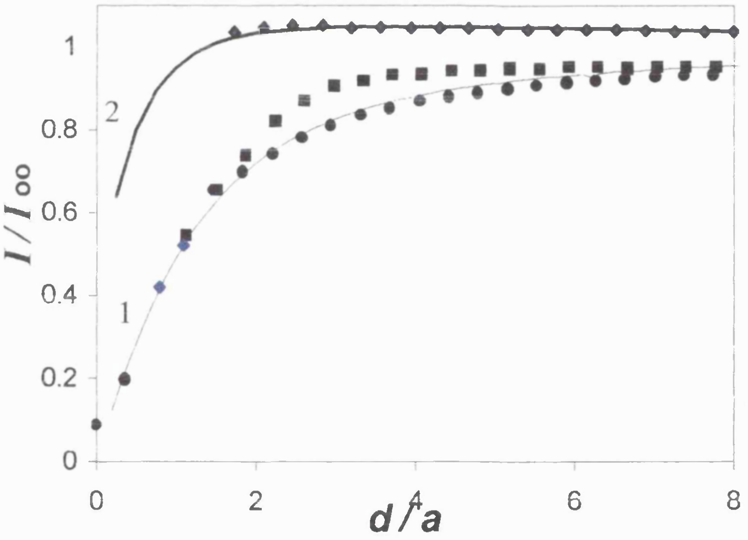

Figure 8. 4 Effect of degassing in the presence of GOx and absence of surfactant. Normalised SECM approach curves with conditions as in previous figure. Circles denote the response for 0.1 M PO_4, diamonds show the response with 0.05M Glucose+0.1 M PO_4 in the aqueous phase after adequate degassing for 30 min and squares when no degassing of the aqueous phase took place. The solid lines represent the theoretical behaviour for an insulating substrate (1)and K= 0.5 (2)

The effect of the nature of the different surfactants used was also studied briefly, using anionic sodium dodecyl sulfate (SDS) and cationic cetyltrimethylammonium toluene sulphonate (CTATS)[114]. The current enhancement due to the feedback current caused by the enzyme reaction mediated by DiMFc was closely similar for all the surfactants used as shown, in Figure 8.3.

8.2.v Effect of adsorption method and mediators

The interfacial enzyme reaction was also studied with the normal electrode of RG=10 and cell shown in Figure 3.12.b with the cell 6b:

	(o)	(w)
Cell 6b:	*Ag(QRE)* *Pt* 1 mM DiMFc 30 mM TPrATPB	0.05 M Glucose 0.2 M K_2HPO_4 10 mM TPrACl 550 nM *GOX,*

In this case, instead of the single electrolyte system used in cell 6a, $TPrA^+$ was used as a potential determining ion and the phases were not equilibrated. An experiment was carried out, where instead of the spread method for GOx adsorption, the enzyme was dissolved in the aqueous buffer solution, allowing sufficient time (>3h) for GOx to adsorb and fully saturate the interface, as established from the capacitance measurement for this concentration. The system was under continuous degassing, and the SECM approach curve from the organic phase to the interface is shown in Figure 8.5:

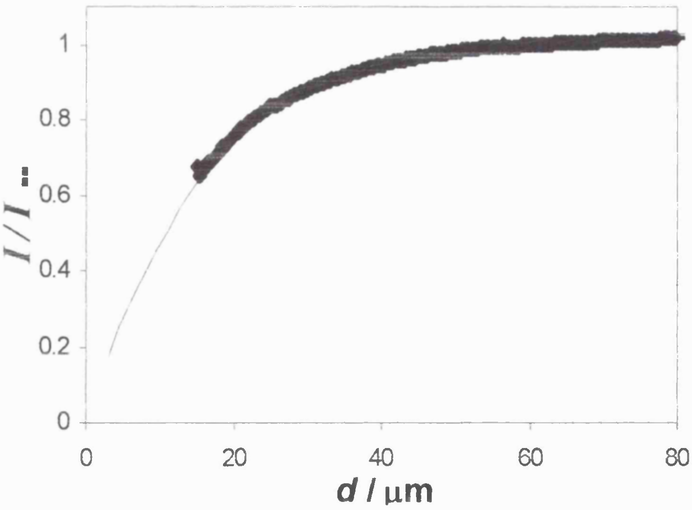

Figure 8. 5 Approach curve after 3h. of equilibration to allow monolayer formation from bulk GOx concentration of 500 nM with constant degassing, with $TPRA^+$ as a PDI. (line): theoretical fit for an insulator and (diamonds): experimental data for approach speed of 2 µm/s.

This experiment showed that even with careful and continuous degassing, the enzyme present only as an adsorbed monolayer, did not produce a significant feedback that could be detected with SECM. The behaviour contrasts with that observed when the enzyme was injected close to the interface, as presented in Figure 8.3.

Some preliminary experiments were also carried out with cell 6b in order to establish a system for the possible study of lateral electron transfer, using a co-adsorbed mediator at the interface. One of the mediators proposed was ubiquinone, UQ, in order to study the system schematically presented by:

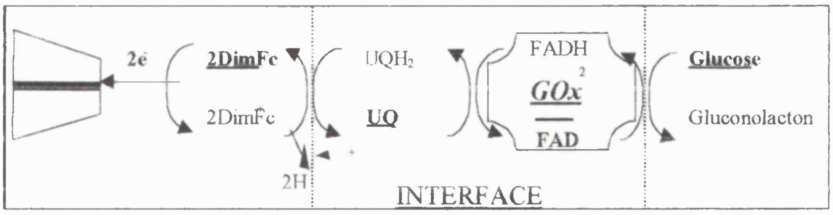

Additions of GOx and UQ were carried out again with the spread method of 1 µl GOx of stock solution near the aqueous side of interface and 10 µl of stock UQ near the organic side of the interface. For a well-degassed system the SECM curves obtained are presented in Figure 8.6:

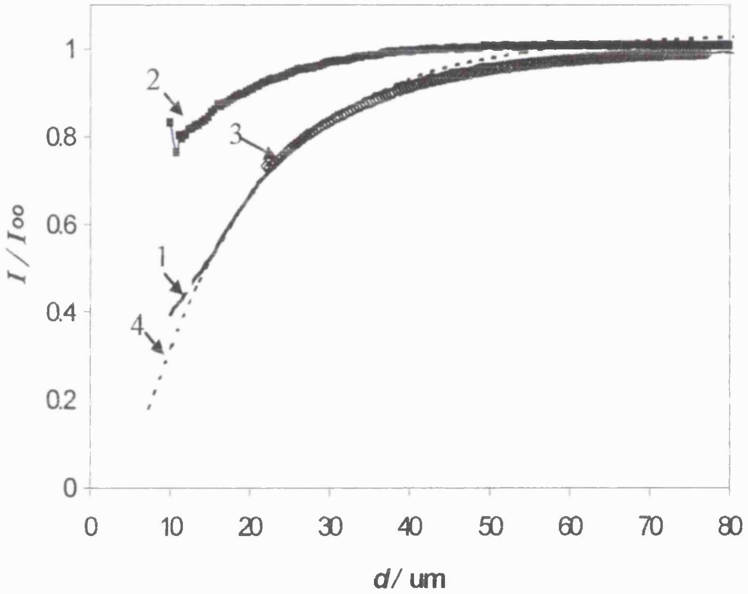

Figure 8. 6 Approach curves using cell 6c in the absence of GOx (solid line 1), after spreading 20 µM GOx (squares & line 2), on the aqueous side and 100 µM UQ (diamonds & line 3), on the organic side of interface. (Dashed line 4): theoretical fit for insulator response.

In the absence of GOx an insulator-like response was obtained. In the presence of GOx, the regeneration of DiMFc$^+$ takes place by the enzyme adsorbed interfacially and a positive feedback was measured, as shown in the previous sections. However, further addition of UQ reduced again the response to an insulator one. This suggests that either the presence of UQ at the interface blocks the reaction, or that the enzymatic regeneration was carried out by UQ instead of DiMFc$^+$. In this case the cycle was not completed as UQ could not be regenerated by DiMFc$^+$. Although in thermodynamic terms such regeneration should be possible, the expected coupling could not be measured. Possible future approaches are further discussed in chapter 9.

8.3 Discussion and proposed model

It was established in chapter 7 that adsorption of GOx at the liquid/liquid saturate the interface at estimated bulk concentrations of 400-500 nM where the enzyme retains its conformational rigidity. It is adsorbed with its short y-axis perpendicular to the interface and x and y parallel to the interface. Adsorption in this geometry would allow the active site pocket of the enzyme, situated in the middle of y-axis, to be accessible to both phases. The surfactant adsorption results established the concentration range of monolayer formation with pores, which inhibits interfacial ET. The enzyme concentration in this chapter was such that would ensure maximum coverage, and the surfactant concentration (just below CMC) ensures almost monolayer formation as found by MEMED measurements in chapter 6 and SECM[100]. It is proposed that according to studies of Rosilio *et al.*[175] for the penetration and co-adsorption of GOx with lipids at the water/air interface, a similar behaviour could be expected for the present system.

It was interesting to observe in Figure 8.1 that following equilibration of the two phases the regeneration of DiMFc was observed in the absence of aqueous redox species. The electromigration effects due to low concentration of the organic electrolyte were proposed as the reason for the unexpected behaviour that has to be accounted for. Another source of deviation could be the use of such a big RG (40 in this case) for the electrode or some other artefact of our system. The results shown in Figure 8.2 however establish that this behaviour was not related to an artefact of the system. It was therefore concluded that following the equilibration of the two phases the establishment of $\Delta\phi$=0.067 V allows for an interfacial process to take place. If the phases were not equilibrated (i.e. the potential difference was not at equilibrium value) the interface indeed behaved as an ideal insulator. The effect shown in Figure 8.2 was not as large as that observed for the electrode with RG=40 (Figure 8.1). Initially it was speculated that DiMFc would adsorb at the interface and participate in a self-exchange process as suggested by Wei *et al.*.[182] However there was no further independent evidence for this adsorption and as this process was not fully understood, it was instead completely blocked by the presence of surfactant at the interface. It could be argued that the mediation of the enzyme by the organic soluble mediator was due solely to the solubilisation of the DiMFc mediator in the aqueous solution with the aid of the neutral surfactant, as has been shown in other systems[183]. However this would not explain the positive feedback of the current response with only the enzyme present, exhibited in Figure 8.4. The surfactant in our case was introduced at the interface, to ensure that the background recycling process was prohibited and to prevent the enzyme from denaturing.

Therefore the response observed could be attributed to either an interfacial reaction between the adsorbed enzyme within the surfactant layer, or a possible coupled homogeneous reaction in the aqueous phase, following the transfer of the DiMFc$^+$ in the aqueous phase, shown in the simple schematic of Figure 8.7. An aim of this study was to address the question, which also arises in studies of bilayer lipid membranes: which of the two processes occurs?

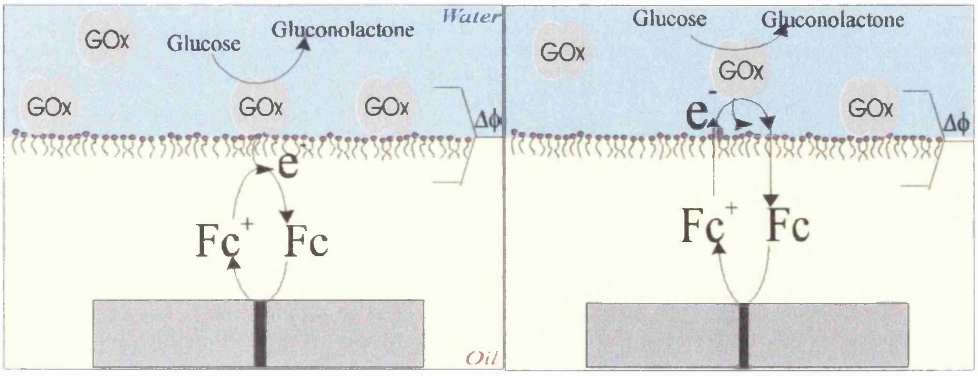

Figure 8. 7 Schematic diagram (not in scale) for the proposed models explored in the present system. Scheme a. shows an interfacial ET between the organic mediator produced at the tip and scheme b. shows IT of the mediator in the aqueous phase and subsequent homogeneous ET.

The first question then is to what extent the two processes depicted in Figure 8.7 could be distinguished by the measurements made here. An initial approach can be attempted based on the response at the various potential differences established. The standard potential of the FAD (redox active site) of the enzyme is E_{Red}^0=-0.136V (SHE) and for the DiMFc, E_{ox}^0=0.350V (SHE). Since E_{Ox}^0-E_{Red}^0 >>0, variation of the interfacial potential difference over the range studied might not have a large effect on the reaction rate if it were indeed an interfacial charge transfer. A range of values is quoted in the literature for the standard transfer potential of DiMFc$^+$ from water to DCE: $\Delta_{(o)}^{(w)}\phi_{DiMFc}^{IT}$=-0.090 to -0.148. Given this, the partition coefficient would be expected to vary between (0.3 to3)×10^{-2} with $TMAClO_4$ as partitioning electrolyte to (0.56 to 4.75) with $TPrAClO_4$.

A much larger effect than observed in Figure 8.3 would have been expected, if a homogeneous aqueous reaction following ion transfer across the interface were the only process occurring. The simulated positive feedback response shown in Figure 8.3 was calculated using a normalised rate first order rate constant of K=0.3. With a diffusion coefficient for DiMFc, $D = 2\times10^{-5}$cm^2/s and tip radius a=12.5μm the resulting first order rate constant was $k = 5\times10^{-3}$cm/s. Pierce *et al.*[184] studied the reactivity of GOx immobilised in a film adsorbed on several solid substrates. They developed models to derive the ET kinetics from the approach curves for such systems. The value obtained for a first order rate constant during the present work indeed lies within the range observed by Pierce *et al.* for enzyme immobilised on solid substrates. These authors found a better fit between their experiment and a model for zero order heterogeneous reaction, especially for low mediator concentration (50μM). The experimental curves shown in Figure 8.3 can equally well be described by a zero order reaction. Using the working curves presented by Pierce *et al.* the resulting rate constant, for a mediator concentration of 1mM, was $k = 10\times10^{-11}$mol cm^{-1}s^{-1}, a value which lies also in the range quoted by these authors.

If however the enzyme loading was reduced to a simple monolayer, a calculation of the expected feedback current enhancement using the known turnover rate of the enzyme in aqueous solution indicates that the feedback current should be very small. Indeed, it was shown here that if the enzyme molecules were restricted to a monolayer, no feedback current was seen. Therefore the first system studied here produced a significant feedback current due to the spreading technique that resulted in sufficiently high loading of the enzyme at the interface. Furthermore, GOx was not bound in this case to the interface, because the modified liquid/liquid interface provides a flexible substrate upon which GOx can adsorb and freely orientate. Finally at this pH, the enzyme's active site was slightly hydrophobic and negatively charged, which was an advantage for the hydrophobic mediator $DiMFc^+$ to approach it. The active site pocket could equally be reached by components in either phase, without the need of an extra step for the enzyme of flipping over at the interface. The use of the dispersion method was imperative which allowed the components to give a maximum adsorption avoiding the waiting period for equilibrium to be reached[185]. Using the method of equilibrium adsorption from solution, which restricted the enzyme coverage to a monolayer only gave an approach curve, which was, within experimental error, indistinguishable from the insulator's response, Figure 8.5.

Due to the limited amount of data and uncertainties in some measurements, it was not possible to decide which mechanism describes our data better, but it should be noted that the rate constants of either mechanism agree with those observed by Pierce *at al.* The slow heterogeneous kinetics could be attributed to interfacial/surface effects, as very little was known at the moment about the dependence of *k* on the interface structure or potential. The competition with oxygen dissolved in the aqueous phase, shown in Figure 8.5 should also be noted. This implies that the enzyme at the interface was certainly accessible to mediators present in the aqueous phase and was significant because, in the bulk solution, the reaction with dissolved oxygen was slower than that with ferrocenes. Because the effect of the interfacial potential was small, a reasonable conclusion is that the reaction was occurring within a thin film of interfacial layer of protein and surfactant.

8.4 Conclusions

❖ There was an unexpected reaction for $DiMFc^+$ for the enzyme system at the interface in the absence of aqueous redox species, after the two phases were equilibrated to establish the interfacial potential difference by the single electrolyte. The process was not clarified but instead was suppressed in the presence of surfactant.

❖ In the presence of surfactant, after carefully controlling the experimental conditions, the adsorption of the enzyme can result in the transfer of electrons from one phase to the other. This could give some insight to various transmembrane processes that occur in biological systems.

❖ Interfacial electron transfer via an enzyme can only be detected when the spread method was used for GOx adsorption and the system is thoroughly degassed, suggesting that a higher than monolayer coverage was established, with interfacial ET occurring within this interfacial layer.

❖ It was not clear with these measurements, if electron transfer occurs homogeneously or heterogeneously, but the rate constants observed suggest that interfacial ET was probable

❖ Co-adsorption of an interfacial mediator with the enzyme ought to allow the study of lateral electron transfer within the mediator/enzyme/surfactant layer.

Chapter 9. Conclusions & further work

9.1 Conclusions

This thesis has presented an attempt to build a system at the liquid/liquid interface that would represent a simplified model for the study of transmembrane proteins responsible for the electron transfer energy processes at the mitochondrial inner membrane. The system main components (surfactant and enzymes) were separately studied and characterised with a number of techniques, followed by the study of the surfactant effect on simple interfacial ET. Finally interfacial ET via an enzyme adsorbed at a surfactant-modified interface was achieved, thus establishing the approach to the biological system and providing some insight on how this experimental model might work.

9.1.i Effect of adsorption of SM at liquid/liquid interface

From the various surfactants used, the non-ionic ones, the sorbitan monostearate SM, and Triton X-100 were extensively studied, and both induced under certain conditions and potential ranges facilitated IT. The adsorption of SM at the liquid/liquid interface in particular was extensively studied with a number of techniques presented in Chapter 4: with impedance, and surface tension and in chapter 6: with CV and SECM. The effect of SM adsorption on the capacitance values, the surface excess and the kinetics of simple ET were fitted to both Langmuir and Frumkin isotherms. Table 9.1 presents a comparison of the various values obtained

Table 9.1 Values of adsorption coefficient obtained from isotherms by various techniques

	ST	SECM	Capacitance
Lanmguir, *K*	(2.20 ±0.01)x 10^3 M^{-1}	(4.20 ±0.15)x 10^3 M^{-1}	(5.50±0.05) x 10^3 M^{-1}
Frumkin, *K*	(2.60± 0.02)x 10^3 M^{-1}	(3.00± 0.10) x 10^3 M^{-1}	(5.00± 0.06)x 10^3 M^{-1}

A good correlation was obtained not only for the values obtained from different isotherms, but also from the various techniques used to extract them. From each individual analysis it was established that the lateral interaction parameter *a* obtained from Frumkin analysis was very small. Therefore a simple Langmuirian behaviour can be assumed for SM adsorption. Figure 9.1 shows the variation of surface coverage with concentration, obtained from these different techniques:

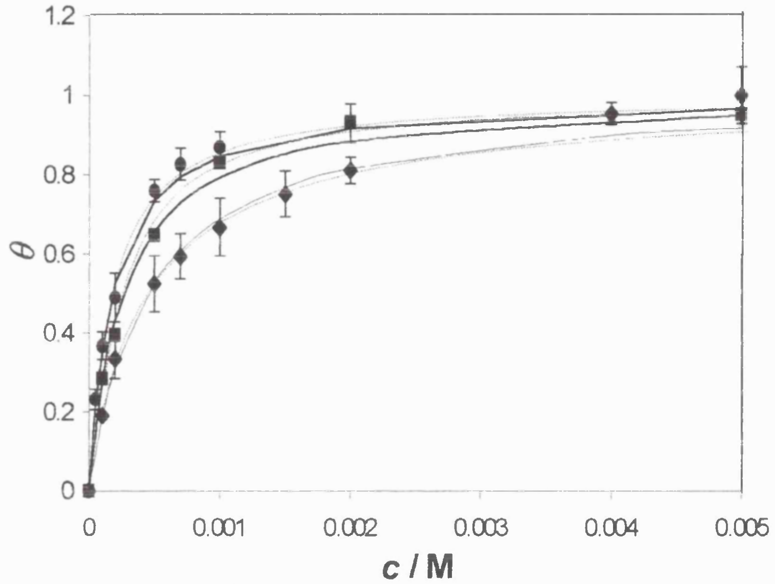

Figure 9. 1 Surface coverage θ vs. surfactant concentration c, obtained from the three different methods (see text). Circles are the experimental values of the capacitance experiments, squares the SECM measurements and diamonds the surface tension measurements, and error bars show the standard deviation. (Solid lines): Langmuir fits and (dashed lines): Frumkin fits

Although the interfacial potential difference was different for each of the methods, the capacitance data demonstrated that the surface coverage of surfactant was independent of the interfacial potential difference within the potential window studied, within experimental error. Figure 9.1 shows that the apparent surface coverage of surfactant obtained by assuming a simple 'patch' model for analysis of the capacitance data was very similar to that derived from the SECM data, which considered no reaction at the portions of the interface blocked by surfactant. The coincidence of these two estimates, strengthened confidence both in the idea that the surfactant covers the surface in patches and that the surfactant patches were inactive for the interfacial ET reaction. The different methods were thus consistent in this respect. The measurement of interfacial tension implied a somewhat smaller fractional surface coverage. The results can be reconciled if it is assumed that the packing density of surfactant in the patches formed increases with increasing surface coverage.

9.1.ii Effect of GOx adsorption

The adsorption of GOx at the liquid/liquid interface studied using impedance and surface tension was presented in chapter 7. The capacitance findings showed that variation of the nature and concentration of supporting electrolytes resulted in different behaviour, and that the adsorption process was very time and concentration dependent. The capacitance studies indicated the existence of two different adsorption states, with minima at 100 nM and 500 nM of bulk GOx concentration. This was further corroborated with surface tension measurements at the liquid/liquid interface, which showed an initial break at 100 nM and a saturation level at 400 nM. For higher concentrations both capacitance and surface tension methods indicated irreproducible behaviour. The capacitance study of the time dependence of GOx adsorption indicated that there were two distinct kinetic steps involved, with their respective time-scales being concentration dependent.

In order to gain a further insight into GOx adsorption at a hydrophilic/hydrophobic interface, the neutron reflection technique was employed. This was used for the study of GOx adsorption at the water/air interface. It was established that surface tension measurements at the water/air interface showed similar phenomena to those observed at the water/oil interface. The neutron reflection showed that for similar ionic strength, (I=0.2M) to that used in the study of the liquid/liquid interface, the adsorption of the enzyme was time and concentration dependent. At low concentrations (< 100 nM) the adsorption process was followed by conformational changes, where the enzyme flattened out, resulting in a layer of thickness smaller than any of the principal axis length determined by the crystal structure and an area/molecule larger than expected. At higher concentrations (100-400 nM) the enzyme retained its conformational rigidity as the molecules repelled each other. At even higher concentrations (>400 nM) a second layer that started to adsorb under the first one, inducing inter- and intra-layer protein/protein interactions. The presence of two layers and their interactions provided some explanation for the observed capacitance and interfacial tension observations at high concentrations, since based on the size of the enzyme, the adsorption could be considered to form a third layer with intermediate properties.

9.1.iii Interfacial ET-Effect of surfactant and GOx adsorption

Interfacial ET at a polarisable interface using a four-electrode set-up and at a non-polarisable interface using SECM was presented in chapter 5. The establishment of interfacial ET was not simple, a fact indicated also by the absence of literature entries on SECM measurements with DiMFc or four-electrode cyclic volltammograms with DcMFC. Nevertheless, careful choice of individual components and control of conditions, especially potential ranges, resulted in the successful study of interfacial ET with both techniques.

The effect of surfactants on ET was presented in Chapter 6. The effect of the presence of both SM and Triton X-100 on the redox electrochemistry at metal electrodes in individual phases was found to be negligible, which allowed the further study of their effect on interfacial ET at the liquid/liquid interface. From these studies it was concluded that the surfactant behaved as patches on an otherwise uncovered surface. An apparent geometry asymmetry was revealed from the cyclic voltammetry measurements: the surfactant patches appear to block the approach of the neutral molecules to the interface, but to inhibit the approach of the ionic species far less. This tentatively suggested that, depending on the potential difference across the interface, the surfactant-modified liquid-liquid interface is in general more readily disrupted by ions than by neutral molecules. It was suggested that the surfactant layer at high coverage behaved towards the uncharged DiMFc as a blocked interface penetrated with microholes of ca 200 nm radius, yet remained uniformly accessible to $DiMFc^+$.

GOx was adsorbed at the surfactant modified interface, and SECM was used to induce and measure interfacial ET via the adsorbed enzyme, as shown in chapter 8. In the absence of any other aqueous redox species, there seemed to be an unexpected regeneration of $DiMFc^+$ at the interface that was potential dependent and could not be deciphered further. Instead, this process was blocked in the presence of surfactant. Co-adsorption of GOx, spread at the interface for quick and maximum coverage at an estimated bulk concentration of ~550 nM, resulted in a positive feedback as the electrode approached the interface. The process once more had to be very carefully controlled. The effects of degassing and of interfacial potential difference indicated that the process takes place interfacially within an interfacial film of enzyme and surfactant. Nevertheless, it could not be ruled out that the process could also occur homogeneously, following ion transfer of $DiMFc^+$.

9.2 Further work

The effect of co-adsorption of enzyme and surfactant at the liquid/liquid interface could be explored with the techniques mentioned above. Moreover, different enzymes than the widely used GOx could be used, such as diaphorase, glucose dehydrogenase or true transmembrane proteins. Structural parameters for the enzyme layer adsorbed at the liquid/liquid interface could be obtained using surface sensitive techniques, such as the second harmonic generation method.

To date, SECM studies of the liquid/liquid interface had used a potential-determining ion to establish and interfacial potential difference. Ideally, SECM could be combined with a 4-electrode potentiostat to secure more flexible control over this potential difference. Certainly with a 3-electrode system, Amatore *et al.*[193] have already shown the mapping of concentration profiles produced at an approaching microelectrode within the diffusion layer of a disc electrode, obtained with potentiometric and amperometric measurements[194]. Some preliminary experiments for the four-electrode control of the potential difference at a liquid/liquid interface studied with SECM are shown in Appendix V.

Another field worth exploring further is the study of lateral electron transfer, occurring within the adsorbed layer of an interfacial mediator. Recently lateral proton diffusion rates have been measured by Unwin *et al.*[186] at Langmuir monolayers of stearic acid using SECM, operated in the induced desorption mode. In order to observe the result of the perturbation effect, the microelectrode was positioned within a distance equal to the electrode radius, or smaller. The deprotonation thus occurred in a spot of similar dimensions to the microelectrode and the response was controlled by three processes: solution diffusion, lateral diffusion and interfacial protonation/deprotonation reaction. The three processes could be resolved under different surface pressures, with the surface pressure controlled by Langmuir trough. Observation of any response required surface pressures > 0.1 mNm^{-1} and the probe electrode within 10 μm from the interface. The lateral diffusion could be deciphered once all the other processes were characterised and was found to be 15% of the bulk solution value. Majda *et al.*[187] carried out extensive measurements with octadecylferrocene layers, in a Langmuir trough with a microelectrode dipped just in the interface. It was found that the conditions (pressure, degassing, temperature and humidity) had to be thoroughly controlled for reproducible measurements. They studied the lateral diffusion of molecules and the effect of surface concentration on the lateral diffusion coefficient, eliminating the contribution of electron hopping between the redox sites. They also presented studies[188] of osmium(II) tris (4,7,-diphenanthroline) perchlorate, where the apparent diffusion coefficient increased with surface concentration, indicating that electron hopping was the main mechanism of the lateral charge propagation, that could only be measured for surface pressures >6 mNm^{-1}, to overcome a percolation threshold.

The lateral diffusion coefficient of ubiquinone and plastoquinones incorporated in bi-layers was thoroughly studied and presented with a quick review by Bourdillon *et al.*[190] They calculated the lateral diffusion coefficient of various quinones and found a value for UQ10 of 2.04 x 10^{8} cm^{2} s^{-1} in supported bilayers. Schiffrin and Gordillo[189] also presented the electrochemistry of UQ10 in a phospholipid model membrane at mercury drop electrode, where they demonstrated the various pathways involved, especially at different pH. These works indicate the feasibility and methodology for extending similar studies. A route forward is the possible co-adsorption of an interfacial mediator, instead of surfactant, with the enzyme. This would not only establish an interfacial ET via the adsorbed enzyme but also provide a system for studying lateral electron transfer within the adsorbed mediator layer. Some preliminary experiments with ubiquinone that did not prove successful were shown in chapter 8. More work needs to be done, varying the enzyme and mediator.

Reference List

1. Morrison L.E., Weber G., *Biophysical Journal*, 1987, **52**, 367.
2. Strycr, L. Biochemistry. 1995. Frccman W.H., New York.
3. Mitchell, P., *Science*, 1979, **206**, 1148.
4. Nernst, W., Reisenfeld, E. H., *Gottinger Nachrichten*, 1901, 54.
5. Cremer, Z., *Biologie*, 1906, **47**, 562.
6. Ostwald, W., *Biologie*, 1890, **6**, 71.
7. Davies, J. T., Rideal, E., *Can.J.Chem*, 1956, **33**, 947.
8. Gavagh, C., Mlodnicha, T., Guastalla, J., *Comptes Rendues de l' Academie Scientific, Series C*, 1968, **266**, 1196.
9. Guastalla, J., *Journal of Physical Chemistry*, 1957, **53**, 470.
10. Samec, Z., *Journal of Electroanalytical Chemistry*, 1977, **83**, 393.
11. Samec, Z., Marecek, V., Weber, J., *Journal of Electroanalytical Chemistry*, 1977, **96**, 245.
12. Koryta, J., Vanysek, P., Brezina, M., *Journal of Electroanalytical Chemistry*, 1977, **75**, 211.
13. Marcus, R. A., *Journal of the Chemical Society-Faraday Transactions*, 1996, **92**, 3905.
14. Marcus, R. A., *Advances in Chemistry Series*, 1991, 277.
15. Marcus, R. A., *Journal of Physical Chemistry*, 1991, **95**, 2010.
16. Marcus, R. A., *Journal of Physical Chemistry*, 1990, **94**, 4152.
17. *Journal of Electroanalytical Chemistry*, 2000, **483**.
18. Koryta, J., *Selective Electrode Reviews*, 1991, **13**, 133.
19. Koryta, J., *Electrochimica Acta*, 1988, **33**, 189.
20. Valent, O., Koryta, J., Panoch, M., *Journal of Electroanalytical Chemistry*, 1987, **226**, 21.
21. Koryta, J., *Electrochimica Acta*, 1984, **29**, 445.
22. Girault, H. H. J., Schiffrin, D. J., *Electroanalytical Chemistry*, 1989, **15**, 1.

23. Homolka, D., Le Hung, Q., Hofmnová, A., Khalil, M. W., Koryta, J., Marecek, V., Samec, Z., Sen, S. K., Vanýsek, P., Weber, J., B, Brezina, M., Janda, M., Stibor, I., *Analytical Chemistry*, 1980, **52**, 1606.

24. Kihara, S., Suzuki, M., Maeda, K., Ogura, K., Umetani, S., Matsui, M., Yoshida, Z., *Analytical Chemistry*, 1986, **58**, 2954.

25. Sawada, S., Osakai, T., Senda, M., *Kyoto*, 1989, **35**, 83.

26. Koczorowski, Z., Paleska, I., Geblewicz, G., *Journal of Electroanalytical Chemistry*, 1984, **164**, 201.

27. Alemu, H., Solomon, T., *Journal of Electroanalytical Chemistry*, 1989, **261**, 297.

28. Samec, Z., Homolka, D., Marecek, V., Kavan, L., *Journal of Electroanalytical Chemistry*, 1983, **145**, 213.

29. Paleska, I., Kotowski, J., Koczorowski, Z., Nakachr, E., Dupeyrat, M., *Journal of Electroanalytical Chemistry*, 1990, **278**, 129.

30. Solomon, T., Alemu, H., Hundhammer, B., *Journal of Electroanalytical Chemistry*, 1984, **169**, 303.

31. Hundhammer, B., Muller, C., Solomon, T., Alemu, H., Hassen, H., *Journal of Electroanalytical Chemistry*, 1991, **319**, 125.

32. Koczorowski, Z., Geblewicz, G., Panoch, M., *Journal of Electroanalytical Chemistry*, 1984, **172**, 327.

33. Guastalla, J., *Journal of Physical Chemistry*, 1957, **53**, 470.

34. Solomon, T., Alemu, H., Hundhammer, B., *Journal of Electroanalytical Chemistry*, 1984, **169**, 201.

35. Vanysek, P., Reid J.D., Craven, M. A., Buck, R. P., *Journal of ElectroChemical Society*, 1984, **131**, 1788.

36. Kontturi, A. K., Kontturi, K., Murtomaki, L., Schiffrin, D. J., *Journal of the Chemical Society-Faraday Transactions*, 1990, **86**, 819.

37. Kontturi, K., Murtomaki, L., Schiffrin, D. J., *Acta Chemica Scandinavica*, 1992, **46** , 25.

38. Osakai, T., Kakutani, T. S. M., *Bulletin of the Chemical Society of Japan*, 1984, **57**, 370.

39. Girault, H. H., *Electrochimica Acta*, 1987, **32**, 383.

40. Quinn, B., *PhD thesis*, Helsinki University of Technology, 2000.

41. Grahame, D. C., *Chemical Reviews*, 1947, **41**, 441.

42. Bard, A. J. and Faulkner, L. R. Electrochemical Methods, Fundamentals and Applications, 1980, Wiley, N.Y.

43. Liquid-Liquid interfaces,Theory and Models. Volkov, A. G. and Deamer, D. W. 1996. Boca Raton, Florida, CRC Press.

44. Verwey, E. J., Niessen, K. P., *Philos.Mag*, 1939, **28**, 435.

45. Gugeshashvili, M. I., Manevelyan M.A., Boguslavsky, L. I., *Soviet Electrochemistry*, 1974, **10**, 782.

46. Gavagh, C., Mlodnicha, T., Guastalla, J., *Comptes Rendues de l' Academie Scientific, Series C.,* 1968, **266**, 1196.

47. Kakiuchi, T., Senda, M., *Bulletin of the Chemical Society of Japan*, 1983, **56**, 1753.

48. Girault, H. H., Schiffrin, D. J., *Journal of Electroanalytical Chemistry*, 1983, **150**, 43.

49. Cheng, Y., Cunnane, V. J., Schiffrin, D. J., Mutomaki, L., Kontturi, K., *Journal of the Chemical Society-Faraday Transactions*, 1991, **87**, 107.

50. Samec, Z., Marecek, V., Homolka, D., *Journal of Electroanalytical Chemistry*, 1985, **187**, 31.

51. Torrie, G. M., Valleau, J. P., *Journal of Electroanalytical Chemistry*, 1986, **206**, 69.

52. Cui, Q., Zhu, G., Wang, E., *Journal of Electroanalytical Chemistry*, 1994, **372**, 15.

53. Pereira, C. M., Schmickler, W., Silva, F., Sousa, M. J., *Journal of Electroanalytical Chemistry*, 1997, **436**, 9.

54. Benjamin, I., *Science*, 1993, **261**, 1558.

55. Brevet, P. F., Girault, H. H., *Progress in Colloid Polymer Science*, 1997, **103**, 1.

56. Strutwolf, J., Barker, A. L., Gonsalves, M., Caruana, D. J., Unwin, P. R., Williams, D. E., Webster, J. P. R., *Journal of Electroanalytical Chemistry*, 2000, **483**, 163.

57. Hung, L. Q., *Journal of Electroanalytical Chemistry*, 1980, **149**, 1.

58. Hung, L. Q., *Journal of Electroanalytical Chemistry*, 1980, **115**, 159.

59. Parker, A. J., *Electrochimica Acta*, 1976, **21**, 94.

60. Reymond, F., Steyaert, G., Carrupt, P. A., Testa, B., Girault, H. H., *Helvetica Chimica Acta*, 1996, **79**, 101.

61. Osborne, M. D., Girault, H. H., *Electroanalysis*, 1995, **7**, 714.

62. Sabela, A., Marecek, V., Samec, Z., Fuoco, R., *Electrochimica Acta*, 1992, **37**, 231.

63. Girault, H. H. J., Schiffrin, D. J., *Journal of Electroanalytical Chemistry*, 1985, **195**, 213.

64. Kakiuchi, T., *Journal of Electroanalytical Chemistry*, 1992, **322**, 55.

65. Senda, M., Kakiuchi, T., Osakai, T., *Electrochimica Acta*, 1991, **36**, 253.

66. Girault, H. H. J., Schiffrin, D. J., *Journal of Electroanalytical Chemistry*, 1988, **244**, 15.

67. Girault, H. H. J., Schiffrin, D. J., *Journal of Electroanalytical Chemistry*, 1988, **244**, 15.

68. Cunnane, V. J., Schiffrin, D. J., Beltran, C., Geblewicz, G., Solomon, T., *Journal of Electroanalytical Chemistry*, 1988, **247**, 203.

69. Samec, Z., *Journal of Electroanalytical Chemistry*, 1979, **99**, 197.

70. Gavagh, C., Seta, C. P., D'Epenoux, B., *Journal of Electroanalytical Chemistry*, 1977, **83**, 225.

71. Hanzlik, J., Hovorka, J., Samec, Z., Toma, S., *Collection of Czechoslovak Chemical Communications*, 1988, **53**, 903.

72. Geblewicz, G., Schiffrin, D. J., *Journal of Electroanalytical Chemistry*, 1988, **244**, 27.

73. Kihara, S., Suzuki, M., Maeda, K., Ogura, K., Matsui, M., Yoshida, Z., *Journal of Electroanalytical Chemistry*, 1989, **271**, 107.

74. Chen, Q. Z., Iwamoto, K., Seno, M., *Electrochimica Acta*, 1991, **36**, 291.

75. Cheng, Y. F., Schiffrin, D. J., *Journal of Electroanalytical Chemistry*, 1991, **314**, 153.

76. Cunnane, V. J., Geblewicz, G., Schiffrin, D. J., *Electrochimica Acta*, 1995, **40**, 3005.

77. L'Her, M., Rosseau, R., L'Hostis, M., Roue, L., Laouenan, C. R *Comptes Rendues de l'Academie Scientific, Paris*, 1996, **322**, 55.

78. Suzuki, M., Umetani, S., Matsui, J., Kihara, S., *Journal of Electroanalytical Chemistry*, 1997, **420**, 119.

79. Ohde, H., Maeda, K., Yoshida, Y., Kihara, S., *Electrochimica Acta*, 1998, **44**, 23.

80. Ohde, H., Maeda, K., Yoshida, Y., Kihara, S., *Journal of Electroanalytical Chemistry*, 2000, **483**, 108.

81. Guanazzi, M., Silvestri, G., Serravale, G., *Journal of Chemical Society, Chemical Communications*, 1975, 201.

82. Cheng, Y. F., Schiffrin, D. J., *Journal of the Chemical Society-Faraday Transactions*, 1996, **92**, 3865.

83. Cunnane, V. J., Evans, U., *Chemical Communications*, 1998, 2163.

84. Lahtinen, R. M., Fermin, D. J., Jensen, H., Kontturi, K., Girault, H. H., *Electrochemistry Communications*, 2000, **2**, 230.

85. Johans, C., Lahtinen, R., Kontturi, K., Schiffrin, D. J., *Journal of Electroanalytical Chemistry*, 2000, **488**, 99.

86. Bard, A. J., Wipf, D. O., Unwin, P., *Abstracts of Papers of the American Chemical Society*, 1991, **201**, 51.

87. Solomon, T., Bard, A. J., *Analytical Chemistry*, 1995, **67**, 2787.

88. Wei, C., Bard, A. J., Mirkin, M. V., *Journal of Physical Chemistry*, 1995, **99**, 16033.

89. Tsionsky, M., Bard, A. J., Mirkin, M. V., *Journal of Physical Chemistry*, 1996, **100**, 17881.

90. Shi, C. N., Anson, F. C., *Analytical Chemistry*, 1998, **70**, 3114.

91. Shi, C. N., Anson, F. C., *Journal of Physical Chemistry B*, 1998, **102**, 9850.

92. Shi, C. N., Anson, F. C., *Journal of Physical Chemistry B*, 1999, **103**, 6283.

93. Barker, A. L., Unwin, P. R., *Journal of Physical Chemistry B*, 2000, **104**, 2330.

94. Shafer, H. O., Derback, T. L., Koval, C. A., *Journal of Physical Chemistry B*, 2000, **104**, 1025.

95. Cheng, Y. F., Schiffrin, D. J., *Journal of the Chemical Society-Faraday Transactions*, 1994, **90**, 2517.

96. Tsionsky, M., Bard, A. J., Mirkin, M. V., *Journal of the American Chemical Society*, 1997, **119**, 10785.

97. Delville, M. H., Tsionsky, M., Bard, A. J., *Langmuir*, 1998, **14**, 2774.

98. Amemiya, S., Ding, Z., Zhou, J. F., Bard, A. J., *Journal of Electroanalytical Chemistry*, 2000, **483**, 7.

99. Zhang, J., Unwin, P. R., *Journal of Electroanalytical Chemistry*, 2000, **494**, 47.

100. Zhang, J., Slevin, C. J., Murtomäki, L., Kontturi, K., Williams, D. E., Unwin, P. R., *Langmuir*, 2001, **17**, 821.

101. Dryfe, R. A. W., Ding, Z. F., Wellington, R. G., Brevet, P. F., Kuznetzov, A. M., Girault, H. H., *Journal of Physical Chemistry A*, 1997, **101**, 2519.

102. Ding, Z. F., Fermin, D. J., Brevet, P. F., Girault, H. H., *Journal of Electroanalytical Chemistry*, 1998, **458**, 139.

103. Lahtinen, R. M., Fermin, D. J., Kontturi, K., Girault, H. H., *Journal of Electroanalytical Chemistry*, 2000, **483**, 81.

104. Dryfe, R. A. W., Webster, R. D., Coles, B. A., Compton, R. G., *Chemical Communications*, 1997779.

105. Webster, R. D., Dryfe, R. A. W., Coles, B. A., Compton, R. G., *Analytical Chemistry*, 1998, **70**, 792.

106. Kott, K. L., Higgins, D. A., Mcmahon, R. J., Corn, R. M., *Journal of the American Chemical Society*, 1993, **115**, 5342.

107. Fermin, D. J., Ding, Z. F., Duong, H. D., Brevet, P. F., Girault, H. H., *Chemical Communications*, 1998, 1125.

108. Ohde, H., Maeda, K., Shirai, O., Yoshida, Y., Kihara, S., *Journal of Electroanalytical Chemistry*, 1997, **438**, 139.

109. Maeda, K., Kihara, S., Suzuki, M., Matsui, M., *Journal of Electroanalytical Chemistry*, 1991, **303**, 171.

110. Kakiuchi, T., *Analytical Chemistry*, 1996, **68**, 3658.

111. Kakiuchi, T., *Electrochimica Acta*, 1995, **40**, 2999.

112. *Scanning Electrochemical Microscopy*, Bard A.J., Mirkin M. V., Marcel Dekker, Inc, New York, 2001.

113. Bard, A. J., Fan, F. R. F., Mirkin, M. V., *Electroanalytical Chemistry*, Marcel Dekker, New York, 1993, vol. 18, 243.

114. Georganopoulou, D. G., Caruana, D. J., Strutwolf, J., Williams, D. E., *Faraday Discussions*, *Bioelectrochemistry*, 2000, **116**, 109.

115. Slevin, C. J., Unwin, P. R., *Langmuir*, 1997, **13**, 4799.

116. Pereira, C. M., Scmickler, W., Silva, A. F., Sousa, M. J., *Chemical Physical Letters*, 1997, **268**, 13.

117. Pereira, C. M., Martins A., Rocha, M., Silva, C. J., Silva, F., *Journal of Chemical Society, Faraday transactions*, 1994, **90**, 143.

118. Cheng, Y., Cunnane, V. J., Schiffrin, D. J., Mutomaki, L., Kontturi, K., *Journal of the Chemical Society-Faraday Transactions*, 1991, **87**, 107.

119. Samec, Z., Langmaier, J., Trojanek, A., *Journal of Electroanalytical Chemistry*, 1999, **463**, 232.

120. Cheng, Y. F., Schiffrin, D. J., *Journal of the Chemical Society-Faraday Transactions*, 1993, **89**, 199.

121. Chen, Q. Z., Iwamoto, K., Seno, M., *Electrochimica Acta*, 1991, **36**, 291.

122. Samec, Z., Lhotsky, A., Marecek, V., Marecek, V., *Journal of Electroanalytical Chemistry*, 2000, **483**, 47.

123. Debye, P., *Physica A*, 1912, **13**, 97.

124. Du Noüy, *Journal of General Physiology*, 1916, **1**, 521.

125. Zhang, J., Rosilio, V., Goldmann, M., Boissonnade M.M., Bazskin, A., *Langmuir*, 2000, **16**, 1226.

126. Rosilio, V., Boissonnade M.M., Zhang, J., Jiang, L., Bazskin, A., *Langmuir*, 1997, **13**, 4669.

127. Tripp, B. C., Magda, J. J., Andrade, J. D., *Journal of Colloid and Interface Science*, 1995, **173**, 16.

128. Peltonen, L. J., Yliruusi, J., *Journal of Colloid and Interface Science*, 2000, **277**, 1.

129. *Physical chemistry of surfaces*, John Wiley & Sons, New York, 5th ed., 1990.

130. Lu, J. R., Su, T. J., Thomas, R. K., *Journal of Colloid and Interface Science*, 1999, **213**, 426.

131. Lu, J. R., Su, T. J., *Langmuir*, 1999, **15**, 6975.

132. Lu, J. R., Su, T. J., Thomas, R. K., Penfold J., Webster, J., *Journal of Chemical Society, Faraday transactions*, 1998, **94**, 3279.

133. Strutwolf, J., Barker, A. L., Gonsalves, M., Caruana, D. J., Unwin, P. R., Williams, D. E., Webster, J. P. R., *Journal of Electroanalytical Chemistry*, 2000, **483**, 163.

134. Lu, J. R., Su, T. J., Thomas, R. K., Penfold J., Webster, J., *Journal of Chemical Society, Faraday transactions*, 1998, **94**, 3279.

135. Lu, J. R., Simister, E. A., Thomas, R. K., Penfold J., *Journal of Physics-Condensed Matter*, 1994, **6**, A403.

136. *Liquid interfaces in chemistry and biology*, Wiley-Interscience, New York, 1998.

137. *Liquid Interfaces in Chemical, Biological, and Pharmaceutical Applications*, Marcel Dekker Inc., New York, 1st ed., 2001.

138. Pereira, C. M., Schmickler, W., Sousa, M. J., *Journal of Electroanalytical Chemistry*, 1997, **436**, 9.

139. Samec, Z., Langmaier, J., Trojanek, A., *Journal of the Chemical Society-Faraday Transactions*, 1996, **92**, 3843.

140. Kontturi, A. K., Kontturi, K., Murtomaki, L., Schiffrin, D. J., *Journal of the Chemical Society-Faraday Transactions*, 1990, **86**, 931.

141. Slevin, C. J., Gray, N. J., Macpherson, J. V., Webb, M. A., Unwin, P. R., *Electrochemistry Communications*, 1999, **1**, 282.

142. Barker, A. L., Gonsalves, M., Macpherson, J. V., Slevin, C. J., Unwin, P. R., *Analytica Chimica Acta*, 1999, **385**, 223.

143. Kakiuchi, T., Yamane, M., Osakai, T., Senda, M., *Bulletin of Chemical Society of Japan*, 1987, **60**, 4223.

144. Wandlowski, T., Marecek, V., Samec, Z., *Journal of Electroanalytical Chemistry*, 1988, **242**, 277.

145. Wandlowski, T., Racinsky, S., Marecek, V., Samec, Z., *Journal of Electroanalytical Chemistry*, 1987, **227**, 281.

146. Kakiuchi, T., Teranishi, Y., Niki, K., *Electrochimica Acta*, 1995, **40**, 2869.

147. Pereira, C. M., Martins A., Rocha, M., Silva, C. J., Silva, F., *Journal of Chemical Society, Faraday transactions*, 1994, **90**, 143.

148. Quinn, B., Kontturi, K., *Journal of Electroanalytical Chemistry*, 2000, **483**, 124.

149. Geblewicz, G., Schiffrin, D. J., *Journal of Electroanalytical Chemistry*, 1988, **244**, 27.

150. Cunnane, V. J., Geblewicz, G., Schiffrin, D. J., *Electrochimica Acta*, 1995, **40**, 3005.

151. Quinn, B., Kontturi, K., *Journal of Electroanalytical Chemistry*, 2000, **483**, 124.

152. Osakai, T., Jensen, H., Nagatani, H., Fermin, D. J., Girault, H. H., *Journal of Electroanalytical Chemistry*, 2001, **510**, 43.

153. Zhang, J., Unwin, P. R., *Journal of Electroanalytical Chemistry*, 2000, **494**, 47.

154. Zhang, J., Barker, A. L., Unwin, P. R., *Journal of Electroanalytical Chemistry*, 2000, **483**, 95.

155. Strutwolf, J., Manzanares, J. A., Williams, D. E., *Electrochemical Communications*, 1999, **1**, 139.

156. Cheng, Y. F., Schiffrin, D. J., *Journal of the Chemical Society-Faraday Transactions*, 1994, **90**, 2517.

157. Chesniuk, S. G., Dassie, S. A., Yudi, L. M., Baruzzi, A. M., *Electrochimica Acta*, 1998, **43**, 2175.

158. Zhang, J., Slevin, C. J., Murtomäki, L., Kontturi, K., Williams, D. E., Unwin, P. R., *Langmuir*, 2001, **17**, 821.

159. Amatore, C., Saveant, J. M., Tessier, D., *Journal of Electroanalytical Chemistry*, 1983, **147**, 39.

160. Paul, H. J., Corn, R. M., *Journal of Physical Chemistry B*, 1997, **101**, 4494.

161. Hickel, A., Radke, C., Blanch , H. W., *Journal of Molecular Catalysis B: Enzymatic*, 1998, **5**, 349.

162. Ismond, M. A. H., Georgiou, C., Arntfield, S. D., Murray, E. D., *Journal of Food Science*, 1990, 55.

163. Gajraj, A., Ofoli, R. Y., *Langmuir*, 2000, **16**, 4279.

164. Vanysek, P., Sun Z., *Bioelectrochemistry and Bioenergetics*, 1990, **23**, 177.

165. Vanysek, P., Reid J.D., Craven, M. A., Buck, R. P., *Journal of ElectroChemical Society*, 1984, **131**, 1788.

166. Georganopoulou D.G., Jones D., Carley R., Boutelle, M. G., *Faraday Discussions, Bioelectrochemistry,* 2001, **116**, 291.

167. Hecht, H. J., Kalizs, H. M., Hendle, J., Schmid, R. D., Schomburg, D., *Journal of Molecular Biology*, 1993, **229**, 153.

168. Sun, S., Ho-Si., P. H., Harrison D.J., *Langmuir*, 1991, **7**, 727.

169. Fiol, C., Valleton, J. M., Delphire, N., Barbey.D, Barraud, A., Ruaudel-Teixier, A., *Thin Solid Films*, 1992, **215**, 88.

170. Baszkin A., Boissonnade M.M., Rosilio, V., Kamyshny, A., Magdassi, S., *Journal of Colloid and Interface Science*, 1999, **209**, 302.

171. Kriechbaum, M., Heilmann, H. J., Wientjes, F. J., Hahn, M., Jany, K.-D., Gassen, H. G., Sharif, F., Alaeddinoglu, G. F., *Febs Letters*, 1989, **255**, 63.

172. Hecht, H. J., Schomburg, D., Kalizs, H. M., Schmid, R. D., *Biosensors Bioelectronics*, 1993, **8**, 197.

173. Duinhoven, S., Poort, R., Vandervoet, G., Agterof, W. G. M., Norde, W., Lyklema, J., *Journal of Colloid and Interface Science*, 1995, **170**, 340.

174. Roth, C., Lenhoff, A. M., *Langmuir*, 1995, **11**, 3500.

175. Rosilio, V., Boissonnade M.M., Zhang, J., Jiang, L., Bazskin, A., *Langmuir*, 1997, **13**, 4669.

176. Tripp, B. C., Magda, J. J., Andrade, J. D., *Journal of Colloid and Interface Science*, 1995, **173**, 16.

177. Lu, J. R., Su, T. J., Thirtle, P. N., Thomas, R. K., Rennie, A. R., Cubitt, R., *Journal of Colloid and Interface Science*, 1998, **206**, 212.

178. Kakiuchi, T., Kondo, T., Kotani, M., Senda, M., *Langmuir*, 1992, **8**, 169.

179. Rinuy, J., Brevet, P. F., Girault, H. H., *Biophysical Journal*, 1999, **77**, 3350.

180. Su, T. J., Lu, J. R., Cui, Z. F., Thomas, R. K., Penfold J., *Journal of Physical Chemistry B*, 1998, **102**, 8100.

181. Zhang, J., Rosilio, V., Goldmann, M., Boissonnade M.M., Bazskin, A., *Langmuir*, 2000, **16**, 1226.

182. Wei, C., Bard, A. J., Mirkin, M. V., *Journal of Physical Chemistry*, 1995, **99**, 16033.

183. Deshaies, C., Chopineau, J., Moiroux, J., Bourdillon, C., *Journal of Physical Chemistry*, 1996, **100**, 5063.

184. Pierce, D. T., Unwin, P. R., Bard, A. J., *Analytical Chemistry*, 1992, **64**, 1795.

185. Kakiuchi, T., Kondo, T., Kotani, M., Senda, M., *Langmuir*, 1992, **8**, 169.

186. Slevin, C. J., Unwin, P. R., *Journal of the American Chemical Society*, 2000, **122**, 2597.

187. Charysh, D. H., Landau, E. M., Majda, M., *Journal of the American Chemical Society*, 1991, **113**, 3340.

188. Charysh, D. H., Majda, M., *Thin Solid Films*, 1992, **210/211**, 348.

189. Gordillo, G. J., Schiffrin, D. J., *Journal of Chemical Society, Faraday Discussions, Bioelectrochemistry*, 2000, **116**, 89.

190. Deshaies,C., Chopineau, J, Moiroux,J., Bourdillon,C., *Journal of Physical Chemistry B*, 1996, **100**, 5063.

191. Horrocks, B. R., Mirkin, M. V., Pierce, D. T., Bard, A. J., Nagy, G., Toth, K., *Analytical Chemistry*, 1993, **65**, 1213.

192. Selzer, Y., Turyan, I., Mandler, D., *Journal of Physical Chemistry B*, 1999, **103**, 1509.

193. Amatore, C., Szunerits, S., Thouin, L., *Electrochemical Communications*, 2000, **2**, 248.

194. Amatore, C., Szunerits, S., Thouin, L., Warkocz, J.-S., *Electrochemical Communications*, 2000, **2**, 353

APPENDIX 1: Ionic activities

For the purposes of this work, the estimation of Galvani interfacial potential difference is based on the extra assumption that the activity coefficients are taken as $\gamma_i^o = \gamma_i^w = 1$, and the formal potential is equal to the standard potential: $\Delta\phi^\theta = \Delta\phi^0 + \frac{RT}{zF}\ln\frac{\gamma_i^{(o)}}{\gamma_i^{(w)}} \approx \Delta\phi^0$. In this case, ionic activities are taken equal to concentrations $a_i = \gamma_i c_i . = c_i$.

Alternatively, ionic activities, a_i, can be estimated based on values for the aqueous activity coefficients in the *Handbook of Chemistry*, CRC Press, 57th edition, or from a calculation using the Debye-Huckel equation[1]:

$$\log\gamma_i = -\frac{A|z_i|\sqrt{I}}{1 + Bd^*\sqrt{I}} \qquad \text{(A1.1)}$$

where I is the ionic strength of the solution

d^* is the distance of closest approach

$$\text{constant } A = -\frac{\varepsilon^3 N_A^{\frac{1}{2}}}{4\pi\ln(10)\sqrt{2}(\varepsilon_0 k\varepsilon T)^{\frac{3}{2}}} = 1.82481\cdot 10^6(\varepsilon T)^{\frac{-3}{2}}(dm^{\frac{3}{2}}mol^{\frac{-1}{2}})$$

$$\text{constant } B = \frac{2\varepsilon^2 N_A}{(\varepsilon_0 k\varepsilon T)} = 502.9(\varepsilon T)^{\frac{-1}{2}}(dm^{\frac{3}{2}}mol^{\frac{-1}{2}}nm^{-1})$$

with ε the relative permittivity of the solvent, (DCE: 10.38 for H_2O:75.84)

e= the elementary charge (1.602 10^{-19} C),

N_A= the Avogadro number (6.0222 10^{-23} mol^{-1})

ε_0= the permittivity of the vacuum (8.854 10^{-12} Fm^{-1})

The ionic strength needed for equation A1.1 is given for complete dissociation:

$$I = \frac{1}{2}\sum_i z_i^2 c_i \qquad \text{(A1.2)}$$

and for part dissociation of electrolytes

$$I = \frac{1}{2}\sum_i \alpha z_i^2 c_i \qquad \text{(A1.3)}$$

with α the degree of dissociation obtained from

$$K_A = \frac{(1-a)}{(a^2 \gamma_{\pm}^2 c)} \qquad \text{(A1.4)}$$

where K_A is the association constant

and $\gamma_{\pm}$ the mean activity coefficient of the associating electrolyte.

Complete dissociation of electrolytes in the aqueous phase is assumed. Reference A2 gives the association constant and distance of closest approach calculated for various organic electrolytes, such as TPAsTPB[2].

APPENDIX 2: MS spectra

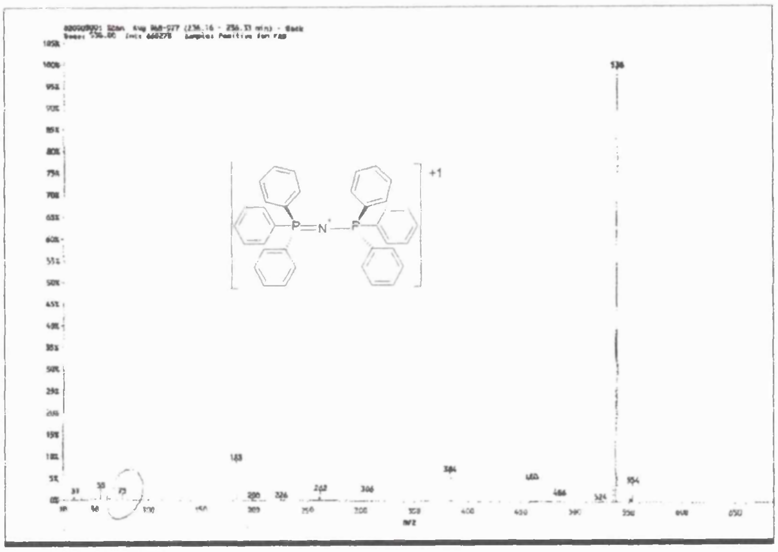

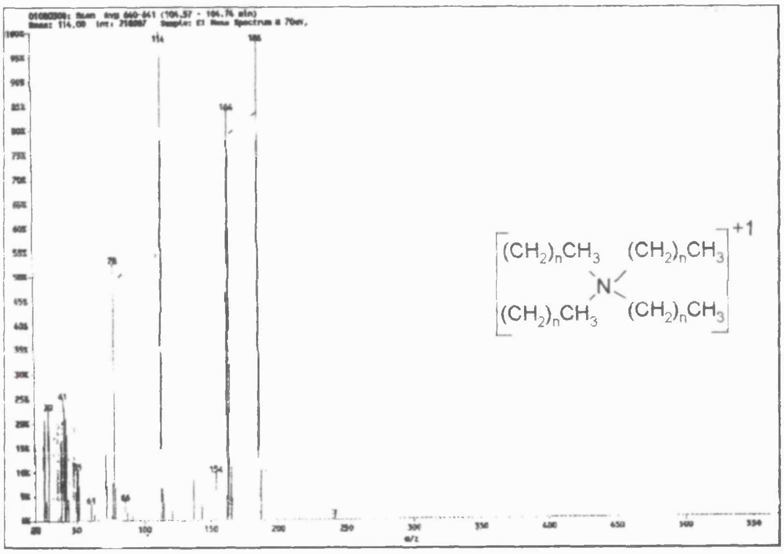

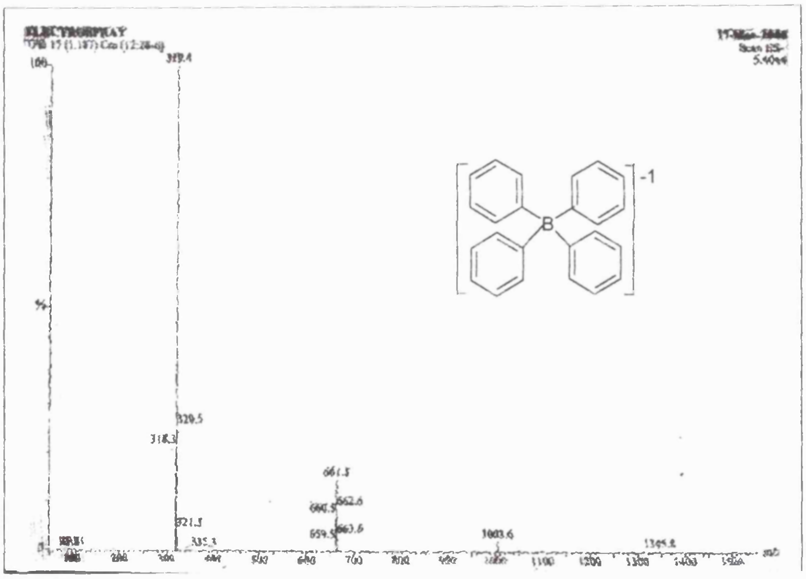

APPENDIX 3: UV-Vis studies of ferrocene derivatives

UV-Vis spectroscopy was used to investigate the solubility of the organic redox species used throughout the present study in the aqueous phase and the spontaneity of ET reactions at the open circuit potential (OCP) established. This ensured that the ET reactions studied was not impaired by any homogeneous or side-reactions. It is more likely for the charged organic species, produced following ET, to transfer in the aqueous phase, but this could not be studied with the equipment available. A possible approach would be with in-situ spectrosopy[3;4].

The possibility of "spontaneous" interfacial reactions was investigated with UV-Vis spectroscopy of each phase following vigorously mixing of the two phases. Figure A3.1 shows the UV-Vis spectra of the organic phase containing various ferrocene derivatives in the absence of partitioning ion (open circuit potential). For all three derivatives, two characteristic absorption bands can be observed, with a very intense peak at 230 nm (not shown) and weaker ones at 325 nm and 430 nm. The band at 230 is characteristic of the aromatic properties of the cis-diene analog. It can be seen that interaction with the aqueous phase results has some effect on the concentration of DcMFc in the organic phase.

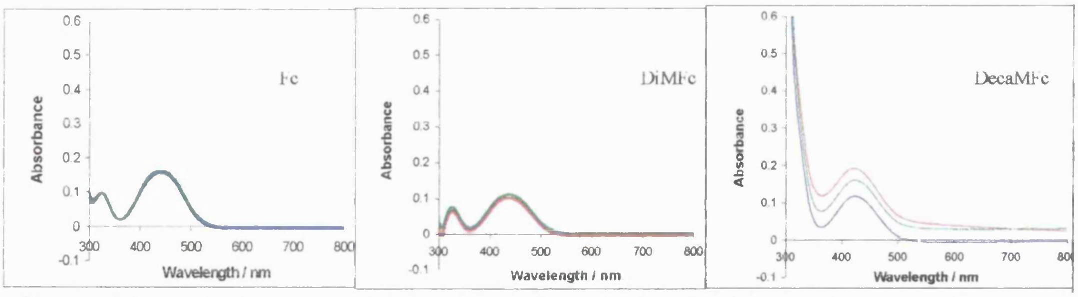

Figure A3.1 UV-Vis spectra of the various FC- derivatives in the organic phase (blue line) and the effect of vigorously shaking the organic phase (0.001BTPPATPB) with the aqueous phase (red line: 0.2 M PO4, green line: 0.2 M PO4 + 0.05 M Glu).

When partitioning ions were present that established various interfacial potential differences, $\Delta\phi$, (TBuATPB-TBuACl and TEAClO$_4$-NaClO$_4$) there was no effect resulting from the mixing of the two phases observed in the organic phase. Only in the case of perchlorate as PDI did a very weak absorption peak at 890 nm appear (results not shown).

Figure A3.2 shows the UV-Vis spectra of the aqueous phase after equilibrating with the organic phase in the absence of partitioning ions. A weak absorption peak appeared at 264.5nm, even in the absence of ferrocene derivatives. It was observed that in the case of DiMFc there was no difference after mixing the two phases. For DcMFc, a small absorption band appeared at 326 nm, whereas for Fc a big absorption band at 225 nm was found (Figure A3.2). This indicated a breakdown of the cyclopentadienyl complex and dissolution in the aqueous phase:

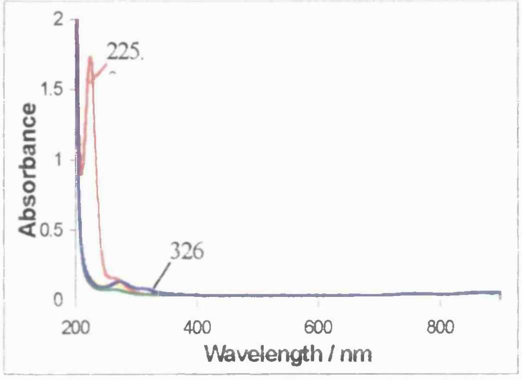

Figure A3.2 UV-Vis spectra of the the aqueous phase (0.2 M PO4 + 0.05 M Glu) after being vigorously shaken with the organic phase (0.001BTPPATPB) containing various FC- derivatives (Blue line: -, Green line:DiMFC, Red line:Fc, Black line: DcMFc)

In the presence of the partitioning ions ($TBuA^+$ and ClO_4^-) there was no effect in the aqueous phase following the vigorous mixing with the organic phase containing various ferrocene derivatives, and no apparent bands appear. It is suggested that for the potential differences $\Delta\phi$ established by $TBuA^+$ or ClO_4^- there were no side-reactions taking place. When hexacyanoferrate (characteristic absorption band at 420 nm) was present in the aqueous phase, following mixture with DcMFc in DCE with ClO_4^- as a PDI there was a significant effect on both spectra. In the spectrum of the aqueous solution, there was a three-fold increase of the absorption intensity of the band at 420 nm and an appearance of a band at 780 nm. Conversely, in the organic solution, the intense peak at 230 nm disappeared and a peak at 780 nm appeared. It is suggested that at the potential difference established, spontaneous ET took place between DcMFc and $Fe(CN)_6^{3}$. In the case of DiMFc, spontaneous ET was not observed in the presence or absence of the PDI. However, depending on the electrolytes, the PDI (i.e. $\Delta\phi$) and the ratio of $Fe(CN)_6^{3-/4-}$ that controls the OCP, some blue precipitates were observed, probably due to interfacial complexation.

APPENDIX 4: UV-Vis studies of GOx solubility

UV-Vis spectroscopy was used to establish the solubility of the enzyme GOx in 1,2-dichloroethane. Figure A4.1 shows the spectra obtained for 10 μm of GOx in the phosphate aqueous buffer solution (pH=7), as well as in the organic solution. An equimolar amount of GOx was added to the organic solution and sonicated, but seemed to have limited solubility in DCE. The solution was then paper filtered; the UV-Vis response gave an adsorption peak at 300 nm (See Figure A4.1). The organic solution then was further filtered using Millipore Millex-SR filters (Hydrophobic PTFE 0.5 μm) and the filtrate was analysed again. This time there were no adsorption peaks throughout the wavelength range studied. Both responses were corrected for the baseline obtained for the phosphate buffer and the organic solvent.

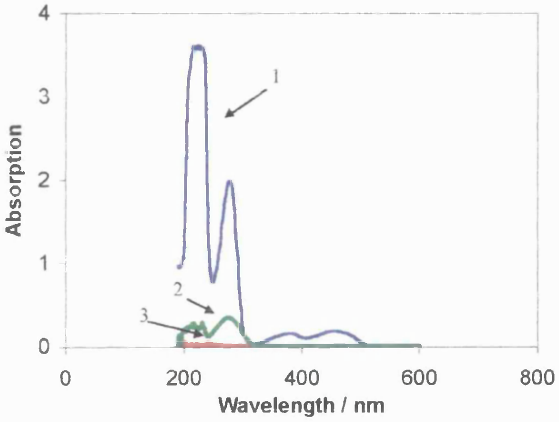

Figure A4.1 UV-Vis spectra of 10 μm GOx in the aqueous buffer (blue line 1), and the organic solvent, after paper filtering (green line 2)or PTFE filtering (red line 3)

The enzyme spectrum measured in the aqueous phase showed the characteristic adsorption bands associated with the $\pi \rightarrow \pi^*$ transition of the oxidised flavin adenine dinucleotide (FAD) at 385 nm and 465 nm. FAD apart from being the chromophore, is also responsible for the redox activity of the enzyme. It is evident that an enzyme as complicated and heavy as GOx is transparent in the ultraviolet, resulting in a simple UV-Vis spectrum due to the $\pi \rightarrow \pi^*$ transitions along the three cycles of the isoalloxazine ring. The paper filtered organic filtrate resulted in a UV-Vis adsorption peak at 300 nm, probably due to some suspended enzyme particles, whereas finally the organic filtrate from filtration through PTFE filters showed no adsorption peaks throughout the studied range. With this simple experiment therefore it was clarified that GOx does not dissolve in the organic phase.

APPENDIX 5 Four-electrode control of $\Delta\phi$ in SECM studies

The set-up used for some preliminary experiments of four-electrode control of the potential difference of an interface studied with SECM was a combination of the two available commercial systems. The four-electrode cell was used (not shown in Figure) controlled by the four electrode Autolab potentiostat and its interface of 0.28 cm^2 was studied with an SECM microelectrode using the µ-Autolab potentiostat, illustrated in Figure A5.1:

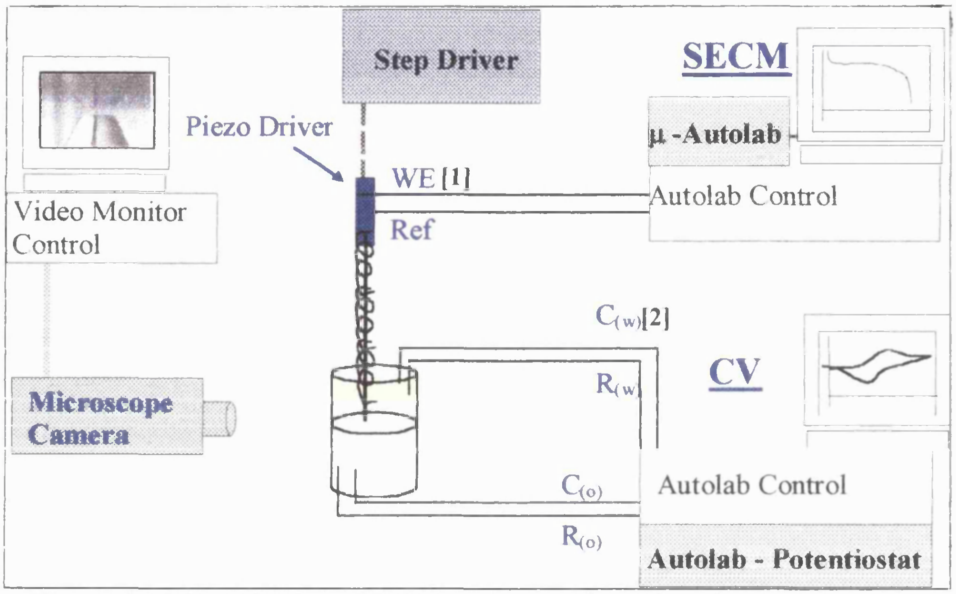

Figure A5.1 Combination of SECM and Four-Electrode voltammetry set-ups, with a simplified schematic of the four-electrode cell. The two electrodes [1] and [2] are the virtual earth connections of the two systems respectively.

For some preliminary experiments carried out for this system the following cell was used as in chapter 5:

Ag/AgCl / 1 mM BTPPACl, 10 mM LiCl / 1 mM BTPPA-TPB, 0.1 mM DiMFc//
1.5 M Li_2SO_4, 0.1 M $K_3[Fe^{III}(CN)_6]$, 0.01 M $K_4[Fe^{II}(CN)_6]$ / ***Pt***

Interfacial ET occurs across the interface, polarised by the potentiostat:

$$\mathrm{DiMFc} + Fe(CN)_6^{3-} \rightarrow \mathrm{DiMFc}^+ + Fe(CN)_6^{4-}$$

The microelectrode in the aqueous phase positioned within 200 µm of the interface, operating in amperometric mode monitors local changes in solution composition, due to the interfacial ET reaction:

$$Fe(CN)_6^{4-} \rightarrow Fe(CN)_6^{3-} + e^-$$

Alternatively the local composition changes can be measured potentiometrically at open circuit.

The existence of both sets of electrodes of the two different potentiostats in the same system, raises questions about the coupling between the two systems. However, if the two different working electrodes in the aqueous phase labelled [1] and [2] in Figure A5.1, are at the same potential and chemical environment, then no current will flow between them. This condition can be achieved by ensuring that both electrodes are the virtual earth terminal of the respective potentiostats, and that the two potentiostats have a common earth connection

Figure A5.2 shows the potentiometric results of a stationary microelectrode, situated near the externally controlled interface, while four-electrode cyclic voltammetry takes place.

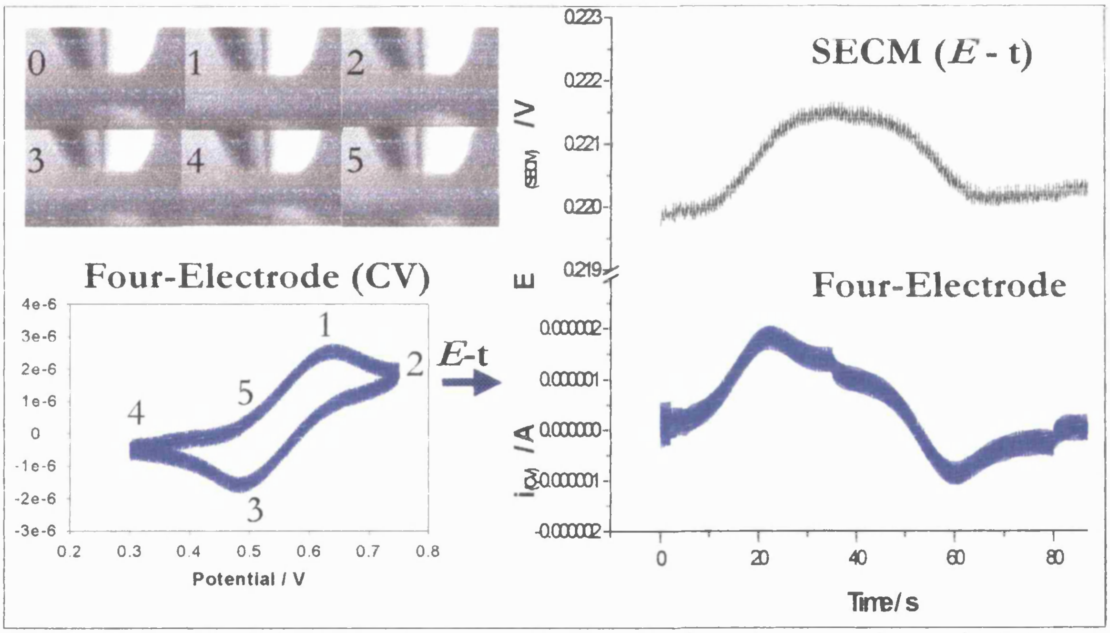

Figure A5.2 Preliminary experiment from the combination of two techniques with SECM microelectrode operating in potentiometric mode. Anticlockwise: Video images of the SECM electrode positioned at 200μm from the polarised interface that oscillates depending on the interfacial potential, four electrode CV, $A = 28$ mm^2, υ=25mV/s, transformed to E-t curve, while SECM monitors E-t.

Figure A5.2 also established the effect of the externally applied potential difference on the surface tension of the interface that was not completely flat. The interface relaxed prior to any externally applied voltage, (image 0) and then contracted once the interfacial potential was applied (images 1,3,5). At the edge of the potential window, when IT started taking place, the interface expanded again (images 2,4). In this case the microelectrode was positioned 200 μm away from the interface (at the edge of diffusion layer). The changes in the measured potential indicated the change in the concentration profiles and the movement of the interface. It can be seen that as the ferrocyanide concentration increases and ferricyanide decreases the potential increases as well.

Alternatively the four-electrode set-up could be operated in an amperometric mode, that would ensure that the interface was stable at one specific potential. The SECM tip, operated in potentiometric mode, could then approach the interface, to measure the local changes in concentration profiles. Figure A5.3 shows the four-electrode cyclic voltammetry as well as the transient chronoamperometry that establishes different potential difference across the interface: The four electrode responses shown were monitored when the SECM microelectrode was not connected in the cell.

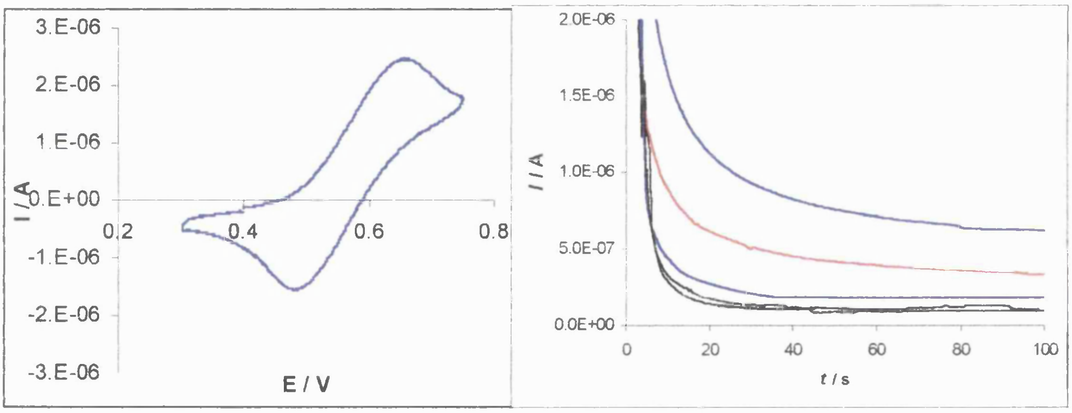

Figure A5.3 Four electrode responses, left cyclic voltammogram at A= 28 mm^2, υ=25mV/s, right chronoamperograms at various potentials, from top to bottom: E=400,450, 500,550,650 mV

Provided the electronics of the set-up are resolved the SECM tip could then approach the interface, measuring the different concentration changes due to the interfacial ET at different potentials that are now established externally. The need of PDI in this case of SECM was not necessary. The range of application of the technique could therefore be greatly extended as SECM is already a well-known method of monitoring local concentration changes while approaching an interface [5-8].

With both systems operated in potentiostatic mode, the question of coupling of the two systems is an important one. Figure A5.4 shows the effect of operating SECM in an amperometric mode, while a four electrode cyclic voltammogram takes place as in Figure A5.3,

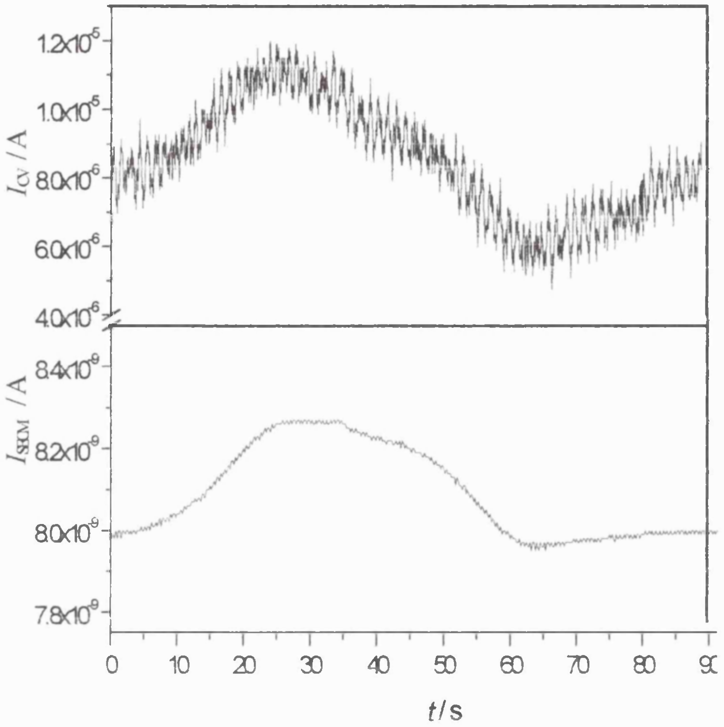

Figure A5.4 Preliminary experiments from the combination of two techniques with SECM microelectrode operating in amperometric mode. Top curve: four electrode CV, transformed to an *I-t* curve, while at the bottom curve the stationary SECM near the interface monitors *I-t*.

Figure A5.4 indicates the issues raised regarding the electronics of the combined system, as the four electrode CV of Figure A5.3, exhibits a current offset of 8 µA. The use of battery operated potentiostat for the SECM measurement would ensure isolation of this system from the four-electrode potentiostat. However, even in the present case, when both potentiostats had a common ground and the aqueous working electrode of each system was at virtual earth potential, some success in SECM measurements with an electrically controlled interface was obtained

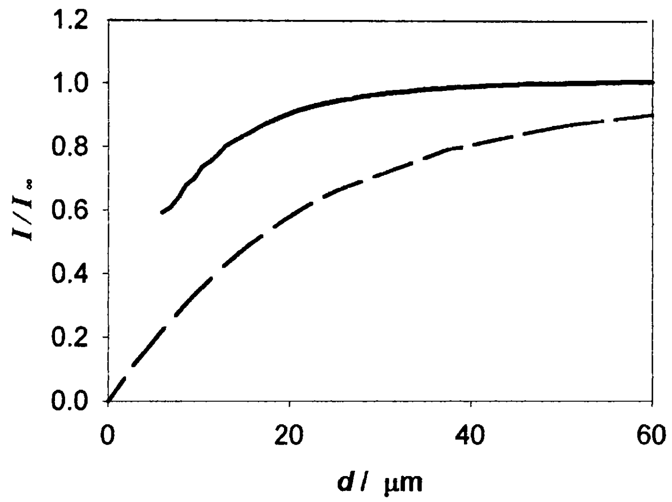

Figure A5.5 SECM approach curve of a microelectrode at an interface were an external potential of E=650 V is applied (solid line) and a theoretical fit of an insulator response (dashed line)

A possible innovation (not explored) would be to use a current follower in the earth connection between the two potentiostats, to check on leakage currents between the two systems.

Reference List for Appendices

A.1. Cheng, Y., Cunnane, V. J., Schiffrin, D. J., Mutomaki, L., Kontturi, K., *Journal of the Chemical Society-Faraday Transactions*, 1991, **87**, 107.

A.2. Samec, Z., Langmaier, J., Trojanek, A., *Journal of Electroanalytical Chemistry*, 1996, **409**, 1.

A.3. Ding, Z. F., Brevet, P. F., Girault, H. H., *Chemical Communications*, 1997, 2059.

A.4. Dryfe, R. A. W., Webster, R. D., Coles, B. A., Compton, R. G., *Chemical Communications*, 1997, 779.

A.5. Slevin, C. J., Unwin, P. R., *Langmuir*, 1999.

A.6. Horrocks, B. R., Mirkin, M. V., Picrcc, D. T., Bard, A. J., Nagy, G., Toth, K., *Analytical Chemistry*, 1993, **65**, 1213.

A.7. Zhang, J., Barker, A. L., Unwin, P. R., *Journal of Electroanalytical Chemistry*, 2000, **483**, 95.

A.8. Selzer, Y., Turyan, I., Mandler, D., *Journal of Physical Chemistry B*, 1999, **103**, 1509.